ABNORMAL BRAIN CONNECTIVITY IN THE PRIMARY VISUAL PATHWAY IN HUMAN ALBINISM

ANAHIT GRIGORIAN

A THESIS SUBMITTED TO THE FACULTY OF GRADUATE STUDIES
IN PARTIAL FULFILMENT OF THE REQUIREMENTS
FOR THE DEGREE OF
MASTER OF SCIENCE

GRADUATE PROGRAM IN BIOLOGY
YORK UNIVERSITY
TORONTO, ONTARIO

SEPTEMBER 2015

Abstract

In albinism, the ipsilateral projection of retinal axons is significantly reduced, and most fibres project contralaterally. The retina and optic chiasm have been proposed as sites for misrouting. The number of lateral geniculate nucleus (LGN) relay neurons has been linked to LGN volume, suggesting a correlation between LGN size and the number of tracts traveling through the optic radiation (OR) to the primary visual cortex (V1). Using diffusion data and both deterministic and probabilistic tractography, we studied differences in OR between albinism and controls. Statistical analyses measured white matter integrity in areas corresponding to the OR, as well as LGN to V1 connectivity. Results revealed reduced white matter integrity and connectivity in the OR region in albinism compared to controls, suggesting altered structural development. Previous reports of smaller LGN and the altered thalamo-cortical connectivity reported here demonstrate the effect of misrouting on structural organization of the visual pathway in albinism.

Acknowledgements

I would like to express my gratitude to my supervisor, Dr. Keith Schneider, for accepting me into his neuroimaging lab and revealing the world of neuroscience to me. I am very grateful for his constant support of my work, and the freedom I was given to focus on my research interests. I am greatly appreciative of all the opportunities he made available for me, from running experiments and writing this thesis, to attending conferences, presenting posters and writing manuscripts for publication.

I wish to extend warmest thanks to my committee member Dr. Jennifer Steeves for her time and attention, watching my progress and providing advice on my work. Her knowledge and kind words throughout this process were greatly appreciated.

I would also like to thank Dr. Rick Thompson, the Chair of the Board of Directors for the National Organization for Albinism and Hypopigmentation (NOAH), for his assistance recruiting albinism patients. I would like to extend this thanks to my lab mate, Larissa McKetton, who collected the scans. Larissa has not only provided me with professional help, exchanging knowledge and skills, but also greatly inspired me with her extraordinary character and enthusiasm for neuroscience and what she does.

Many thanks to Mirka Ondrack from York University for her statistical consulting, as well as members of the lab, including Monica Giraldo Chica, for her advice on tractography and all the hours spent together in the lab, sharing our frustrations and achievements; Denis Romanovsky, for his help running some analyses and modifying a figure, Kevin DeSimone, for his advice on coding, Joy Williams for her help in MRI acquisition, and Aman Goyal for his MRI analysis expertise.

Table of Contents

Abstract ii

Acknowledgements iii

Table of Contents iv

List of Abbreviations vi

List of Tables vii

List of Figures viii

Chapter 1 Introduction: Why Albinism? 1

1.1 What Is Albinism? 1

1.2 Types, Diagnoses and Treatment 2
- 1.2.1 OCA1 3
- 1.2.2 OCA2 5
- 1.2.3 OCA3 7
- 1.2.4 OCA4 7
- 1.2.5 OA 8
- 1.2.6 Syndromic Albinism 9
- 1.2.7 Diagnosis and Treatment 10

1.3 Visual Impairments in Albinism 12
- 1.3.1 Nystagmus 12
- 1.3.2 Visual Acuity and Photophobia 13
- 1.3.3 Loss of Binocular Vision 17

1.4 Molecular Basis of Albinism 23

Chapter 2: Methods 31

2.1 The History of MRI: from NMR to Spatial Images 31

2.2 The Physics of MRI 33

2.3 Advances in LGN Delineation 36

2.4 Advances in White Matter Reconstruction 40
- 2.4.1 In Vitro Techniques 40
- 2.4.2 Diffusion Tensor Imaging and Tractography 41

Chapter 3: Research Protocol: Abnormal Brain Connectivity in the Primary Visual pathway in Human Albinism 46

3.1 Background....46
3.1.1 The Lateral Geniculate Nucleus....46
3.1.2 The Relationship between the Number of RGCs and LGN Neurons ... 50
3.1.3 Comparison of Three Principal Mammalian Models of the LGN..... 50
3.1.4 The Effects of Misrouting on LGN Organization....52
3.1.5 Altered Cortical Response in Albinism....55
3.1.5 Retina and Chiasm as candidates for Axonal Misrouting....56
3.2 Rationale.... 60
3.3 Objective and Hypothesis.... 61
3.4 Methods....62
3.4.1 Subjects....62
3.4.2 Structural MRI Parameters....63
3.4.3 LGN Delineation and V1 Segmentation....64
3.4.4 Probabilistic Tractography....65
3.4.5 Deterministic Tractography....67
3.4.6 Statistical Analysis-TBSS....69
3.4.7 Statistical Analysis-SPSS....69
3.5 Results.... 71
3.5.1 Probabilistic Tractography....74
3.5.2 Deterministic Tractography....76
3.5.3 TBSS....78
4. Discussion and Conclusion.... 79
4.1 General Discussion....79
4.2 Human Optic Radiation Tractography....81
4.3 Other Disorders.... 84
4.3.1 Dyslexia....84
4.3.2 Achiasma....86
4.4 Conclusion....87
5. Future Directions: V1 to LGN Tractography and fMRI-based V1 Organization....88
References.... 91
Appendices.... 102
Appendix A: Non-normalized Probabilistic Runs....102
Appendix B: Non-normalizaed Deterministic Run....108

List of Abbreviations

ABR auditory brain-stem response
BOLD blood oxygenated level dependent
CHS Chediak-Higashi syndrome
CN cochlear nucleus
CSF cerebrospinal fluid
DTI diffusion tensor imaging
FA fractional anisotropy
GM gray matter
GS Griscelli syndrome
HPS Hermansky-Pudlak syndrome
IC inferior colliculus
LGN lateral geniculate nucleus
MD mean diffusivity
MGN medial geniculate nucleus
MRI magnetic resonance imaging
MSO medial superior olivary
NGSL number of generated streamlines
NMR nuclear magnetic resonance
NR neural retina
OA ocular albinism
OCA oculocutaneous albinism
OR optic radiation
PCD post conceptional day
PD proton density
PGSL percentage generated streamlines
RF radio frequency
RGC retinal ganglion cell
ROI region of interest
RPE retinal pigment epithelium
SNR signal to noise ratio
TBSS tract based spatial statistics
V1 primary visual cortex
VBM voxel-based morphometry
VEP visual evoked potential
WM white matter

List of Tables

Table 1: Summary of LGN volumes reported throughout the years as measured using different techniques..... 48

Table 2: Participant information and health history.....63

Table 3: A Summary of LGN volumes 73

Table A1: SPSS GENLIN “long form” data view for T1 run.....102

Table A2: SPSS GLM (general linear model) “wide form” data view for FS run.....104

Table A3: SPSS GENLIN “long form” data view for FS run with all-raters-median LGN masks.....106

Table B1: SPSS GENLIN “long form” data view for deterministic run in diffusion space.....108

List of Figures

Figure 1: Clinical characteristics of OCA1A and OCA1B..... 4

Figure 2: A simplified model of key proteins in the melanosome..... 7

Figure 3: Common nystagmus waveforms..... 13

Figure 4: The flow of information in the retina..... 17

Figure 5: Visual acuity charts..... 17

Figure 6: An illustration of the relationship between eye position and the degree of binocular visual field..... 21

Figure 7: Optic chiasm in albinism vs. controls..... 22

Figure 8: EphB:ephrinB bidirectional signalling..... 22

Figure 9: misrouting at the optic chiasm in albinism..... 23

Figure 10: A model of axonal guidance at the mouse optic chiasm..... 23

Figure 11: Skin structure..... 28

Figure 12: Tyrosinase gene mutations..... 29

Figure 13: The melanogenic pathway from tyrosine to pheomelanin and eumelanin 29

Figure 14: Retinogenesis in the mouse. 30

Figure 15: MR signal contrast..... 35

Figure 16: LGN detection on different MR contrasts.. 39

Figure 17: An outline of the LGN..... 39

Figure 18: OR delineation based on Klingler's method 41

Figure 19: The diffusion tensor model 44

Figure 20: Schematic comparison of streamline (deterministic) and probabilistic tractography..... 45

Figure 21: OR tractography in healthy humans.....45
Figure 22: The position of the thalamus in the brain 49
Figure 23: Tracings of ganglia as seen in flat mounts of the retina.....49
Figure 24: Layers of the LGN. 49
Figure 25: Mammalian LGN structure.....52
Figure 26: LGN lamination in the albino mouse. 54
Figure 27: LGN of normal and albino green monkeys.....55
Figure 28: LGN of healthy and albino humans. 55
Figure 29: Primary visual pathway in healthy and albino brains.....62
Figure 30:Probabilistic tractography pipeline 67
Figure 31: Deterministic tractography pipeline.....68
Figure 32: LGN mask delineation on a PD scan.....74
Figure 33: Output of PROBTRACKX for probabilistic tracking.....75
Figure 34: Output of DSI Studio fiber tracking.....77
Figure 35: Voxelwise statistical analysis with TBSS.....78
Figure 36: OR tractography.....84
Figure A1:LGN volume vs. LGN to V1 connectivity, T1 space.....103
Figure A2: LGN volume vs. LGN to V1 connectivity, FS space.....105
Figure A3: LGN volume (all-raters-median) vs. LGN to V1 connectivity.....107
Figure B1: LGN volume vs LGN to V1 connectivity, diffusion space..... 109

Chapter 1 Introduction: Why Albinism?

1.1 What Is Albinism?

Albinism, originating from the Latin word for white, “albus” (Cruz-Inigo et al. 2011), is a genetic condition primarily characterized by overt hypopigmentation observed in affected individuals. It is caused by inherited mutations to genes involved in melanin synthesis. Currently, a total of 15 genes associated with the various types of albinism have been identified. However, the substantial number of genetically undiagnosed individuals suggests that additional genes remain to be discovered (Mártinez-García & Montoliu 2013).

Albinism appears in two main forms: oculo-cutaneous albinism (OCA), an autosomal recessive trait presenting both ocular and cutaneous features; and ocular albinism (OA), an X-linked trait more prevalent in males and characterized primarily by the ocular symptoms. OCA affects about 1 in 20,000 people worldwide (Mártinez-García & Montoliu 2013), with prevalence rates as high as 1 in 15000 in South Africa’s Caucasian population, and 1 in 3900 in its black population (Kromberg & Jenkins 1982). In some African countries, the prevalence can be much higher, like in the case of the small isolated group Tonga in Zimbabwe, where as many as 1 in 1000 individuals have the condition (Lund et al. 2007). East Africa is still largely rooted in superstition and witchcraft, and the belief that albino body parts can bring wealth and luck threatens the lives of individuals with albinism. Moreover, extreme poverty in this region encourages an underground trade in albino flesh. Since 2000, over 100 cases of violent attacks on individuals with albinism and 71 murders have been reported in Tanzania, where over 150,000 people live with albinism (Dave-Odigie 2010). OCA2, a subcategory of OCA, is the most common type of albinism (Newton et al. 2001). Due to minimal melanin production, people with OCA2 are at high risk of developing skin cancer (Okulicz et al. 2003). Its rates are so high that most people with albinism in Tanzania die by the age of

40. These statistics reiterate the need for increased awareness of the condition in order to improve the medical, social and psychological needs of these individuals.

Melanin in the retinal pigment epithelium (RPE) is crucial for proper development of the central visual pathway. Its absence in albinism therefore results in visual impairments, including photophobia, nystagmus, reduced visual acuity and loss of binocular vision (Gottlob 2007). In humans, a retinal line of decussation lies along the nasotemporal border through the fovea, with fibres from nasal retina crossing to the other hemisphere and those from temporal retina extending ipsilaterally. The degree of reduced visual function in albinism has been linked to the level of hypopigmentation. Specifically, pigmentation is inversely proportional to the shift into temporal retina of the line of decussation (Von Dem Hagen et al. 2007). As a result of the shift in line of decussation into the temporal retina, crossing of optic nerve fibres is increased- a characteristic common across all species (Gottlob 2007). The link between coordinated structural development of the visual system and normal function is explained in 1.3-1.4.

Rare syndromic forms of albinism also manifest systemic complications such as bleeding problems, immunodeficiency and neurologic defects. Syndromes include Hermansky-Pudlak syndrome (HPS), Chediak-Higashi syndrome (CHS) and Griscelli syndrome (GS). Systemic abnormalities may not develop for years, delaying diagnosis of affected individuals. Confirming diagnosis of albinism facilitates the prediction of such life-threatening systemic symptoms, allowing timely genetic screening and treatment (Gittler & Marion 2014).

1.2 Types, Diagnoses and Treatment

Albinism is clinically heterogeneous, exhibiting a spectrum of phenotypes and is categorized based on the various acquired mutations. Genetic complexity is further increased due to the fact that most affected individuals being compound heterozygotes, with two different mutant alleles (Oetting & King 1994). The two main categories of albinism are OCA and OA. OCA can be further divided into 4 classes. The different forms of albinism are described below.

1.2.1 OCA1

OCA1 can be further distinguished clinically into OCA1A (formerly termed 'tyrosinase-negative OCA') and OCA1B (formerly termed ' yellow OCA'). OCA1A is the most severe form of the disorder. In this type of albinism, tyrosinase, a key enezyme in melanogenesis, is inactive. As a result, pigment is completely absent from the skin, hair and eyes. A total of 78 mutations of the tyrosinase gene (*TYR*) have been associated with this phenotype. In OCA1B, though little to no pigmentation is present at birth, some melanin synthesis may occur throughout life due to residual tyrosinase activity. Ten *TYR* gene mutations have been linked to OCA1B (Toyofuku et al. 2001).

The classic concept of the OCA1 phenotype has been that tyrosinase, which is crucial for pigment production, is successfully transported to melanosomes but is inactive. The catalytic activity of tyrosinase requires the binding of two copper ions at two sites termed CuA and CuB. Copper binding facilitates substrate oxidation. Mutations reported in OCA1 have been shown to alter proper folding of the tyrosinase polypeptide and therefore disrupt copper binding and render tyrosinase inactive (Spritz et al. 1997).

Normally, the tyrosinase protein is transported through the rough endoplasmic reticulum (ER) and the Golgi apparatus where it undergoes post-translational processing and glycosylation prior to its delivery to melanosomes (Borovansky & Riley 2011). The ER is known as the 'quality-control system', where misfolded proteins fail to reach their final destination and are instead degraded by proteolysis. Toyofuku and colleagues (2001) transfected COS7 (African green monkey kidney) cells with tyrosinase cDNA expression vectors containing various OCA1 mutations. Immunostaining and pulse-chase experiments revealed prolonged interaction of these tyrosinase polypeptides with calnexin in the ER and their degradation following its dissociation. These findings introduce a new concept of the OCA1 phenotype, according to which tyrosinase malfunction results from prolonged retention and subsequent degradation of mutant polypeptides in the ER. This suggests that in OCA1, tyrosinase never reaches its final target in the melanosomes.

OCA1 can be clinically identified by the presence of white scalp hair at birth. Individuals born with some pigment in their scalp are associated with other types of OCA. The presence of white hair is a useful diagnostic tool as it has been shown to correctly identify 85% of probands with OCA1 (King et al. 2003). However, since OCA2 may also have this phenotype, molecular analysis is necessary for precise diagnosis. Furthermore, certain clinical features may be used to distinguish between the two types of OCA1 (Figure 1). Criteria defining OCA1A include the presence of white hair and skin throughout life, blue eyes with translucent irides, erythema but no tan and pink amelanotic nevi upon exposure to sunlight. OCA1B is defined by white scalp hair at birth that may acquire pigment throughout childhood, eyelashes darker than scalp or eyebrows, blue or brown eyes, and white skin with the ability to tan and develop freckles following sun exposure (King et al. 2003).

Figure 1: Clinical characteristics of OCA1A and OCA1B. Top: OCA1A is characterized by white hair and skin, erythema (left), and translucent irides as demonstrated by the seemingly reddish eyes (second right). Bottom(left to right): OCA1B patients experience darkening of the hair throughout childhood (left), are able to tan as seen by the darker exposed arm compared to unexposed abdomen, have dark eyelashes compared to hair colour, and have blue or brown pigment in their eyes (King et al. 2003).

1.2.2 OCA2

Tyrosinase-positive OCA, also known as OCA2, or P-related OCA, is the most common type of albinism. The name indicates the locus for mutations occurring in this type of albinism, which are mapped within the region of human *P* gene, the human homologue to the mouse pink-eyed dilution, or *P*, gene. OCA2 usually has a better prognosis than OCA1 as affected individuals are born with some hair pigment and pigmentation may increase throughout childhood, varying from white to blond to brown (Okulicz et al. 2003).

The P protein, a melanosomal membrane protein, is essential for generating the acidic environment in melanosomes. Specifically, it is thought to act as an anion transporter working alongside an H^+/ATPase pump to maintain electrogenic neutrality (Figure 2). Acidification of melanosomes appears to be important for normal pigmentation as demonstrated by its presence in wild type colored mice compared to its absence from hypopigmented mice with mutated *P* gene. However, whether it directly affects the enzymatic activity of tyrosinase remains to be elucidated (Brilliant 2001).

High prevalence of OCA2 is found in Brandywine, Maryland, where 1 in 85 individuals of African heritage have the condition, and in some native American Indian groups, with frequencies ranging from 1 in 200 to 1 in 500. It is also relatively common in sub-Saharan Africa, with prevalence from 1 in 2000 to 1 in 7000 (Brilliant 2001).

Basal pigmentation plays an important protective role against ultraviolet radiation (UVR), as demonstrated by the 10-fold difference in the incidence of skin cancer between Caucasians and dark skinned individuals. The lack of melanin in Africans with albinism greatly increases the risk for skin cancer compared to the general African population. Since OCA2 is the most prevalent type of albinism in Africa, it is often associated with high susceptibility to skin cancer.

UVR is a carcinogen inducing DNA damage, but it also triggers the tanning pathway resulting in increased levels of epidermal melanin. Specifically, melanin-containing melanosomes are transferred to keratinocytes and localized over the nucleus to

protect the genomic material from subsequent UVR. Melanin thus acts both as a physical barrier and as an absorbent filter to reduce UV penetration through the epidermis (Nga Tran 2009).

Dark pigment eumelanin provides better photoprotection than the yellow-red phaeomelanin (Brenner & Hearing 2008). While dark skin restricts UV penetration to only 7.4% of UVB (280–320 nm) and 17.5% of UVA (320–400 nm), penetration through fair skin is almost three times greater (Halder & Bridgeman-Shah 1995). Though UVA penetrates deeper than UVB, the latter is more cytotoxic and mutagenic.

One factor that compromises the photoprotective effect of light skin is its susceptibility to lysosomal-induced degradation of melanosomes, which only persist as "melanin dust" in the epidermis. Dark skin is resistant to such melanosomal degradation. Further, eumelanin acts as a free radical scavenger and superoxide dismutase to reduce reactive oxygen species (ROS) generated mainly by UVA for indirect DNA damage (Brenner & Hearing 2008).

Human pigmentation is a polygenic trait. Single nucleotide polymorphisms (SNPs) of the human melanocortin-1 receptor (*MC1R*) gene have been shown to be involved in regulation of pigmentation phenotypes. MC1R is a G-protein coupled receptor activated by variants of the melanocyte –stimulating hormone (MSH), typically α-MSH, and adrenocorticotropic hormone (ACTH). Binding to these melanocortins initiates a signal cascade that leads to the production of eumelanin instead of phaeomelanin produced by default.

Allelic variations in MC1R result in altered receptor activity and are associated with red hair and fair skin, indicators of high levels of pheomelanin (Duffy et al. 2004). King and colleagues demonstrated an interaction between the *MC1R* and *P* genes in OCA2 patients with atypical red hair phenotype using DNA sequencing (R. a King et al. 2003). Since skin colour is related to the degree of protection against UV light, both *MC1R* and *P* genes have been implicated in malignant melanoma (MM) predisposition ((Hawkes et al. 2013; Ibarrola-Villava et al. 2010; Jannot et al. 2005).

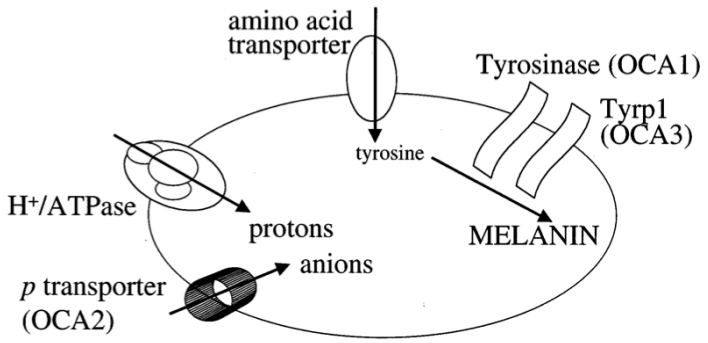

Figure 2: A simplified model of key proteins in the melanosome. Specialized skin cells in the basal layer of the epidermis, called melanocytes, produce melanin. The pigment is then stored in large organelles named melanosomes. Low pH environment, which may favour the enzymatic activity of tyrosinase, is regulated through the activity of the P protein and H^+/ATPase pump in the melanosomal membrane (Brilliant 2001).

1.2.3 OCA3

OCA3, also known as rufous (Latin for red) OCA, is a rare form of OCA occurring mostly in African blacks. It is caused by mutations in human tyrosinase-related protein-1(*TYRP1*), the human homologue to the murine Brown *TRP-1*gene. In murine, mutations to this locus result in a switch from black to brown coloration. Similarly, TYRP1 is a key regulatory protein in the production of eumelanin in humans. People with OCA3 have little pigment at birth, but they experience an increase in pigmentation with age. In turn, visual deficits are also not as pronounced in this type of albinism (Kromberg et al. 1990). Clinical features include red-bronze skin with nevi, ginger-red hair and blue or brown irises (Zhang et al. 2011).

1.2.4 OCA4

Newton and colleagues have identified a fourth form of oculocutaneous albinism, OCA4, caused by mutations to the human homologue of the mouse underwhite gene (*uw*), *matp* (membrane-associated transporter protein). Comparisons of melanosomes from healthy and *uw* mutant mice revealed differences in the ultrastructure of these organelles. Such observations lead to the possibility that MATP protein functions in osmotic regulation (2001). OCA4 is similar in phenotype to OCA2, with newborns

having some pigment in their hair, varying from silver white to yellow. Skin pigmentation varies from minimal to near normal (Suzuki & Hayashi 2011). A study by Inagaki and others showed that *matp* is the most common locus for mutations in OCA patients in Japan (Inagaki et al. 2004).

1.2.5 OA

This type of albinism primarily affects the eyes, while skin and hair of OA patients are not significantly different from those of unaffected relatives. The most common form of OA is known as Nettleship-Falls type or type 1, an X-linked recessive disorder affecting 1 in 60,000 males (Oetting 2002). Individuals with the condition suffer from severely impaired visual acuity accompanied by nystagmus, strabismus and photophobia (Schnur et al. 1998). X-linked OA is distinguished from other, autosomal recessive, forms of OA by the presence of macromelanosomes as detected by light and electron microscopy in the skin and retinal pigment epithelium (RPE) of patients (Charles et al. 1992).

OA1 is caused by mutations of the *OA1* gene, recently renamed *GPR143*, isolated from both murine and humans. OA1 is a melanosomal membrane protein thought to play a role in melanosome formation. Based on amino acid sequence similarities between *OA1* gene and several G-protein coupled receptors (GPCR), OA1 is believed to be a member of this family of receptors. Studies have shown that OA1 is involved in melanosome biogenesis, specifically in the reorganization of endosomes, melanosomal precursors (Shen et al. 2001). Therefore, OA1 has been suggested to function as a stop signal for melanosome growth. Cortese and colleagues generated double mutant mice of *oa1* and either *Tyr* or *Matp* mice, revealing a double role of OA1 protein in the regulation of melanosome maturation. In early stages it controls the rate of melanosome biogenesis and in final maturation stages it controls the size of melanosomes (Cortese et al. 2005).

1.2.6 Syndromic Albinism

Although the manifestation of albinism is mostly restricted to oculocutaneous features, additional symptoms may exist and suggest the presence of syndromic albinism. Hermansky-Pudlak syndrome (HPS) is a rare autosomal recessive disorder resulting in OCA and abnormal bruising and bleeding. The bleeding diathesis is attributed to a platelet pool deficiency. Additionally, HPS is associated with storage of a waxy ceroid pigment in tissues (Okulicz et al. 2003). A fatal complication of the disorder is pulmonary fibrosis, resulting from the accumulation of ceroid in the lungs and leading to early death (Introne et al. 1999). Mutations in 9 genes have been linked to the different types of HPS. Products of these genes are thought to be involved in intracellular protein trafficking (Gittler & Marion 2014). Individuals with HPS experience varying degrees of hypopigmentation, from minimal to near normal.

While HPS is a rare disease worldwide, affecting 1 in 500,000 individuals, prevalence is high in Puerto Rico, where 1 in 1800 people has the condition due to a founder effect. Homozygosity for a 16 bp duplication in the *HSP1* gene has been shown to be unique to patients from northwest Puerto Rico and different from homozygous *HSP1* mutations in other pats of the world, reflecting the founder effect in this population (Iwata et al. 2000). Most cases of HPS in Puerto Rico are associated with mutations in the *HPS3* gene, caused by a 3904 bp deletion. The HPS protein forms part of a complex called biogenesis of lysosome-related organelles complex-2 (BLOC-2), which regulate the sorting and transport of proteins into lysosome-related organelles (LROs). Such LROs include melanosomes within pigment-producing melanocytes and dense granules in platelets responsible for signaling blood clot formation (Anikster et al. 2001; Gittler & Marion 2014). A splice-site mutation in the *HPS3* gene results in an abnormally short protein and is common in Eastern European (Ashkenazi) Jews (Serrant et al. 2010).

Chediak-Higashi syndrome (CHS) is another example of a condition that presents silvery hair, fair skin and the typical ocular abnormalities characteristic of the OCA phenotype. It also resembles HPS with the bruising and abnormal bleeding experienced

by affected individuals. Additionally, CHS patients may experience peripheral neuropathy. CHS is a rare autosomal recessive disorder with only 200 cases reported worldwide as of 1989 (Introne et al. 1999). In patients with CHS, the immune system is severely damaged, resulting in repeated infections and possibly in the accelerated stage of the disorder in which white blood cells invade different body organs and lead to organ failure (Introne et al. 1999).

CHS is caused by mutations to the *CHS* gene, also known as *LYST* gene, which is thought to be involved in vesicle formation and trafficking, particularly of lysosomes. Indeed, patients with CHS manifest enlarged lysosomes and lysosome-related organelles such as melanosomes and dense granules, which disrupt the proper function of these cells (Westbroek et al. 2007).

Griscelli syndrome (GS) is also characterized by partial OCA, immunodeficiency and neurologic impairments. It is a rare autosomal recessive condition with an unknown prevalence. GS1 and 2 are caused by mutations in the MYO5A1 and RAB27A genes responsible for melanosomal migration. GS3 is caused by mutations in melanophilin (*MLPH*) gene, also involved in melanosome transport within melanocytes. Defects in these genes results in clumps of melanosomes near the centre of melanocytes, trapping melanin and preventing normal pigmentation (Gittler & Marion 2014).

1.2.7 Diagnosis and Treatment

Due to varying degrees of pigmentation, the clinical overlap between OCA subtypes and the absence of cutaneous signs in OA, the appearance of skin and hair cannot serve as a diagnostic of albinism. The ocular symptoms rather define the diagnosis of this condition. Therefore, an eye examination is the main test for the presence of albinism. Ophthalmologists look for signs of nystagmus, which is usually the presenting clinical symptom. They also perform slit-lamp examination for iris transillumination, and fundus examination to confirm retinal hypopigmentation and foveal hypoplasia (Nelson and Olitsky 2005). Standard eye tests are used to evaluate visual acuity. To determine the

subtype, genetic testing is required and is especially helpful if family history of albinism exists (Gronskov et al. 2007).

However, clinical signs are variable, and some children with albinism may only exhibit iris transillumination and near normal visual acuity. Visually evoked potential (VEP) recordings are required to determine albinism in these individuals (Creel et al. 1990).

A tool for prenatal diagnosis of tyrosinase-negative albinism is the dopa reaction test in hair bulbs of fetuses. Electron microscopy can also be used to make observations on melanosomes in hair bulb melanocytes from the scalp. Melanosomes of affected fetuses fail to show complete development, providing an easy way of distinguishing normal fetuses from affected ones (Gershoni-Baruch et al. 1991).

Clinical features of HPS include bleeding diathesis, horizontal nystagmus and mild hypopigmentation at birth (Anikster et al. 2001). Bleeding abnormalities present with bruising from early childhood. Though bleeding is mild, hemorrhagic complications associated with surgery occur. Bleeding is therefore controlled by the use of platelet concentrates and pre-surgical administration of desmopressin. Ceroid accumulation increases with age and predisposes patients to granulomatous colitis, which develops in adolescence. It may also lead to pulmonary fibrosis, which only becomes symptomatic in early adulthood. Subtle hypopigmentation and late symptoms often cause delayed diagnosis of the condition. Newborn screening for HPS3 using DNA pooling from dried blood samples in areas of high prevalence such as Puerto Rico facilitate early diagnosis and treatment of the condition (Serrant et al. 2010). Absence of platelet dense bodies detected by wet-mount electron microscopy is used to confirm the presence of HPS (Oetting and King 1999). Tissue biopsy showing ceroid accumulation also serves as a diagnostic tool (Glitter and Marion 2014).

CHS is diagnosed with blood smear examination that shows the presence of giant leukocyte precursor cells. In severe cases of the disease in which the accelerated phase is manifested, bone marrow transplant is implemented (Glitter and Marion 2014).

Diagnosis of GS is achieved through the examination of a hair shaft showing abnormal aggregates of pigment under light microscopy (Glitter and Marion 2014).

1.3 Visual Impairments in Albinism

1.3.1 Nystagmus

Congenital nystagmus, or more accurately renamed infantile, is an involuntary oscillation of the eyes that develops in the first months after birth. It is usually aggravated by any effort of fixation, and is reduced in the dark (Spielmann 2000). It occurs in a manifest form in which symptoms are present at all times, or in a latent form that is evoked upon occlusion of one eye. OCA is the leading cause of manifest congenital nystagmus. This form of nystagmus is also termed sensory defect nystagmus, since it is caused by abnormal sensory afferents that lead to inadequate image formation on the fovea (von Noorden 1990). This in turn interferes with oculomotor stabilization of fixation.

OCA patients show bilateral, conjugate and horizontal oscillations of the eyes. The intensity and waveform change with gaze direction. Waveform can be pendular or jerky (Figure 3). The former is a sinusoidal like oscillation in which both eyes move with the same speed in both directions. In infants with albinism, oscillations are often pendular in nature. The latter consists of a slow phase followed by a rapid saccadic correction movement. In albinism the slow phase is typically of accelerating velocity (Papageorgiou et al. 2014).

Young patients often develop an anomalous head posture that allows them to put their eyes into a “null” position where the eyes are nearly still. This helps improve visual acuity, which is affected in these patients due to rapid motion of image on the retina (Bedell & Loshin 1991).

A corrective surgical procedure was designed by the ophthalmologists Kestenbaum and Anderson in the 1950’s. It involves surgery on the extraocular muscles to move the null point closer to the position of primary gaze. Some surgeries focus

particularly on the horizontal rectus muscles. More than half the patients with albinism experience up to one line of improvement in measured visual acuity following one of these surgical procedures. Such improvement, though limited due to abnormal anatomy of the visual pathway in albinism, is beneficial since in some cases it is sufficient for these patients to gain their driver's license (Summers 1996).

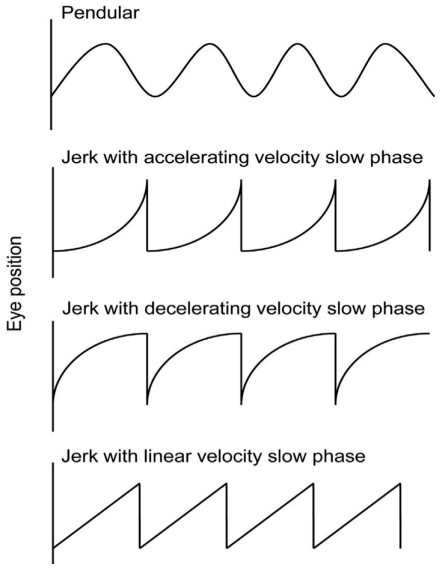

Figure 3: Common nystagmus waveforms. Pendular nystagmus is a sinusoidal like oscillation seen in infants with congenital nystagmus and in brainstem and cerebellar conditions. Jerk nystagmus shows both a quick and a slow phase, and the latter can be of accelerating or decelerating velocity. The one with accelerating nature is invariably observed in congenital nystagmus such as that seen in albinism.

1.3.2 Visual Acuity and Photophobia

Visual acuity is described by the minimum visible, the minimum separable and the minimum resolvable acuity. Minimum visible acuity, also known as detection acuity, refers to the ability of the eye to perceive a visual stimulus as distinguishable from the background, and its threshold is 1 arcsec in healthy humans. Minimum separable, or hyperacuity, is the ability to distinguish between visual stimuli, and the threshold for recognizing two objects as separate is 2–10 arcsec. Lastly, minimum resolvable acuity, also termed discrimination acuity, refers to the ability to make sense of the stimulus, and the resolving threshold is 30 arcsec to 1 arcmin (von Noorden 1990).

Each retina and its corresponding visual field can be schematically divided into quadrants. A vertical line divides the retina into nasal and temporal divisions, and a horizontal line splits it into superior and inferior halves. The vertical and horizontal lines intersect at the centre of the fovea (Latin for pit), which is aligned with a point in the visual field known as the fixation point (Purves et al. 2001). A proper distribution of photoreceptors across the retina is crucial for vision. The ratio of rods to cones is 20:1 throughout most of the retina, with the exception of the fovea, which consists solely of densely packed cones. While rods are specialized for sensitivity of light at the expense of spatial resolution, cones demonstrate the opposite properties. The fovea is therefore the retinal area responsible for high acuity (Purves et al. 2001). The flow of information (Figure 4) is from photoreceptors, through bipolar cells to the only action potential firing cells in the retina, the retinal ganglion cells (RGCs). The two major classes of RGCs are midget and parasol cells. In the rod system, few to many rods contact a single bipolar cell. Convergence allows small signals from many rods to be joined to trigger a large response in the bipolar cell under low light conditions. However, it prevents detection of the source of signal, thus reducing the spatial resolution of this type of receptors. The cone system, however, is much less convergent. In central retina, each cone diverges to a single on and single off midget bipolar cell. Each bipolar cell then contacts a single on or off midget ganglion cell. This single cone spatial resolution maximizes acuity (Purves et al. 2001). While the midget pathway demonstrates a 1:1 ratio of bipolar to ganglion cells in the fovea, about four to five diffuse bipolar cells contact a single parasol ganglion cell (Weiner 2003).

Grating acuity refers to the ability to distinguish elements of alternating dark and light bars. Vernier acuity is the aspect of acuity that refers to the ability to detect disalignment of two lines. Grating and vernier acuity tests using horizontal lines to dampen nystagmus-induced temporal modulations showed a five-fold reduction in central vision in albinism (Wilson et al. 1988). It was further shown that the anatomy of the visual system of adult albinos is comparable to that of healthy human infants (Hendrickson & Yuodelis 1984), linking their impaired visual acuity to arrested

development. Normally, the fovea is formed by two opposing migrations. Inner nuclear and ganglion cells are displaced peripherally to create the foveal pit and slope, while photoreceptors in the surrounding outer retina migrate centripetally towards the centre of the fovea to increase cone density in this area (Dubis et al. 2012). Melanin has been shown to play a role in the topographic patterning of ganglion cell axons in mice and rats (Silver and Sapiro 1981). Since melanin normally exists in high levels in the macular region of the pigment epithelium, a possible mechanism by which postnatal cone migration is prevented due to lack of melanin in the albino retina has been proposed (Wilson et al. 1988). Light microscopic examinations confirmed previously reported reductions in cone density in the albino fovea (Fulton 1978). However, cone numbers and their distribution were later reported to be unaffected in albinism, as shown by the examination of retinal whole mounts from albino and pigmented ferrets (Jeffery et al. 1994).

While no significant difference was observed in the number of cones, there was a significant deficit in the number of rods throughout the albino retina (Jeffery et al. 1994). In 2002, Donatien and Jeffery were able to show a relationship between the amount of ocular melanin and the number of rods in mice, revealing a 30% reduction in the number of rods in albino retinae (Donatien & Jeffery 2002). Functional evidence for the abnormal number of rods also exists. Single unit recordings revealed impaired threshold sensitivity of light in hypopigmented rodents and rabbits compared to normally pigmented animals at low levels of stimulus and background illumination. At higher levels of illumination, no differences were observed between the strains, probably due to the function of cones under these conditions.

Individuals with albinism demonstrate variably reduced visual acuity, depending on the amount of ocular pigmentation. Many albinism patients fall within the legally blind range, corresponding to 20/200 visual acuity. This means that, with corrected vision, they are only able to read the first line, the uppercase letter E, on a Snellen chart. However, reports show that some individuals with albinism have near normal or normal vision (20/20 visual acuity) (Summers 2009).

The Snellen chart was first introduced in 1862 by Dutch ophthalmologist Herman Snellen and has been since used universally to measure visual acuity in clinical practice. Snellen acuities are usually expressed as fractions with the numerator equal to the distance from the chart and the denominator equal to the size of the smallest line that can be read. However, the Snellen chart has disadvantages including the "crowding phenomenon" caused by the closely spaced letters as well as the irregular and arbitrary progression of letter size between lines. Additionally, this chart has never been standardized, therefore different manufacturers may use different letters, different fonts, and different spacing ratios, which may be illuminated or projected differently. All these do not allow equivalent task presentation and may as a result affect the performance and the acuity scores (Kaiser 2009).

To improve the accuracy of the test, newer charts have been developed. ETDRS, which stands for early treatment diabetic retinopathy study, is designed to eliminate flaws introduced by the Snellen chart, and therefore has become the "gold standard" for visual acuity testing (Kaiser 2009). In this test, visual acuity is expressed in LogMar notation, the logarithm of the minimum angle of resolution. That is, the logarithm to the base 10 of decimal visual acuity, where the range of 0.0–1.0 corresponds to the Snellen 20/20–20/200 (Figure 5).

Another visual impairment experienced in albinism is photophobia, in which little to no pigment in the iris prevents filtration of incoming light. Due to the reduced ability to absorb light, bright environments often cause discomfort to people with albinism. A common myth associated with albinism is that affected individuals have red eyes. Indeed, their eyes may appear reddish or pink upon exposure to light. However, since the albino iris has little to no pigment, the reddish tint is not the color of the eye but rather the color of blood vessels on the retina that show through the translucent iris (Meyer et al. 2002).

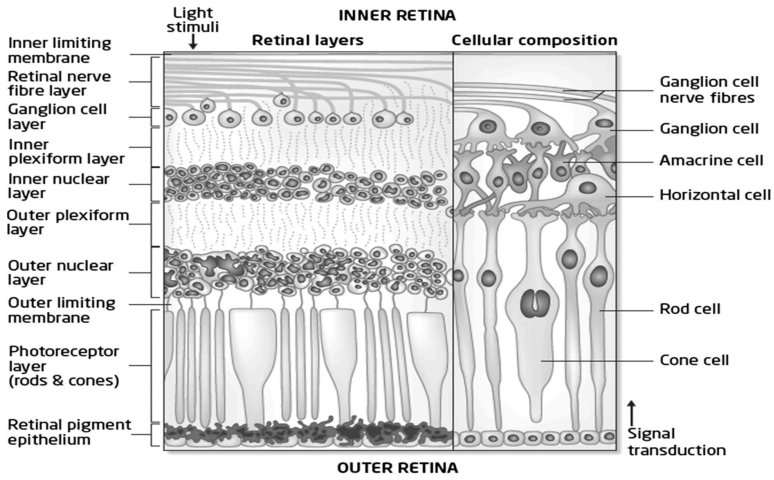

Figure 4: The flow of information in the retina. In vertebrates, the retina is divided into ten distinct layers. Light comes in from the anterior part of the retina and travels through the neural retina to reach the photoreceptors at the posterior portion of the retina (Saidha et al. 2011).

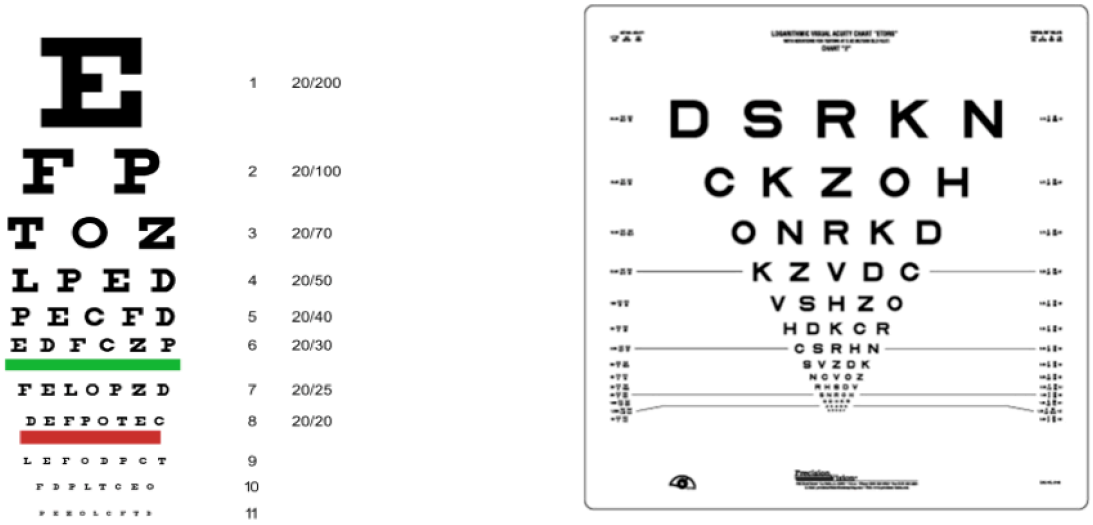

Figure 5: Visual acuity charts. Many people with albinism fall within the legally blind range, being able to only read the first line, the big E (corresponding to 20/200 visual acuity), on a Snellen chart (left), with corrective lens. Note that in our study, visual acuity was assessed using an ETDRS eye chart (right) and expressed in LogMar (0.0–1.0 corresponding to 20/20–20/200) (Kaiser 2009).

1.3.3 Loss of Binocular Vision

Upon exiting the retina, RGCs converge in a region called the optic disc, also known as the blind spot due to the lack of photoreceptors in this area and its subsequent inability to detect light. It is also the point of exit of ganglion cell axons that travel

through the optic nerve to transmit information from the retina to the brain (Pallin and Wright 2007).

The optic nerves of both eyes extend to the forebrain and meet at a structure called the optic chiasm. At this junction point, fibers are redirected before retinal axons are further projected into a bilateral structure in the thalamus called the lateral geniculate nucleus (LGN) (Purves et al. 2012). A line on the retina called the naso-temporal division separates RGCs with different chiasmatic routes. Axons from the nasal retina cross to the opposite side of the brain, while those from the temporal retina extend ipsilaterally. The degree of precision of the naso-temporal division, and hence the degree of uncrossing, is proportional to the size of the binocular field of view across species (Figure 6).

In animals with laterally located eyes, the size of the uncrossed ipsilateral projection is relatively small. For instance, it is as low as 2–3% in rodents (Jeffery et al. 1981). In animals with frontally located eyes, the uncrossed projection may be approaching the crossed projection in size (Fukuda et al. 1989;Jeffery & Erskine 2005). In humans about 50% of fibers cross at the chiasm, while the other half project ipsilaterally.

In the frog *Xenopus* metamorphosis, the transition from laterally located eyes (and thus completely crossed RGCs) to frontally located eyes is accompanied by the generation of a new population of RGCs that project ipsilaterally. This suggests that crossing of axons is a default state and that a repulsive signal exists in the chiasm to prevent ipsilateral projections from crossing in organisms with frontally located eyes.

Structural MRI studies on humans have shown narrower chiasms in albinism compared to controls, which is likely the result of increased crossing of RGCs observed in albinism (Rice et al. 1995; Schmitz et al. 2003; Mcketton et al. 2014). Optic nerves and tracts were also found to be smaller in humans with albinism (Figure 7).

The retina and optic chiasm express axonal guidance cues such as Eph family receptors and their ligands (R. a King et al. 2003), and are therefore candidate sites for the misrouting seen in albinism (van Genderen et al. 2006). Nakagawa and co-workers (2000) therefore sought to explore such molecular cues. Eph family receptor tyrosine

kinases (RTKs) and their ephrin ligands have been associated with the development of the visual pathway, including the formation of topographic maps, in the mouse and *Xenopus* (Nakagawa et al. 2000; Rasband et al. 2003) and are therefore candidate repellents. Both these receptors and their ligands are membrane-bound proteins. Two subclasses of ligands exist, based on their structure and attachment to the membrane: ephrin-As are linked to the membrane through the glycolipid glycosylphosphatidylinositol (GPI) and lack a cytoplasmic domain, while ephrin-Bs are transmembrane proteins containing a cytoplasmic motif. Eph receptors are similarly divided into A- and B-subclasses based on their affinity to these ligands.

Nakagawa and others transplanted metamorphic *Xenopus* ventrotemporal retina into embryonic eyes and observed completely crossed RGCs, suggesting that repelling signals guiding axons ipsilaterally are absent early in development. They also detected a stage specific expression of ephrin-B at the frog chiasm during metamorphosis, but not in the embryo, using affinity probes. Lastly, they transfected embryonic chiasm cells with ephrin-B. This triggered the formation of ipsilateral projections, previously known to originate from Eph-B expressing ventro-temporal (VT) RGCs. These results suggest a role of ephrin-B as a midline gatekeeper repulsing Eph-B expressing axons. Furthermore, ephrin-B expression has been found in the chiasm of mammals, which have ipsilateral projections, but not in the chiasm of fish and birds, which do not have them. This further confirms that ephrin-B/Eph-B signalling at the midline provides the mechanism for RGC axonal guidance.

However, the exact ephrin-B ligand and Eph-B receptor involved in this type of regulation remained unknown until later. In 2003, Williams and colleagues showed, using in situ hybridization, that ephrin-B2 is strongly expressed at the mouse chiasm at E14.5, when ipsilateral axons begin to arrive at the chiasm. They also cultured retinal explants on recombinant mouse ephrin-B2 and found that outgrowth from VT retina is significantly reduced in a dose-dependent manner. This constitutes the first direct evidence that ephrin-B2 is selectively inhibitory to VT axons and therefore plays a key role in directing the divergence of retinal axons. They have also identified the receptor

for this ephrin ligand, EphB1, which is expressed in RGCs destined to the ipsilateral projection. Through retrograde labeling they were able to show that in protein null *EphB1*$^{-/-}$ mutants, axons from VT retina misproject into the contralateral hemisphere. This suggests that EphB1is not only a factor in the formation of ipsilateral projections through a repulsive interaction with eprhin-B2, but that its absence is sufficient to cause substantial misrouting of the axons.

While Williams and others mapped EphB1 expression to ipsilateral RGCs (2003), a recent study showed that expression of EphB1is also found in the chiasm (Chenaux & Henkemeyer 2011). The experimenters therefore sought to explore a possible role of EphB1-mediated reverse signalling in axonal pathfinding at the chiasm, as EphB:ephrin interaction is known to trigger bidirectional signalling. A novel knock-in mouse mutant (EphB1$^{T\text{-}lacZ}$) was generated, which renders the receptor unable to stimulate forward signalling (Figure 8). Previously, the dramatically reduced ipsilateral projection phenotype observed in protein null EphB1$^{-/-}$ mice suggested EphB1-mediated forward signalling regulation of RGC axon pathfinding (Williams et al. 2003). Since the EphB1$^{T\text{-}lacZ}$ mutant exhibited the same phenotype seen in the null mutation, the authors concluded that EphB1-mediated reverse signalling is not necessary for directing axons at the optic chiasm. Moreover, EphB1/B2 double mutant mice, with EphB2 forward signalling mutation, exhibited a more pronounced reduction in ipsilateral projection. However, the EphB2$^{lacz/lacz}$ mutation by itself did not display a phenotype. They were also able to show that EphB1 and EphB2 are co-expressed within the same VT RGCs, suggesting redundancy in their function at the chiasm. Yet, taking into account that EphB2 does not rescue function in the EphB1$^{-/-}$ and EphB1$^{T\text{-}lacz/T\text{-}lac\text{-}z}$ mice implies preference toward EphB1 at the optic chiasm. Further genetic manipulations included generation of mice with reduced levels of functional EphB1 (EphB1$^{+/T\text{-}lacz}$ heterozygotes) and normal levels of EphB2, and a combination of EphB1$^{+/T\text{-}lacz}$ and EphB2$^{lacz\text{-}lacz}$. In the first scenario, close to normal phenotype was observed, while in the second a significant decrease in ipsilateral projection was detected. Taken together, these results suggest that EphB2 directs axons at the chiasm only when EphB1 levels are reduced.

Upstream transcription factors have been suggested to regulate the identity of RGCs. *Zic2*, a zinc-finger transcription factor (TF), is involved in left-right body asymmetry and patterning of binocular vision. Immunohistochemistry revealed that *Zic2*, but not other members of this family of TFs, is selectively localized in RGCs from mouse VT retina. *Zic2* expression was found to be restricted not only spatially, but also temporally, from E14.5 to E17.5- after neurogenesis and during the formation of permanent ipsilateral projections. Moreover, the expression of Zic2 in the retina is proportional to the degree of binocularity across species. Also, fewer Zic-expressing cells were observed in albino mice compared to pigmented littermates at E14.5 and E16.5, which is in line with the reduced uncrossed projection observed in this population (Figure 9; Figure 10). These findings support the role of Zic2 in regulating the formation of ipsilateral projections (Herrera et al. 2003). Despite these findings, the exact mechanism by which abnormal chiasmatic pathways are formed remains largely unknown.

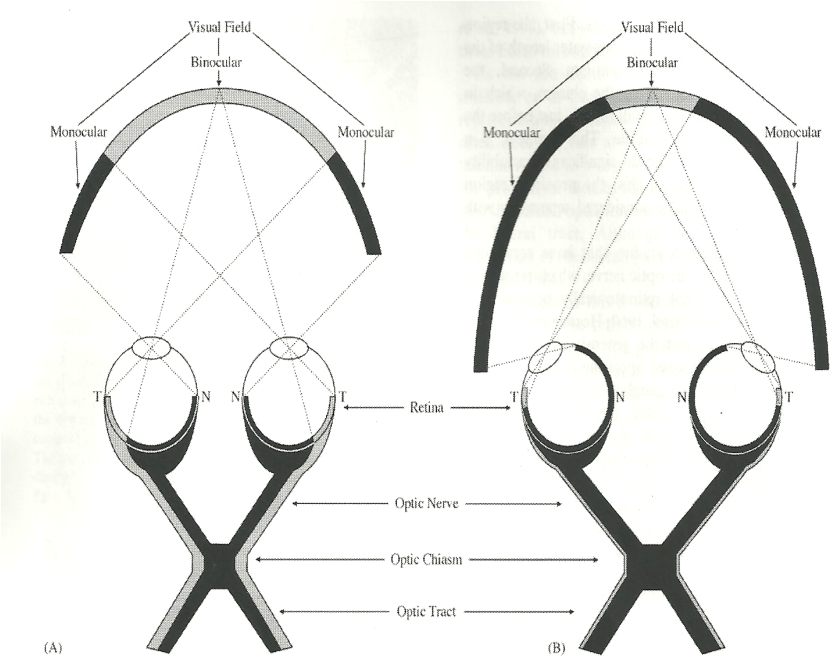

Figure 6: An illustration of the relationship between eye position and the degree of binocular visual field. (A) In animals with frontally located eyes the binocular field is large, and ipsilateral fibres approach contralateral fibres in number. (B) In animals with laterally positioned eyes the overall size of the visual field is greater, and the monocular visual field is

increased significantly. However, the binocular field and consequently the size of ipsilateral projection are reduced (Jeffery and Erskine 2005).

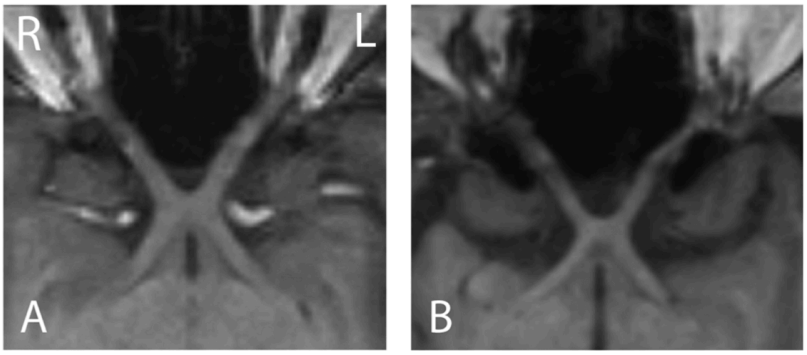

Figure 7: Optic chiasm in albinism vs. controls. The optic nerves, chiasms and tracts of A) a healthy human and B) a patient with albinism. The chiasm is narrower in the albino and the angles between the optic nerves and tracts are larger compared to controls (McKetton et al. 2014).

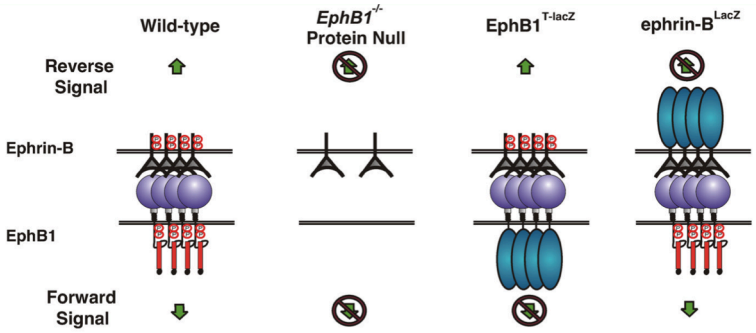

Figure 8: EphB:ephrinB bidirectional signalling. The protein null loses the ability to stimulate both forward and reverse signalling, the EphB1-β-gal fusion protein can only stimulate reverse signaling, and the ephrin-B-β-gal fusion protein is only able to stimulate forward signaling (Chenaux and Henkemeyer 2011).

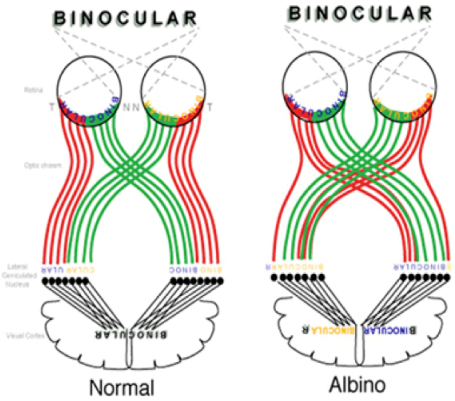

Figure 9: misrouting at the optic chiasm in albinism. In the healthy brain, nerve fibres originating from the nasal retina (green) cross at the optic chiasm and project to the contralateral LGN, while fibres in the temporal retina (red) project to the ipsilateral LGN, approaching the contralateral projection in size. In albinism, misrouting of retinal fibres at the optic chiasm results in the majority of fibres crossing to the contralateral side of the brain (Herrera and Garcia-Frigola 2008).

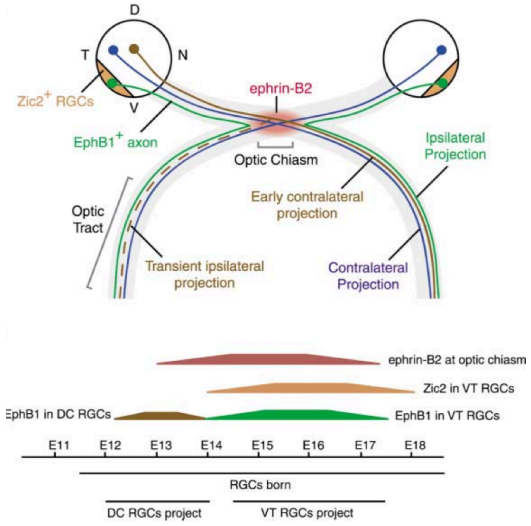

Figure 10: A model of axonal guidance at the mouse optic chiasm. Zic2-expressing RGCs give rise to EphB1 expressing axons, which turn ipsilaterally at the optic chiasm upon ephrin-B2 expression. Axons that do not express EphB1, do not sense ephrin-B2 and cross to the contralateral side of the brain. RGCs are produced from E11.5 until birth. The first RGCs originate from the dorsocentral (DC) retina and most of them project contralaterally. The permanent ipsilateral projection is generated between E14.5–E17.5 from the ventrotemporal (VT) retina. Ephrin-B2 is expressed at the chiasm from E13.5–E17.5 (Rasband et al. 2003).

1.4 Molecular Basis of Albinism

The hypopigmentation observed in albinism has been shown to result from mutations in over 65 loci in the mouse (Silvers 1979), all of which are responsible for melanin production or melanocyte distribution and development, or both. Different mutations of the same gene produce a range of pigmentation levels, from complete absence to near-normal levels of pigment. In mammals, pigmentation is the product of melanin synthesis, which takes place in cytoplasmic organelles called melanosomes, found within melanocytes (Del Marmol & Beermann 1996). Two types of melanin are made: a darker brown/black eumelanin, and a lighter yellow/red pheomelanin.

Melanosomes are then transferred to keratinocytes in the epidermis, where they participate in photoprotection (Figure 11) (Costin & Hearing 2007).

Tyrosinase is a key enzyme in the cascade of melanin production. It catalyzes the rate-limiting step, the conversion of tyrosine to dopaquinone. The tyrosinase gene is located on mouse chromosome 7 and human chromosome 11 (Del Marmol & Beermann 1996). About 88 mutations of the tyrosinase gene have been found, more than in any other gene associated with albinism. Many of the missense mutations are located in or around the copper binding sites (Figure 12). Two tyrosinase-related proteins, TRP-1 and TRP-2, have been identified and linked to specific steps in the melanogenic pathway (Figure 11). TRP-1 is located on mouse chromosome 4 and on human chromosome 9. TRP-2, or DOPAchrome tautomerase, is located on chromosome 14 in mice and chromosome 13 in humans.

Melanin synthesis begins with the oxidation of the amino acid tyrosine to dihydroxyphenylalanine (DOPA), which is then oxidized to DOPAquinone. Both steps are catalyzed by tyrosinase. DOPAquinone is an intermediate from which both eumelanin and pheomelanin are produced. TYRP1, a DHICAoxidase, and TYRP2, a DOPAchrome tautomerase (DCT), catalyze the conversion of DOPAquinone to eumelanin.

More specifically, DOPAquinone can be converted, through a leucoDOPAchrome intermediate, to DOPAchrome and follow either one of two pathways to produce eumelanin. In the presence of DCT, DOPAchrome is converted to 5,6-dihydroxyindole-2-carboxylic acid, DHICA. The latter can then be oxidized by TYRP1, as necessary for melanin polymerization and the production of black eumelanin. Otherwise, DOPAchrome is decarboxylated to 5,6-dihydroxyindole (DHI), which is then oxidized by tyrosinase and polymerized to form brown eumelanin.

A cysteine precursor interacts with DOPAquinone to produce the direct precursor of pheomelanin. The rate of this reaction is greater than that of the ring formation reaction in which LeucoDOPAchrome is produced (Thompson et al. 1985). Hence, cysteine levels regulate the synthesis of both types of melanin. Once DOPAchrome is

formed, the pathway with the DHICA intermediate is favoured over that with the DHI intemediate for the production of eumelanin (Figure 13) (Palumbo et al. 1991).

Tyrosinase in the RPE has been found to be a critical regulator of neural retina (NR) development, as its addition to transgenic albino animals corrected the structural abnormalities seen in this population (Esteve & Jeffery 1998). Since tyrosinase catalyzes the production of dopa and its gene is defective in many cases of albinism, Ilia and Jeffery predicted abnormally low concentrations of dopa in albino retinae (Ilia & Jeffery 1999). They first counted mitotic profiles in the retinae of pigmented and albino rats. In the RPE mitotic figures could be identified from postconceptionday (PCD) 12-15, while in the NR cell production is completed later and mitotic profiles could therefore be identified until PCD 30. In both compartments, more profiles were identified in albinism, resulting in increased retinal thickness. Moreover, in a study on the order of birth of cells in the mouse NR, ^{3}H-thymidine labeling revealed a center-to-periphery pattern of development, based on the weakly labeled nuclei found in the periphery. This suggests continued cell division in peripheral cells following injection (each day from birth through postnatal day 11), which dilutes the amount of radioactivity. Indeed, cells in the center ceased to divide on days 5-6 after birth, while those in the periphery stopped dividing on day 11 (Young 1985). While Ilia and Jeffery (1999) detected a similar pattern of development in the pigmented strain, the albino phenotype demonstrated a delay in the center-to-periphery pattern of cell production. Also, although albino retinae were thicker than pigmented retinae, cell death was greater in the albino from PCD 17-28 as determined by the number of pyknotic nuclei in both phenotypes (Ilia and Jeffery 1999). Therefore, differences in thickness between the two groups declined.

In the same study, dopa levels were measured with high performance liquid chromatography (HPLC). At PCD 15, dopa concentrations were at trace levels in both phenotypes, but at later stages its concentrations were found to be abnormally low in the albino retinae compared to the normally increasing levels in pigmented retinae. In addition to its role in melanogenesis, dopa has been shown to act as an antimitotic agent. This has been demonstrated by the inhibition of DNA synthesis observed in murine and

human melanoma cells treated with dopa (Wick 1980). Ilia and Jeffery (1999) therefore studied the effect of varying dopa concentrations on the abnormal mitotic/pyknotic profiles in albinism. Organ culture experiments on PCD 19 retinae revealed reduced mitotic and pyknotic profiles in albino eyes with increasing concentrations of dopa (0.1-0.5 mM), demonstrating its regulatory role in mitosis (Ilia and Jeffery 1999). Upon addition of dopa, the level of mitotic/pyknotic profiles in the experimental albino was comparable to that in the pigmented control group. Mitotic profiles were also reduced in the experimental pigmented group, but the reduction was not significant.

The reduced levels of dopa in albino RPE seems to be responsible for deregulated mitosis or for signalling cell cycle exit. This is supported by observations on RPE cultures treated with dopa, in which cells took 27 instead of 19 hours to double (Akeo et al. 1989). During ocular development, the NR and RPE form gap junctions, as demonstrated by electron-microscopic observations of chick embryos (Fujisawa et al. 1976). Particularly, numerous gap junctions are present during retinal mitosis, but not at a later stage of development when cells are differentiated into the various types of neurons. Differentiation occurs in two waves. RGCs, cone photoreceptors, as well as amacrine and horizontal interneurons are generated during an early wave, while the late born rod photoreceptors, bipolar cells and Müller glial cells are detected during a second wave (Young 1985) (Figure 14). In the chick embryo, gap junctions were scarce at 3 days of incubation, reaching a maximum at day 6 in the proliferative zone of the retina but not in layers of early-differentiated RGCs and amacrine cells. Gap junctions were absent in 9 day-old embryos in which most cells had become postmitotic (Fujisawa et al. 1976). These findings suggest that the more developmentally advanced RPE influences cell proliferation in the NR through gap junctions.

Normal levels of Dopa restrict junction permeability, as shown by dopamine-induced reductions in Neurobiotin tracer coupling in rabbit dopaminergic amacrine cells connected by gap junctions (Hampson et al. 1992). Dopamine stimulates D_1-receptors (D1R), which in horizontal cells of lower vertebrates have been shown to activate adenylate cyclase (AC), which in turn raises cAMP levels leading to cAMP-dependent

activation of protein kinase (PK). The activation of PK, particularly PKC, might then phosphorylate the gap junction protein connexin. For some connexins, particularly Cx43, phosphorylation causes the protein's internalization and degradation (Laird 2005). Therefore, a subsequent reduction in junction permeability is expected. Hence, low levels of dopa may result in junctions remaining permeable in albinos while becoming increasingly restrictive in pigmented animals. This may in turn induce the abnormal level of mitosis observed in albinos (Ilia and Jeffery 1999). Furthermore, normal Ca^{2+} concentrations have been shown to increase dopamine-triggered cAMP accumulation (Hampson et al. 1992), implying a role of Ca^{2+} in gap junction permeability and perhaps in the regulation of retinal mitosis.

Both RPE and the ventricular zone (VZ) of the NR, a layer adjacent to the RPE in which mitosis takes place, display spontaneous Ca^{2+} transients. Such spontaneous Ca^{2+} activity can spread both within and between the two tissues via gap junctions. Pearson and colleagues showed that Ca^{2+} activity in chick VZ is reduced in the absence of RPE. They also showed that gap junction blockers such as carbenoxolone reduce Ca^{2+} signal propagation between the two tissues (Pearson et al. 2004). The spreading of Ca^{2+} activity between neighbouring cells is a feature of the developing nervous system. In the proliferating neuroepithelial cells, Ca^{2+} spreading via gap junctions that connect these cells suggests that Ca^{2+} may regulate cell cycle events. However, further investigation is required to understand the relationship between Ca^{2+} waves in the RPE and NR and mitosis in the NR.

Despite these findings, the exact mechanism by which abnormal chiasmatic pathways are formed remains largely unknown. Neuroimaging techniques such as diffusion tensor imaging can be used to study the structural organization of neural tracts in order to shed more light on the abnormal development of the visual pathway in albinism. We used diffusion data and tractography approaches to map the connections between LGN and V1 in human patients. Studying the developmental link between different structures in the visual pathway will improve the understanding of the etiology and the diagnosis of this condition.

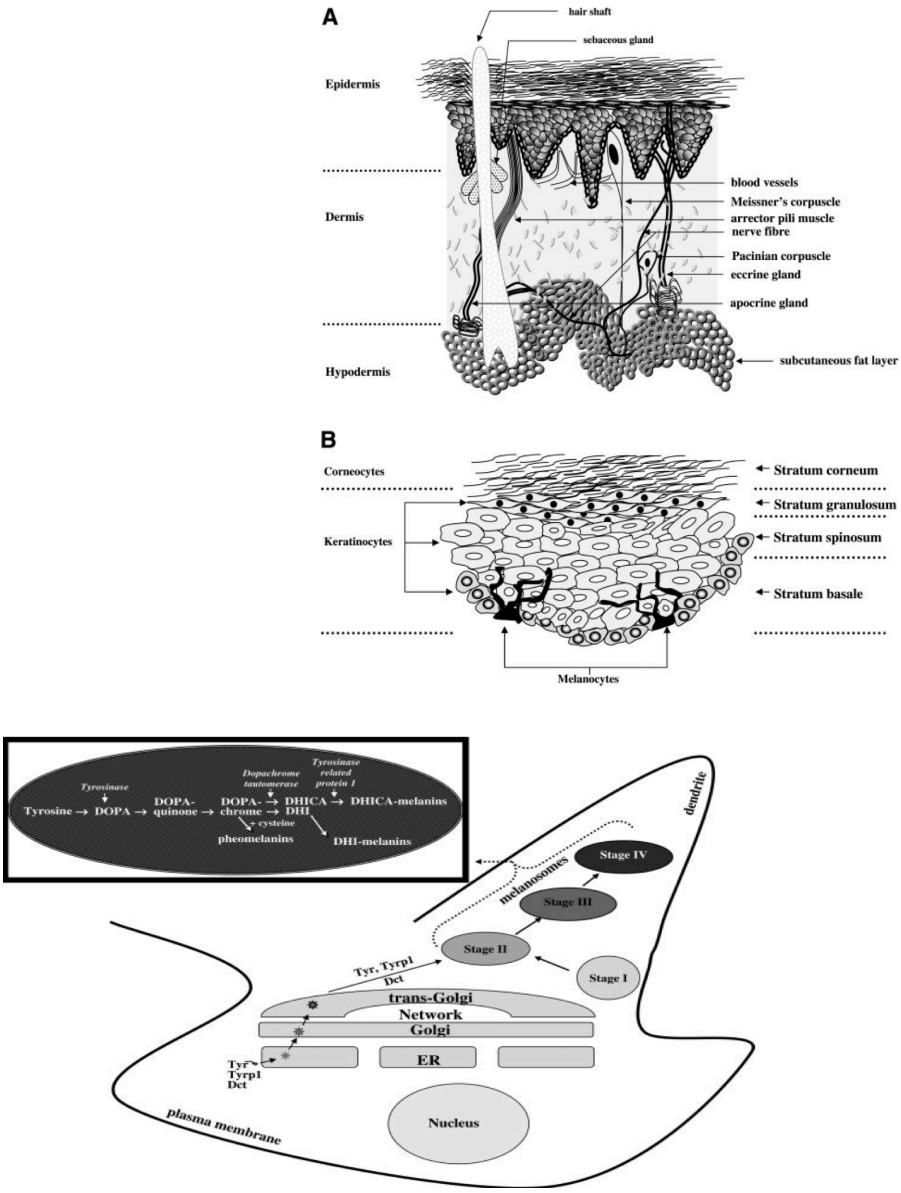

Figure 11: Skin structure. A) The different layers and components of the skin. B) A zoomed-in image of the epidermis, depicting melanocytes and keratinocytes. C) Schematic of a melanocyte, demonstrating melanosome synthesis and migration to the periphery of the cell within dendrites. The melanogenic pathway and key enzymes are displayed in the box (Costin and Hearing 2007).

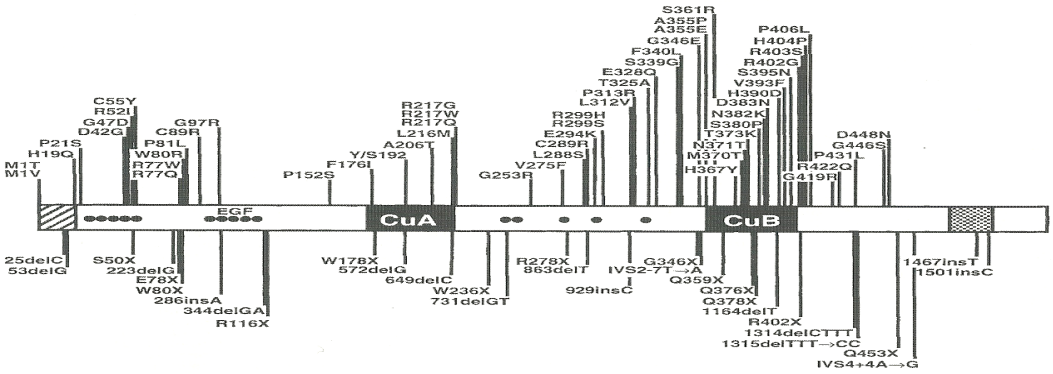

Figure 12: Tyrosinase gene mutations. Locations of missense (top), nonsense, frameshift, and splice-site (bottom) mutations of the tyrosinase gene associated with OCA1. CuA and CuB are the copper-binding sites, located within the coding region. The black circles represent the location of cysteine residues (Oetting and King 1999).

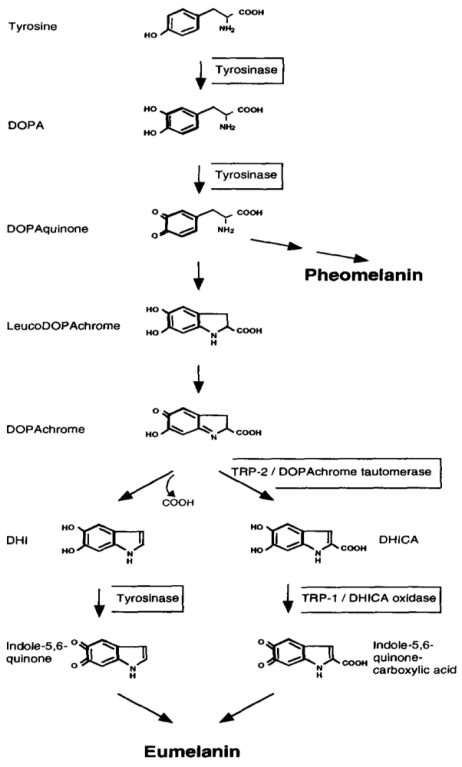

Figure 13: The melanogenic pathway from tyrosine to pheomelanin and eumelanin (Marmol and Beermann 1996).

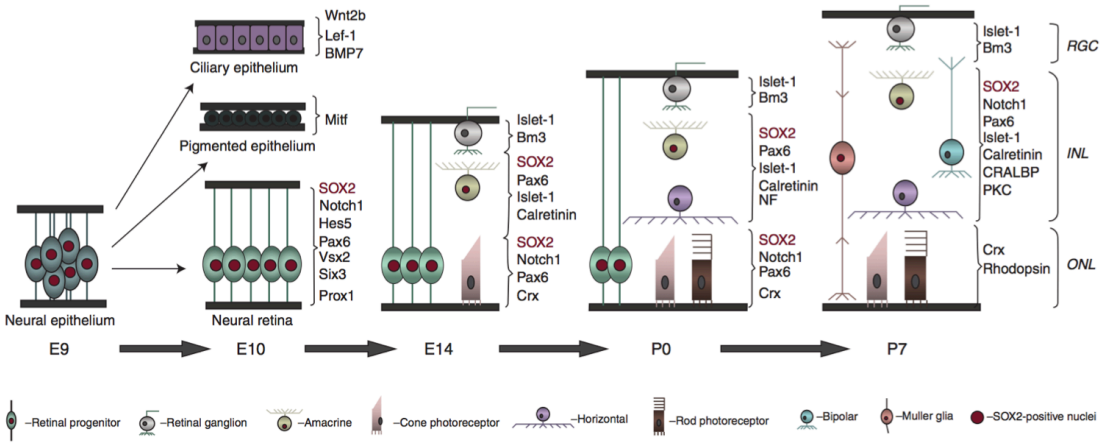

Figure 14: Retinogenesis in the mouse. RGCs, cone photoreceptors, as well as amacrine and horizontal interneurons are generated during an early, embryonic wave, which peaks at E14.5. The late born rod photoreceptors, bipolar cells and Müller glial cells are detected during a second wave, which peaks at P4 (Heavner and Pevny 2012).

Chapter 2: Methods

The visual system has been the main focus of research on clinical conditions in which vision is impaired, as well as the general study of brain development and plasticity. Considerable advances have been made in the field of neuroscience since the 1970s with the introduction of magnetic resonance imaging (MRI), which provides high-resolution images of internal body structures. Recently, research on vision has given more attention to a particular structure in the central visual pathway, the LGN. In albino mammals, hypopigmentation of the RPE results in a reduced number of ipsilateral projections to the LGN. This in turn causes disorganization of the LGN structure as well as its projections to the visual cortex (Creel et al. 1990). While most existing literature on albinism focuses on the retina and chiasm, we studied downstream components of the visual pathway in this population. This chapter describes the basis of MRI, the method implemented here to study LGN to V1 connectivity in albinism.

2.1 The History of MRI: from NMR to Spatial Images

The beginnings of MRI can be traced to the 1920s when basic physics showed that atomic nuclei have magnetic properties. In 1946, Nobel Prize winners Felix Bloch and Edward Purcell elaborated on this idea by introducing the phenomenon of nuclear induction. This phenomenon is now known as nuclear magnetic resonance (NMR). Purcell and his colleagues demonstrated magnetic resonance in bulk matter. They placed paraffin wax in the center of a magnetic field, predicting that at a particular oscillation frequency, the wax would absorb energy from the magnetic field. This magnetic resonance depends on the strength of the magnetic field and can change the electrical conductance of the wax. Conductance, measured by a simple circuit, can only be detected once the atomic nuclei in the sample, in this case the wax, aligned with the external magnetic field. This concept is termed relaxation time. Purcell's team found a resonance effect when increasing the current of the magnet to near maximum. At the same time,

Bloch and his colleagues measured resonance effects in a sample of water placed in a brass box. They used a transmitter coil to send electromagnetic energy into the sample, and a detector coil to measure resonance in the water. Similar to Purcell's group, they also detected magnetic resonance effects. Modern MR scanners share the basic design of Bloch's apparatus: a strong static magnetic field, a transmitter coil and a detector coil (Huettel et al. 2009).

Nuclei contained in body tissues absorb and re-emit electromagnetic radiation when placed in a non-uniform magnetic field. Changes in energy state lead to perturbation in alignment of spins with the external field. The time it takes the protons to re-align is called relaxation time, and during this relaxation a signal is generated. It is measured by two time constants, T1 and T2, which describe the exponential return to equilibrium of spins in directions parallel or perpendicular, respectively, to the applied magnetic field. As they lose energy, spins in the high-energy (antiparallel) state return to their low energy (parallel) state. This is called longitudinal or spin-lattice relaxations (T1), as protons lose energy to their surroundings. Following excitation, the net magnetization is tipped into the transverse plane and all the spins in the sample begin their precession at the same starting point. This coherence between the spins is gradually lost and they fall out of phase. This is called transverse relaxation (spin-spin/ T2) (Huettel et al. 2009).

Water molecules display differences in diffusion and orientation depending on whether or not they are within biological tissue. Such differences can be identified using NMR. Differences in NMR signals between cell water and distilled water have been previously reported, with reduced relaxation times recorded for cell water compared to distilled water. Such differences were attributed to the highly ordered water molecules found intracellularly (endosolvent), which existed as polarized layers adsorbed onto cell proteins (Cope 1969). Hazelwood and co-workers (1969) have shown that rat skeletal muscle growth is accompanied by changes in ionic composition and water structure, suggesting a link between dedifferentiation and alterations in endosolvent structure.

Since dedifferentiation is associated with neoplasia, Raymond Damadian hypothesized that differences in endosolvent structure can be detected between cancerous and healthy cells, making NMR a powerful diagnostic tool. He studied 6 tissues (muscle, kidney, stomach, intestine, brain and liver) from healthy and ill Sprague-Dawley rats, infected with Walker sarcoma and Novikoff hepatoma. NMR measurements were obtained 5 minutes following death. Mean T1 and T2 values for hepatoma (826 ms, 118 ms, respectively) were increased significantly compared to normal liver (293 ms, 50 ms), confirming a decrease in the ordered configuration of intracellular water in malignant tissue. The results demonstrate prolonged T1 and T2 relaxation times for tumours relative to healthy tissue, associating this increase with perturbation to endosolvent in cancer (Damadian 1971). These findings support the hypothesis and further strengthen Hazelwood's work. This study confirms that cancerous tissue exhibits altered water structure in which order is reduced compared to normal tissue, providing, for the first time, a medical application for NMR.

Damadian's work led to advances that resulted in the development of MRI. This technique is more advanced than NMR in its ability to generate images of the signals detected. It provides good contrast between different soft tissues. The resulting images are more detailed than could be generated by x-rays and their acquisition does not require x-ray exposure. Radiation from x-rays is ionizing and therefore harmful to biological tissue. High doses may increase the chance of developing cancer. The term MRI was introduced instead of NMR to eliminate the negative connotation of the word "nuclear", as the technique does not use ionizing radiation. MRI is currently a major tool in the surgical management of tumours. When a tumour is suspected, the initial management involves obtaining MRI imaging to narrow the differential diagnosis.

2.2 The Physics of MRI

Unlike the dissection, tracer injection and lesion production techniques, MRI can noninvasively depict the anatomy and function of soft tissues such as brain structures, and hence it can be used on humans and other animals in vivo. Body tissues contain

water, which constitutes 57–79% of body weight. The basis for the MR signal is in hydrogen atoms (i.e. protons) of the abundant water molecules. Protons have a magnetic moment and spin around their magnetic pole, acting as a micro magnet. The net magnetic field in the body is zero, as all the randomly spinning protons cancel each other. However, upon exposure to an external magnetic field, the proton spins are lined up along the axis of the field (B_0). A radio frequency (RF) pulse (an electromagnetic wave) is then turned on, introducing a varying magnetic field, which flips the spins of the protons. Once the RF pulse is turned off, the protons will realign with the external field and give up excess energy. The time it takes the protons to re-align is called relaxation time, and during this relaxation a signal is generated and detected by receiver coils (Hashemi et al. 2010). The resonant frequency of a spin within a magnetic field of a given strength is called Larmor frequency, given by the angular velocity equation $\omega=\gamma B_0$. The frequency of the electromagnetic pulse is the product of the gyromagnetic ratio (constant for a given atomic nucleus, 42.57 MHz/ T for proton) with the strength of the magnetic field. Magnetic fields used for human research range between 1.5–7 T. 1 T is equivalent to about 20,000 times the magnetic field of the earth.

To convert nuclear magnetic resonance to MR imaging, spatial information must be extracted from the MR signal. To produce 3D images, the MR signal must be restricted to one two-dimensional slice at a time in a process termed slice selection. In this step, an additional gradient is introduced as the electromagnetic pulse is applied to excite spins within a slice. The precession frequencies of nuclei within the slice and the RF pulse have to match. Any other spins in the sample will not be excited since their frequencies are different from that of the RF applied.

Phase encoding and frequency encoding are two related processes that participate in the readout (image acquisition) of an MR signal. The main difference between these two processes is that phase encoding is completed before the data acquisition period, while frequency encoding is applied during this period. If excitation occurs but no additional spatial gradients are applied, all protons will be precessing at the same rate. The resulting MR signal would provide a representation of the total contributions of all

protons within the selected slice, but fail to provide information about the location of the protons. Introducing a non-uniform field will alter the main magnetic field and change the precession frequencies over space. The resulting MR signal would now have various frequency components based on relative location, allowing the construction of a proton density map. This map is a one-dimensional image. Phase encoding is the step required to convert a one-dimensional image into a complex 2D or 3D image. In this step, an additional gradient (y gradient) is applied to a slice in the z direction before the frequency gradient (x gradient) and prior to MR signal acquisition, setting up the phase of the spins. This way, spins precess at different rates based on their position in the slice before the second gradient is introduced. Applying a second gradient allows resolving the 2D spatial information, which leads to different recorded MR signals.

The difference in signals between different types of tissues in the brain produces contrast in the image that is depicted as intensity differences. This difference is based on the water composition of the tissues. Hence, different tissues have different T1 (longitudinal relaxation time) and T2 (transverse relaxation time) parameters, or time constants. In T1-weighted scans, the more protons, the darker the tissue appears in the image. Hence, fluid appears black (e.g. cerebrospinal fluid, CSF), gray matter (GM) appears as dark gray, and white matter (WM) is bright. In T2-weighted images, fat appears darker and water lighter. In proton density (PD) images, contrast is based on proton density in a voxel. Hence, gray matter structures appear as areas of high signal intensity relative to the surrounding white matter (Figure 15).

MRI can be used for diagnosing strokes and tumours in their early stages. This imaging technique is considered to be safe, as it does not use ionizing radiation. The MRI system is, however, very expensive, therefore the exams are also very costly. Another inconvenience is the long scanning time during which subjects need to hold still. Even the slightest movement can distort the images. Moreover, the MRI technique cannot be used on people with pacemakers or any metallic implants, as well as people who suffer from severe obesity or claustrophobia, who would simply not fit into or make it through the MRI.

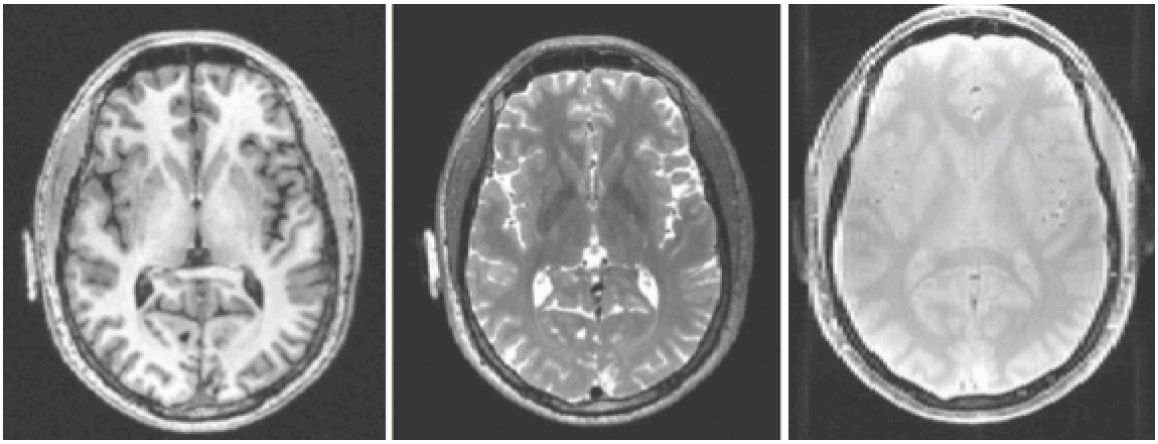

Figure 15: MR signal contrast. T1 imaging requires a short echo time (TE) and an intermediate repetition time (TR) and results in an image with brightest voxels in WM, intermediate in GM and darkest in CSF (left). T2 imaging requires an intermediate TE and a long TR, resulting in an image with brightest voxels in CSF and darkest in WM (middle). PD imaging requires a very short TE and a very long TR, resulting in an image with brightest voxels in CSF, intermediate in GM and darkest in WM (right).

2.3 Advances in LGN Delineation

The 19th century introduced dissection techniques for studying the anatomy of brain tissues. Such methods involve the removal of structures at autopsy for histological preparations. Balado and Franke carried out the first study that examined human LGN using quantitative histology in 1937. They counted 568,845 cells in the LGN. In 1967, Kupfer and colleagues reported cell counts in the optic nerve, optic tracts and LGN removed at autopsy from a patient with unilateral enucleation. Upon removal, tissues were placed in 10% neutral formalin to preserve the tissues from decay. LGN were processed in celloidin, a concentrated preparation of pyroxylin used for embedding specimen for microscopic observations. The 'slice technique' was employed in the study and LGN sections were stained with cresyl violet, an ethanol based solution that colors cell bodies brilliant violet, while causing myelin and other components of the cell to lose their color. Stained sections were then projected onto tracing paper on which the six LGN laminae were outlined. Cell density within each lamina was calculated by counting the number of cells, defined by their distinct nuclei, within a known area measured by planimetry. Since the left eye had been enucleated, cell counts were done in laminae

receiving input from the right eye. The reported total number in the six normal laminae (1,4,6 from left LGN and 2,3,5 from right LGN) was 1,043,000 ± 53,400. Moreover, LGN cell counts agreed with those of optic nerve fibres, and a 1:1 ratio of RGCs to postsynaptic LGN cells was therefore concluded. Also, the ratio of crossed to uncrossed nerve fibres in the optic chiasm was found to be about 53:47, satisfactorily comparable with the ratio of cells in crossed to uncrossed LGN laminae (58:42) (Kupfer et al. 1967).

However, LGN determination in vivo is challenging due to its relatively small size and location deep in the center of the brain. WM tracts including the optic tract, optic radiation and posterior limb of the internal capsule surround the LGN. Due to myelinated fibres within the LGN, signal intensity differences between the LGN and the WM surround are small. Therefore, large contrast-to-noise ratios of LGN compared to surrounding WM are required for LGN delineation.

Fujita and colleagues (2001) determined the anatomical boundaries of the LGN on proton density (PD)-weighted images acquired with a 1.5T scanner using a double-echo turbo spin-echo sequence. In these scans, the LGN appears as an area of high signal intensity relative to the surrounding WM tracts, facilitating its detection. It is visible anterolateral and ventral to the pulvinar, medial to the optic radiation, and supero-medial to the hippocampus. However, the LGN is not consistently detectable on T1 and T2-weighted images, even with high spatial resolution. On these images, the border between the LGN and WM surrounding is indistinct due to small contrast-to-noise ratios between this nucleus and adjacent structures (Figure 16) (Fujita et al. 2001)

In addition to PD-weighted imaging which enhances gray to white contrast, Devlin and others evaluated a second anatomical method that uses diffusion data and tractography to delineate the LGN. Specifically, this approach allows parcellation of GM regions based on their distinct connectivity profiles (Devlin et al. 2006). Both approaches were consistent with published atlases.

The LGN is the only location in the brain where the magnocellular and parvocellular streams are spatially isolated (Figure 17), and is therefore of interest in testing the basis of the magnocelluar theory of dyslexia. In a novel in vivo study on

morphological abnormalities in the LGN of individuals with dyslexia, 40 proton density weighted images were collected with a 3T scanner. These images were then registered to correct for displacement between acquisitions, and averaged to create a mean image with high signal to noise ratio (SNR) (Giraldo-Chica et al. 2015). LGN volume was reduced by about 18% in the left hemisphere of dyslexics compared to controls, while no significant differences were observed in the right hemisphere. Since the left hemisphere receives a larger magnocellular input (Stein 1994), the hemisphere asymmetry is in line with the magnocellular hypothesis.

An alternative method for LGN volume determination uses functional MRI (fMRI). The imaging is based on blood oxygenation level dependent (BOLD) contrast, which is used to map the activated areas in the brain. Active neurons use oxygen bound to haemoglobin to meet their increased metabolic requirements. Since the magnetic properties of deoxygenated haemoglobin alter the spins of nearby diffusing hydrogen nuclei, its presence reduces their signal intensity. Hence, changes in levels of deoxygenated haemoglobin are used markers of brain function. Technical challenges include activation from adjacent structures such as the pulvinar, which introduce bias to the volume measurements (Li et al. 2012). The volume estimates obtained by Li and collaborators were consistent with post-mortem results. Fujita and colleagues (2001) reported that the region activated in fMRI could be superimposed onto the anatomical protein density-weighted image obtained for the LGN (Figure 16).

Defining the LGN based on functional activation (Schneider et al. 2004) may result in an overestimation of the anatomical boundaries due to surrounding voxels containing nearby blood vessels and other subcortical structures. In the population receptive field (pRF) model, RF properties are derived from a BOLD signal of a population of neurons within a voxel. This approach is used to measure retinotopic maps in subcortical areas such as the LGN. DeSimone and others overlaid pRF estimates in the LGN on PD images to confirm functional activation (DeSimone et al. 2015). They were the first to use anatomically guided tracing of the LGN in retinotopic mapping.

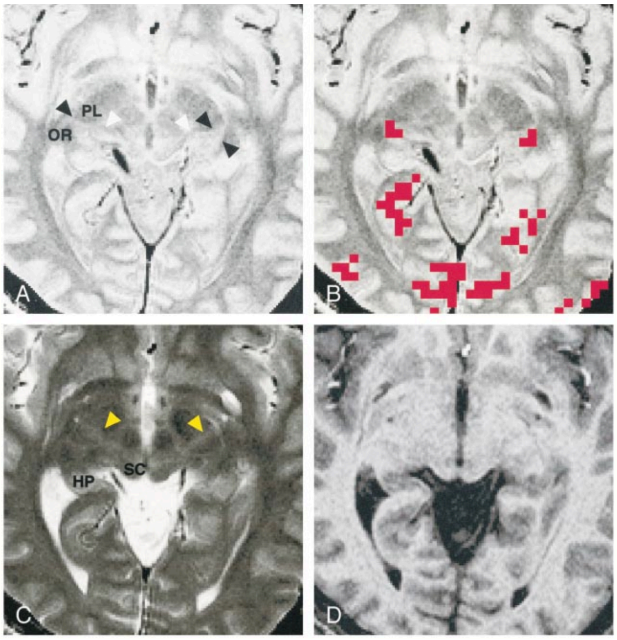

Figure 16: LGN detection on different MR contrasts. A) PD image shows LGN (black arrowheads) bordered by OR. B) Activation at the identified location of LGN superimposed on the PD image. C) T2 and D) T1 images show no clear LGN-WM border (Fujita et al. 2001).

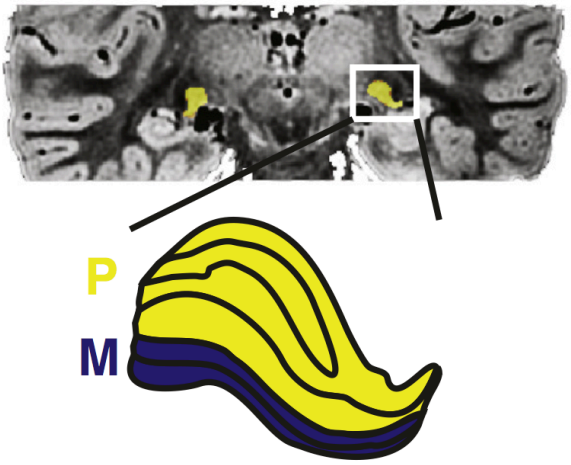

Figure 17: An outline of the LGN. In the box, LGN mask delineated on a coronal slice of a PD image (Giraldo-Chica et al. 2015). Zoomed-in outline of a human LGN from a stained section (Andrews 1997) with distinct parvo- and magnocellular layers (bottom).

2.4 Advances in White Matter Reconstruction

2.4.1 In Vitro Techniques

A common technique for studying fibre pathways in non-human primates involves injections of horseradish peroxide or Lucifer yellow, which spread within the neurons and allow anatomical depiction of the target cells. In some cases, retinal lesions can be introduced in order to induce cell permeability to dyes, which allows the precise tracing of a selected axonal pathway (Picaud et al. 1990). However, these techniques are invasive and cannot be applied to healthy humans in vivo (Hofer & Frahm 2008).

Examining patterns of anatomical connectivity in humans has been limited. Dissection, tracer injection and lesion induction are invasive techniques that can only be used post mortem, and usually involve a very small number of patients. Previous studies using carbocyanine dye DiI injections demonstrated neuronal connectivity between V1 and V2 (secondary visual cortex) (Burkhalter & Bernardo 1989), as well as within the hippocampal complex in aldehyde-fixed post-mortem human brains (Mufson et al. 1990). Labeling fibers in this way is restricted to distances of only tens of millimeters from the point of injection (Mufson 1990).

In the early 19th century, Louis-Pierre Gratiolet identified the fibres that run from the LGN to the visual cortex, now known as the optic radiation (OR), using dissection. A new dissection method was developed by Joseph Klingler in 1934, as the interest in mapping WM tracts for neurosurgery increased. This method has been implemented in studies on the extent of the OR and its relationship to structures such as the temporal horn in order to facilitate surgery in the temporal lobe. Klingler's method is based on freezing of brain tissue, which causes a 10% increase in water volume upon ice formation, allowing loosening of the tissue. The resulting spread of fibres allows easier delineation of fine fibre bundles (Figure 18) (Ebeling & Reulen 1988).

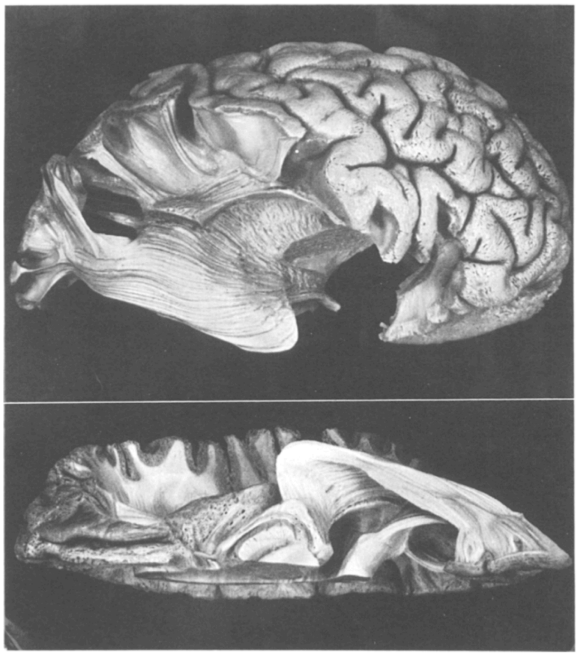

Figure 18: OR delineation based on Klingler's method. Lateral (top) and ventral (bottom) views of the OR of the right and left hemispheres, respectively (Ebeling and Reulen 1988).

2.4.2 Diffusion Tensor Imaging and Tractography

Diffusion tensor imaging, DTI, is an MRI modality developed in early-mid 1990s to identify fibre tract direction and organization. It is a non-invasive method that allows mapping of large white matter (WM) pathways in the living brain. DTI is sensitive to the diffusion of water molecules in biological tissue (Wedeen et al. 2008). Due to the organization of white matter in the brain, the diffusion of water molecules across, or perpendicular to the orientation of the fibre bundles is more challenging, given barriers such as membranes and myelin. Rather, its preferential diffusion is in the direction of less barriers, that is, along the long axis of the fibre (Smith et al. 2006).

DTI uses a collection of images, each sensitized to diffusion in a different direction (minimum of 6 directions required), to quantify the relative diffusivity of water in a voxel into directional components. To accurately measure fibre orientation, the concept of diffusion tensor was introduced. In this model, measurements along different axes are fitted to a 3D ellipsoid. In this ellipsoid, the principle eigenvector tells you about

the principle direction of diffusion in a single voxel. The other two vectors tell you about the girth of the ellipsoid, or in other words, about how homogenous diffusion is in a region (Figure 19). Girth is expressed as fractional anisotropy, FA. FA is a scalar quantity that describes the preference of molecules to diffuse in an anisotropic manner. FA values range from 0–1, from low to high anisotropy (CSF < GM < WM)(Smith et al. 2006). In diffusion-weighted images (DWI), darker regions represent high water diffusivity. In an anisotropic medium, diffusion causes water molecules to move away from the centre and towards the surface of an ellipsoid, which is described by the direction of its three axes (x,y,z), called eigenvectors, and by their lengths (V), termed eigenvalues (λ). The sum of the three eigenvalues divided by three yields the mean diffusivity (MD) (Vandermosten et al. 2012).

Different algorithms exist to reconstruct 3D pathways using the directional information gained from diffusion data, including streamline (deterministic) and probabilistic fibre- tracking. Deterministic tractography uses a line propagation method, connecting neighbouring voxels in a defined seed region. This algorithm progresses only if the FA in a voxel exceeds a specific threshold, limiting its effectiveness in accurately defining pathways near gray matter. Due to such locally optimal decision-making, regional aberrations caused by artifacts and noise, as well as by unresolved features such as crossing fibres are not considered by the deterministic approach. Also, since deterministic algorithms do not account for uncertainty in the data, a pathway will appear to either exist or not, increasing the risk of false negatives. This becomes an issue in presurgical preparations, as lesions often distort the diffusion signal of nearby tracts (Johansen-Berg and Behrens 2013).

Probabilistic tractography, on the other hand, yields a connectivity map describing the probability of a voxel to be part of a tract between two regions of interest (ROIs) and thus allows tracing directly from deep GM like the LGN and into gray matter such as V1 (Newcombe et al. 2013) (Figure 20). Apart from its ability to track in areas of low probability, this approach is also resistant to noise. This is because erroneous routes tend to disperse, which classifies them as areas of low probability, while ‘true’ paths group

together, yielding a higher probability of connection (Behrens et al. 2003). Using this MRI application, key WM structures like the OR can be delineated, as shown in previous studies (Behrens et al. 2003; Bassi et al. 2008; Hofer et al. 2010). Limitations to this approach include the inability to determine tract polarity to distinguish thalamocortical from corticothalamic connections. Moreover, pathways that display sharp inflections or cross other tracts are not always detected (Behrens et al. 2003).

Since the introduction of DTI and fibre tracking (FT), much attention has been paid to the study of the OR. Particular focus has been on the portion that passes through the anterior temporal lobe prior to looping back to the cortex, called Meyer's loop. It constitutes a bundle of fibres that carry information about the contralateral upper visual field, which makes it a critical site during surgery (Sherbondy et al. 2008). Due to its complexity, visualizing this portion of the OR becomes challenging and requires the use of higher resolution imaging and careful choice of analysis approaches (Behrens 2003). Despite their simplicity and speed, deterministic algorithms have limitations that may be critical in clinical application. Such algorithms yield first order approximation of the OR but do not match the gold standard determined by Ebeling and Reulen (1988) (Klingler's method). Deterministic based studies have reported differences in the mean anterior position of Meyer's loop of more than 1 cm posterior to estimations from dissection (Yamamoto et al. 2005; Nilsson et al. 2007). Studies using probabilistic algorithms such as ConTrack reported estimates of the course of the healthy OR (Sherbondy et al. 2009) that match those detected with the gold standard with a spatial precision of about1mm (Figure 21) (1988).

An important drawback of DTI is its inability to resolve multiple fibre orientations within a voxel. The diffusion tensor model assumes Gaussian diffusion according to which only a single fiber bundle orientation can exist within a voxel. However, many regions are nearly isotropic due to non-Gaussian diffusion resulting from fiber crossing and branching. Specifically, about one third of white matter voxels contain multiple fiber bundle orientations. Furthermore, the resolution of diffusion-weighted imaging (DWI) usually ranges between 3–15 mm^3, while fiber bundle diameters are on

the order of 1 mm, with single axons on the order of 1–30 µm. Therefore, WM pathways resolved with DT-based tractography are prone to misrepresentation arising from false anisotropic diffusion profiles or premature stop in region of low anisotropy. To overcome this limitation, high angular resolution diffusion imaging (HARDi) techniques, including q-ball and diffusion spectrum imaging (DSI) have been developed (Descoteaux et al. 2009).

Despite its limitations, diffusion imaging remains the only technique available for non-invasive identification of structural connectivity in the human brain. Furthermore, it has become validated by post-mortem tract tracing techniques, revealing a high degree of overlap between the connectivity determined with each of the techniques (Vandermosten et al.2012).

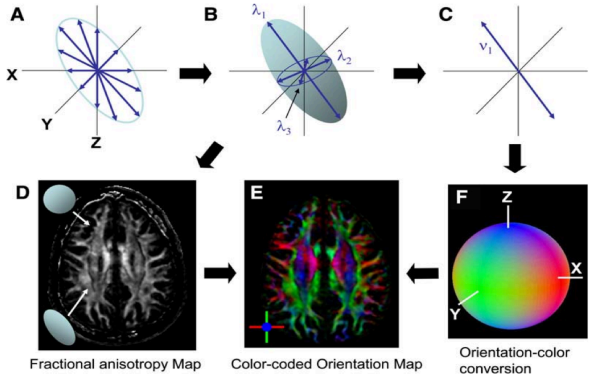

Figure 19: The diffusion tensor model. Diffusion measurments along multiple axes (A) generate an estimated diffusion ellipsoid (B) from which the orientation of the longest axis can be found(C). An anisotropic map is created from the shape of the ellipsoid (D), with dark regions are isotropic (spherical) and bright regions are anisotropic (elongated). The local fibre orientation information derived from (C) can be converted to a color-coded orientation map (E) by combining the intensity of the anisotropy map (D) and color (F) (Mori and Zhang 2006).

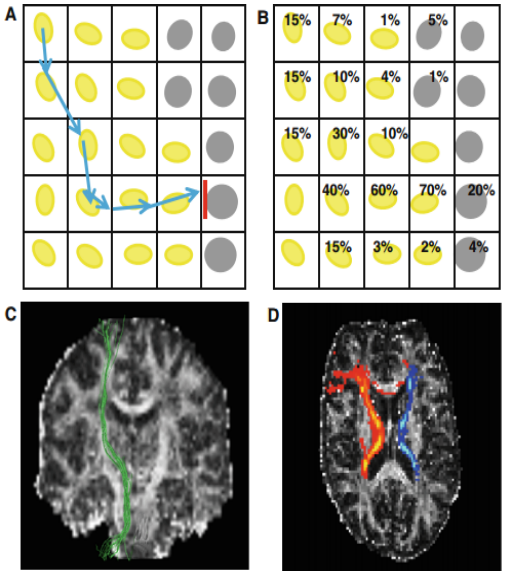

Figure 20: Schematic comparison of streamline (deterministic) and probabilistic tractography. (A) and (B) yellow circles are more anisotropic, gray are more isotropic voxels (Newcombe et al. 2013). Note that tractography does not show the anatomy of an axon or a fibre, but simply the direction of diffusion within a region.

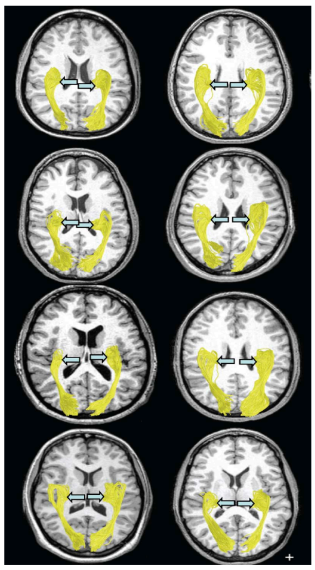

Figure 21: OR tractography in healthy humans. Measurements consistent with Ebelin and Reulen dissection results (Sherbondy et al. 2008).

Chapter 3: Research Protocol: Abnormal Brain Connectivity in the Primary Visual pathway in Human Albinism

3.1 Background

3.1.1 The Lateral Geniculate Nucleus

The thalamus, constituting a complex of GM nuclei, is located at the junction of the brain stem and cerebral hemispheres (Fujita et al. 2001) and carries sensory information to the cerebral cortex. Visual information from the retina is relayed in the LGN to V1(Figure 22). Its precise location depends mainly on the size of neighbouring structures in the thalamus (Chacko 1948). Its volume correlates with the volumes of the optic tract and V1, as shown by post mortem examination (Andrews et al. 1997). This demonstrates interdependent development of components of the visual pathway. Great inter-subject variability in LGN size has been reported in various histological as well as structural and functional imaging studies (Table 1).

In higher primates, the LGN is divided into 6 layers: 4 dorsal, small-celled layers (i.e. parvocellular, P), and 2 ventral, large-celled layers (i.e. magnocellular, M). Inter-laminar regions found between the main layers of the LGN consist of a third type of neurons, known as the koniocellular, K cells (Figure 23). This cyto-architectural organization is based on function. The three classes of neurons composing the LGN represent parallel pathways in the visual system. They are each responsible for processing particular facets of the image obtained on the retina, based on their sensitivity to chromatic, temporal and spatial stimuli (Schwartz 2010).

The M, P and K cells in primates correspond to Y, X and W cells in other mammals, respectively. The M, P and K cells receive their inputs from different types of RGCs (Rodieck et al. 1993). About 90% of RGCs project to the LGN. Projections into the magnocellular layers are primarily of parasol cells, which possess large dendritic trees. The parvocellular layers are mainly fed by midget cells with smaller dendritic trees.

Projections to the koniocellular zones are relatively variable (Kremers et al. 2005) (Figure 24). The parvocellular projection accounts for approximately 80% of the retinogeniculate pathway, while the magnocellular projection represents about 10% of the pathway (Meissirel et al. 1997). Magnocellular neurons are innervated by faster conducting retinal axons compared to the parvocellular neurons, and exhibit faster and more transient responses, higher temporal resolution, higher contrast sensitivity, and lower spatial resolution than parvocellular neurons. Color is rather processed by parvocellular and koniocellular neurons (Jones 2007).

In the development of the LGN, retinal afferents segregation occurs first, followed by interlaminar spacing and finally by the formation of distinguishable cytological characteristics of individual layers. The laminar pattern seen in the adult LGN takes 3 weeks beginning around the 22nd week of gestation to evolve into its mature form (Hitchcock & Hickey 1980). While all 6 layers of a typical human LGN are separated in the medial portion of the nucleus, layers 5 and 6 do not extend into the lateral horn. Hence, only 4 layers appear at the caudal pole (Kupfer 1965).

While LGN structure is fairly consistent across non-primate mammals such as cats, human LGN shows large inter-subject variability (Hickey & Guillery 1979). In particular, variations correspond to its rostral part, representing the peripheral visual field. However, the laminar pattern in the caudal part, which represents the central visual field, is relatively constant. The fairly constant structure of the LGN observed in other species suggests that a regular laminar organization is associated with proper operation of the visual system. A possible explanation for the variability in humans relative to other species is a reduction in the selective pressure for good peripheral vision as a direct consequence of a civilized lifestyle (Hickey and Guillery 1979).

Table 1: Summary of LGN volumes reported throughout the years as measured using different techniques (modified from Li et al. 2012).

Type of study	Authors	Year	Subjects	Morphometric measurements
Histological	Putnam	1926	Healthy subjects	Ranging from 91.9 to 157 mm^3
	Zvorykin	1980	Healthy subjects	Ranging from 66 to 152 mm^3
	Selemon and Begovic	2007	Healthy subjects	Average volume: 79.67 mm^3
	Dorph-Peterson et al	2005	Healthy subjects (only left LGN)	Average volume: 104 mm^3
	Andrews et al	1997	Healthy subjects	Mean right: 121 mm^3. Mean left: 115 mm^3.
fMRI	Chen et al	1999	Healthy subjects	Activation area: 4.6 x 4.6 mm^2
	Schneider et al	2004	Healthy subjects	Mean activated volume: 440 ± 25 mm3
	Kastner et al	2004	Healthy subjects	Left/right: 234 ± 29 mm^3/244 ± 28 mm^3
	Korsholm et al	2007	Patients with isolated optic neuritis	Average of bilateral LGN: 267 ± 27 mm^3
	Hess et al	2009	Patients with amblyopia	Left/right: 409 ± 306 mm^3/439 ± 310 mm^3
Proton density MRI	Gupta et al	2009	8 Healthy subjects	Height: left/right 4.83 ± 0.95 mm/4.74 ± 0.54 mm
	Li et al	2012	Healthy subjects	Mean right: 86 mm^3. Mean left: 77 mm^3.
	McKetton et al.	2014	Healthy vs. Albinism	Healthy: LLGN 157.9 ± 9.8 mm3, RLGN 165.2 ± 9.6 mm3 ; Albinism: LLGN 98.2 ± 6mm3, RLGN 105.6 ± 8.7mm3
	DeSimone et al.	2015	Healthy subjects	LLGN: 214± 1, RLGN:229± 30

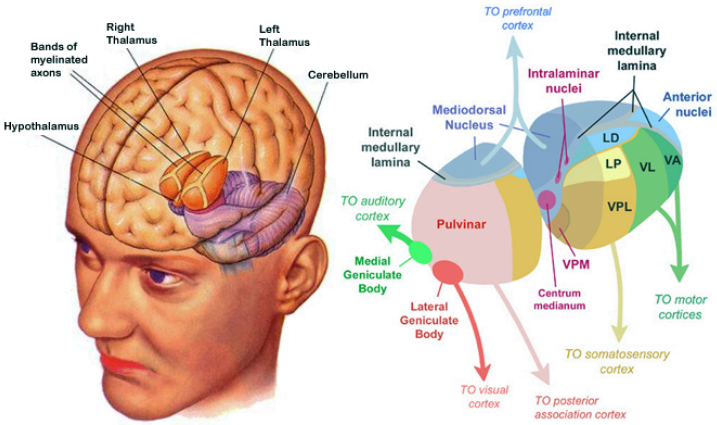

Figure 22: The position of the thalamus in the brain, depicted in orange on the left image (SEER Training Modules/ U. S. National Institutes of Health, National Cancer Institute). The subdivisions of the thalamus are shown on the right. The LGN is adjacent to the pulvinar and is placed in close proximity to the medial geniculate body (MGB/MGN) (MedLibes (Online medical library)).

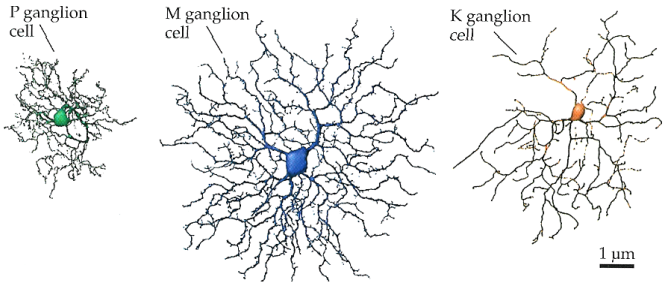

Figure 23: Tracings of ganglia as seen in flat mounts of the retina (Purves et al. 2008).

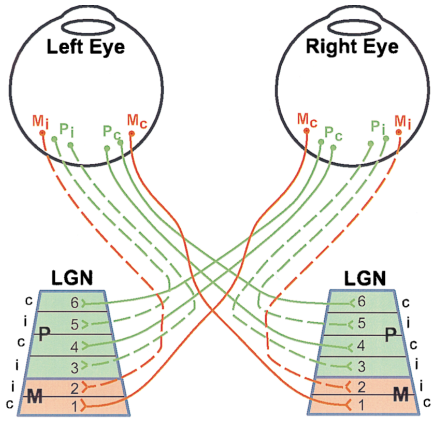

Figure 24: Layers of the LGN. The ventrally situated magnocellular layers receive input (1-contra, 2- ipsi) from retinal ganglion parasol cells. The more dorsal parvocellular layers receive input (3,5 –ipsi, 4,6-contra) from retinal ganglion midget cells (Meissirel et al. 1997).

3.1.2 The Relationship between the Number of RGCs and LGN Neurons

Work dated from 1876 by Krause reported an estimate of 10^6 nerve fibres in men. This finding is based a calculation of the average fibre size and the overall optic nerve diameter. A later study suggested that the number of fibres in the optic nerve range from 564,775 to 1,140,030 (Bruesch and Arey 1942). The estimated ratio of crossed to uncrossed nerve fibres in the optic tract was 2:1 (Ramon and Cajal 1899), and was later revised to 3:2 by Santha (1933).

Balado and Franke were the first to report an estimate of the number of cells in the lateral geniculate nucleus, which they found to be 568,845 (1937). Chacko reported a count of 1,210,000 cells (1948). She also found the ratio of LGN cells of crossed to uncrossed laminae to be 56:43. She suggested a 1:1 ratio of optic nerve fibre to geniculate cell number. Kupfer and colleagues reported a range of 1,060,100 to 1,127,268 optic nerve fibres (Kupfer et al. 1967). They also found a ratio of 53:47 crossed to uncrossed optic nerve fibres in the chiasm, and 58:42 cells of crossed to cells of uncrossed laminae in the LGN. Due to the close agreement between the LGN optic nerve cell count, they concluded that the overall ratio of optic nerve fibres to post-synaptic LGN cells is 1:1.

A more recent study (1996) by Spear and colleagues examined the numbers of both retinal ganglion cells and the LGN cells in the rhesus monkey, and their results were consistent with previous studies, suggesting an average ratio of 1:1 retinal projections to the LGN to number of LGN cells. However, they indicated a two- fold range in ratio in individual animals, varying from 0.78:1 to 1.64:1(Spear et al. 1996).

3.1.3 Comparison of Three Principal Mammalian Models of the LGN

In rodents, the nucleus consists of a fairly homogenous cell population and segregation into separate layers is not overt. The simplest pattern of organization includes two layers innervated by fibres of the contralateral eye, as well as a shorter middle layer innervated by ipsilateral projections, detected under staining of retinal axon terminations (Reese 1988). The small ipsilateral input to the nucleus is related to the position of the eyes, which are laterally directed and share a relatively small degree of overlap (~ 30°) in

the binocular visual field. In more visually developed rodents, such as squirrels, the pattern observed is more extensive, consisting of three longer layers innervated by contralateral retinal projections, and two shorter layers innervated by ipsilateral projections. Regions of alternating retinal inputs constitute the binocular segment of the nucleus, while the region receiving only contralateral inputs represents the monocular segment of the nucleus (Figure 25, top left) (Jones 2007).

The nucleus of carnivores is separated into 3 layers. The dorsal (A) lamina receives inputs from the contralateral retina, while the middle lamina (A1) receives inputs from the ipsilateral retina. Similar to rodents, the ipsilaterally innervated lamina is shorter. The third lamina is closest to the optic tract and is further subdivided into sublaminae, which together are called the C laminae. The most dorsal in this group of layers consist of large cells, whereas laminae C1–C3 consist of small cells. The cat, which serves a great model for studying the mammalian visual system, was the first species in which parallel retino-geniculo-cortical pathways were identified. Axons of X retinal cells project to the geniculate lamina A or A1, depending on the eye of origin. Contralateral retinal Y axons terminate in laminae C and A, while ipsilateral retinal Y axons terminate in lamina A1. Carnivores such as cats have frontally located eyes; hence the overlap of their visual fields is almost complete and the ipsilateral and contralateral retinal projections to the LGN are nearly completely segregated. This suggests that the line of decussation through the area centralis is well defined, usually preventing projections to the wrong side (Jones 2007) (Figure 25, top right).

In prosimians, the LGN forms an elongated lateral bulge on the thalamus, while in simians it acquired the shape of an inverted U (Figure 25, bottom left). In humans, the U appears opened out (Figure 25, bottom right). Unlike most primates, some new world monkeys do not follow the traditional 4-layered pattern of 2 magno- and 2, often further divided, parvocellular laminae. The LGN of a squirrel monkey, for example, exhibits parvocellular sublaminae comparable to laminae 5 and 6, but lacks subdivisions that form laminae 3 and 4 (Horton & Hocking 1996). Human LGN is very large, yet it is smaller than in monkeys relative to the remainder of the thalamus. Parvocellular layers 3 and 5,

and 4 and 6 show a similar degree of peripheral fusion in both humans and monkeys (Jones 2007). An S layer is found in monkeys and humans, and consists of small cells that receive both retinal and collicular inputs. Short wavelength-specific (blue) RGCs have been identified by Wiesel and Hubel (1966). These RGCs project to the cells in the S and interlaminar zones (Wiesel & Hubel 1966).

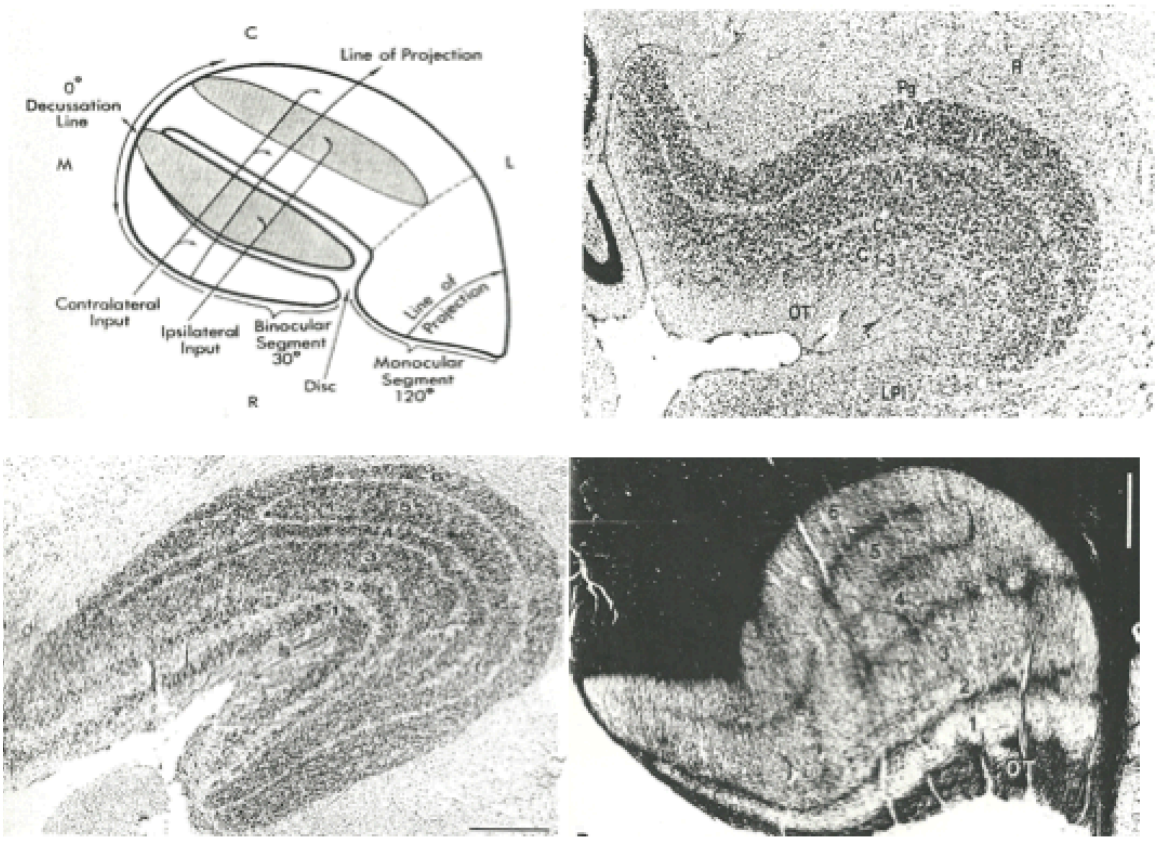

Figure 25: Mammalian LGN structure. Top left: LGN of the squirrel. The layers receive alternating input (ipsi-/contralateral). The part innervated by contralateral input only constitutes the monocular segment (Kaas et al 1972). Top right: Sagittal thionin-stained section through the cat LGN (Jones 2007). Bottom left: Frontal thionin- stained section through the U- shaped dLGN of a rhesus monkey (*Macaca mulatta*) (Jones 2007). Bottom right: frontal section stained with hematoxylin through the LGN of a human. Notice the fusion of layers 3 and 5 and the opened out U shape compared to that of the monkey (Jones 2007).

3.1.4 The Effects of Misrouting on LGN Organization

The characteristic reduction in ipsilateral projections in albinism disrupts the LGN organization and leads to disorganized visual information in the visual cortex. Rebsam

and colleagues traced retinogeniculate axons in tyrosinase negative albino mice, which lack distinct eye specific layers in the LGN (Huberman et al. 2008). They found that although the ipsilateral projection in the albino mice targeted the same LGN zone as in pigmented mice, it was reduced by 48%, occupying just 9.7% of LGN territory compared to almost double the occupancy in pigmented mice. They also detected a population of RGCs from the VT retina, which terminated in a patch adjacent but separated from the principal contralateral termination area in the LGN (Figure 26) (Rebsam et al. 2012). The researchers also showed that the reduction in ipsilaterally destined RGCs is correlated with fewer VT RGCs expressing Zic2 and EphB1, but not with an increase in cells expressing contralateral markers such as Islet2 (2012).

Autoradiographic labeling in the albino green monkey LGN revealed abnormal contralateral innervations of LGN zones normally innervated by ipsilateral afferents (Guillery et al. 1984). The laminar pattern of the LGN was affected, with the boundaries between the magnocellular and parvocellular layers being less defined than in a pigmented monkey. The ipsilateral input was greatly reduced in the posterior and medial portions of the nucleus, which are associated with central vision. The magnocellular layers were more severely affected than the parvocellular ones. They appeared smaller in regions innervated by ipsilateral fibres (Figure 27).

Evoked potential in human albinos have shown abnormal response of ipsilateral cortex to monocular stimulation, implying chiasmatic misrouting in this population. Post-mortem examination of the LGN revealed extensive fusion of the parvocellular layers. Also, the magnocellular portion, which is normally divided into two layers, appeared as a single distinct magnocellular layer throughout most of the six-layered segment (Figure 28) (Guillery et al. 1975). Such fusing of adjacent layers is suggestive of abnormal retinal projections into the nucleus.

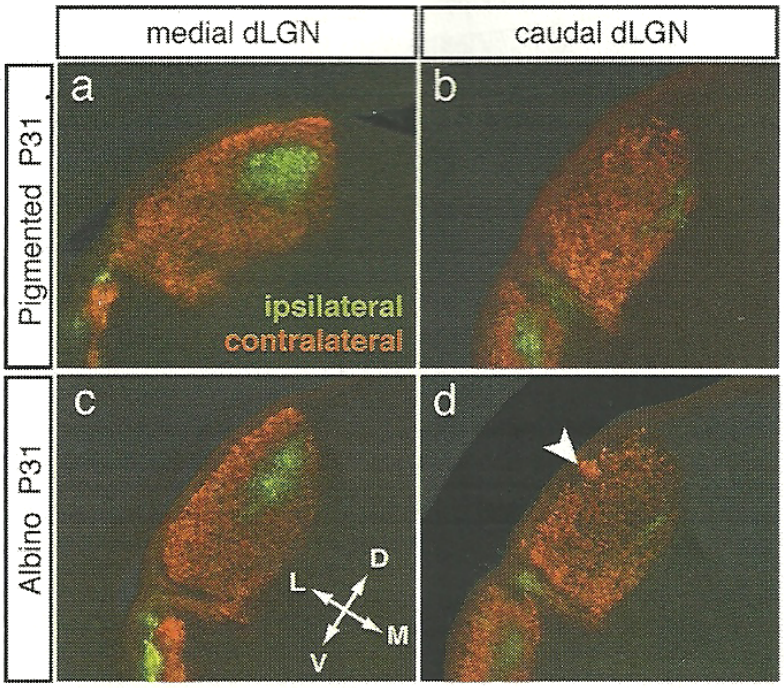

Figure 26: LGN lamination in the albino mouse. The ipsilateral (green) termination zone is reduced in size (c, d versus a, b). Additionally, a cluster of contralateral (red) fibres from VT retina is found in the caudal LGN (d, arrowhead), within the contralateral RGC-recipient zone but separate from the normal contralateral projections (Rebsam et al. 2012).

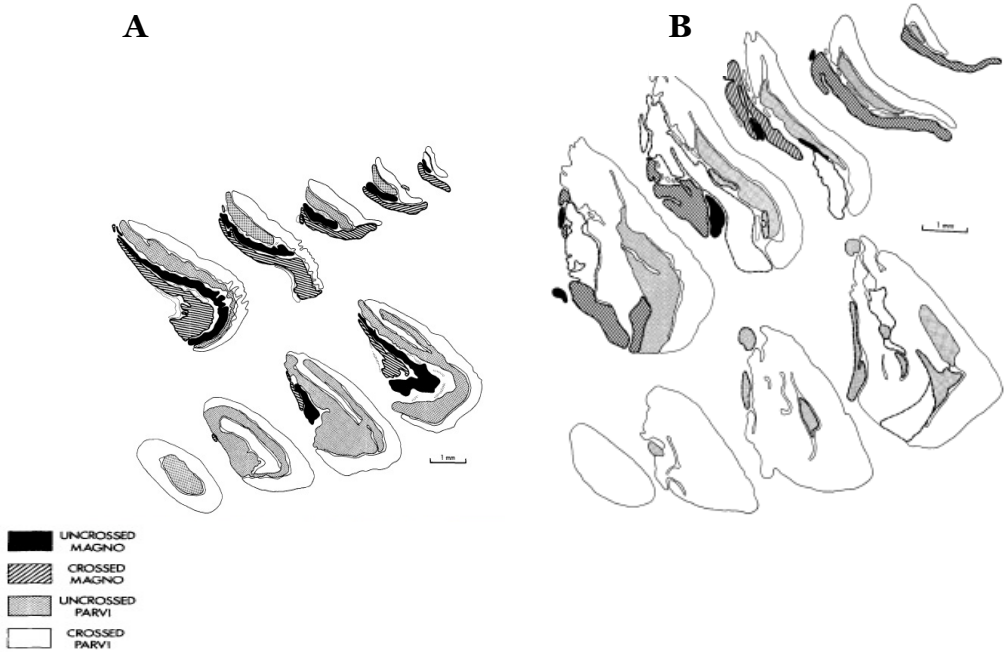

Figure 27: LGN of normal and albino green monkeys. Drawings of parasagittal sections through the LGN of (A) a normal green monkey and (B) an albino green monkey. The magnocellular layers in the albino monkey are significantly reduced compared to the normally pigmented monkey (Guillery et al. 1984).

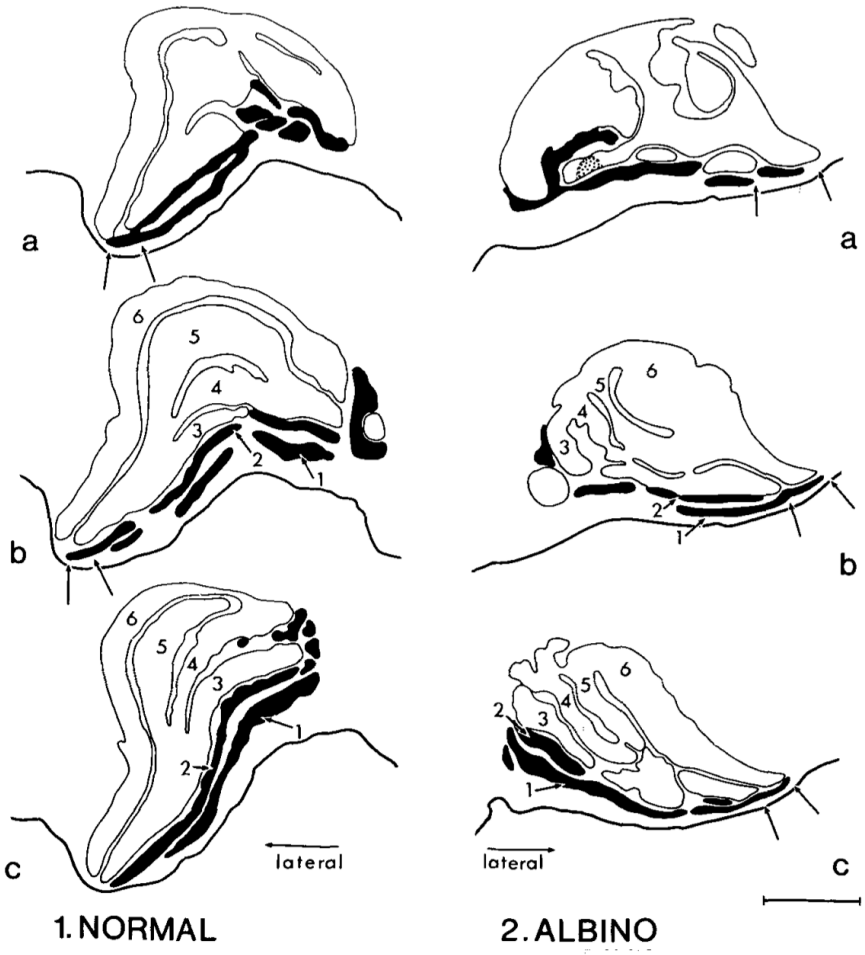

Figure 28: LGN of healthy and albino humans. Abnormal lamination is observed in albinism, with adjacent layers fusing together (Guillery 1975).

3.1.5 Altered Cortical Response in Albinism

Previous studies on Siamese and albino cats have shown that the shift in line of decussation into the temporal retina is greater in tyrosinase negative albino cats, leading to greater misrouting in this strain (Creel et al. 1982). A similar inversely proportional relationship between the level of pigmentation and the shift in line of decussation was seen in albino mice and mink (Balkema & Dräger 1990; Sandron et al. 1974). Retinotopic

mapping and VEP techniques (Hoffmann et al. 2005; Hoffmann et al. 2003) suggested a similar relationship in humans by showing a range of shifts in the line of decussation from 2 to 15° of the visual field.

Von dem Hagen and colleagues used fMRI to visualize the extent of hemispheric response lateralization in healthy humans and albinism patients upon hemifield stimulation of nasal or temporal retina. Stimulation of the nasal retina produced a similar contralateral response in both groups. However, stimulation of the temporal retina resulted in a contralateral response in posterior slices of the occipital lobe in albinos, instead of the normal ipsilateral response as seen across all slices in controls. This finding is in line with the abnormal fibre projections from the temporal retina in albinism. The cortical response was further examined based on the topographic mapping of the retina onto the cortex, according to which central and peripheral visual fields are represented in the posterior and anterior parts of the cortex, respectively. As slice location in albinos became more anterior, lateralization reverted to the ipsilateral hemisphere, providing an estimation of the extent of misrouting (Von Dem Hagen et al. 2007). The abnormal response in the posterior part is consistent with the underdeveloped fovea reported in albinism (Wilson et al. 1988). Slice transition location correlated negatively with the level of pigmentation as determined by visual assessment. These results suggest that pigmentation can predict the shift in line of decussation in humans with albinism.

Voxel-based morphometry (VBM) can be used to compare gray matter volumes in the occipital lobes of albino and non-albino humans (von dem Hagen et al. 2005). Since the size of V1 has been previously linked to the magnitude of the retinal input (Andrews et al. 1997), a reduction in V1 volume in individuals with albinism has been proposed. Von-dem Hagen and co-workers reported a reduction in gray matter volume corresponding to the cortical region that represents the central visual field. This reduction is possibly linked to the underdeveloped central retina observed in albinism.

3.1.5 Retina and Chiasm as candidates for Axonal Misrouting

The retina and optic chiasm express axonal guidance cues such as Eph family

receptors and their ligands (Williams et al. 2003), and are therefore candidate sites for misrouting in albinism (van Genderen et al. 2006). Marcus and colleagues carried out several experiments in mice to investigate the site of gene action associated with the reduced ipsilateral projection observed in albinism. First, they used DiI-labeling to compare the trajectory of crossed and uncrossed axons from albino and pigmented animals, demonstrating similar growth patterns of retinal axons in both groups. The authors therefore concluded that, though smaller in size, the trajectory of the VT component is unaffected by the albino mutation. They then co-cultured retinal explants and dissociated chiasm cells from pigmented animals, revealing greater reductions in outgrowth from VT compared to dorsotemporal (DT) retina (source of crossed axons) (Mason et al. 1996). Previous studies showed that the growth rate of axons in the chiasm is slow relative to the optic nerve and tract, consistent with the chiasm's role as a decision region that prepares axons to respond to divergent cues. Such studies explain the overall pattern of reduced outgrowth observed from both VT and DT retina (Wang et al. 1995). The greater reduction in length of VT compared to DT axons is supported by time-lapse video microscopy of retinal growth, which revealed that uncrossed axons in an intact optic chiasm pause for longer durations than crossed axons. Such retardation in growth may be related to the process of turning into the ipsilateral tract (Godement et al. 1994). A similar difference in length of VT compared to DT was observed when retinal explants from pigmented animals were grown on cells dissociated from albino chiasm. These findings indicate that chiasm cells from both albino and pigmented animals promote differential growth of crossed and uncrossed axons, suggesting that the albino mutation does not affect chiasmatic signalling. Additionally, the researchers grew albino retinal explants with dissociated chiasm cells from pigmented or albino animals. They found a similar pattern of differential growth as observed in pigmented retinal explants grown on chiasm cells from either group. However, albino uncrossed axons were reduced to a much lesser degree compared to pigmented axons, as if they originated from the part of the retina allocated to crossed cells. These findings suggest that the albino mutation alters the number of RGCs that respond to divergence cues, but that the cellular composition of

the optic chiasm is normal in albino animals (Marcus et al. 1996). Taken together, these results suggest a localization of the site of gene action to the retina.

In most studied albino mammals, central RGC density is 25% below normal. No similar deficits are found in non-mammalian animals. Albino birds, for example, demonstrate normal central retina. In the bird retina, cones outnumber rods. Most mammals, however, have rod-dominated retinae. The albino mutation exerts its affect on rods (Donatien & Jeffery 2002),while cone numbers and distribution are normal (Jeffery et al. 1994). Bird outer retina may therefore be relatively unaffected by the albino mutation. Esteve and Jeffery studied RGC densities in pigmented and albino gray squirrels, mammals with cone rich central retina, to investigate a possible relationship between the rod and RGC deficits in albinism (Esteve & Jeffery 1998). The albino squirrels demonstrated near normal (< 5% reduction) peak cell densities, unlike other mammals. Moreover, vision deficits in albino squirrels are expected to be minor, as they are the only albino mammals known to survive in the wild. These results suggest that the albino RGC and rod deficits are related.

Furthermore, the time of a cell's final division is important for determining its trajectory, as uncrossed destined axons form before crossed ones. Therefore, developmental delays found in the albino retina, including the temporal lag in centre to periphery production of cells in the ganglion cell layer and in the formation of the uncrossed axons outgrowth, provide a possible explanation to the shift in albino chiasmatic pathways (Esteve and Jeffery 1998). Also, the reduced RGC density observed in albinism is present early in development, before any connections have been established with target structures or other retinal cells, further supporting the possibility that retinal deficits precede chiasm abnormalities (Jeffery 1997).

Bhansali and colleagues studied the link between spatiotemporal dynamics of RGC production and the reduced ipsilateral projection characteristic of the albino retina (2014). They found fewer $Zic2^+$ RGCs in the VT retina of albino mice compared with the pigmented VT retina at E15.5. This decrease was not compensated by an increase in $Zic2^-$ RGCs, and the total number of postmitotic RGCs ($Islet1/2^+$) in the VT retina was

therefore reduced in albino mice at that time. No similar reduction was detected in the albino DT retina at this time. At E17.5, the number of RGCs in the VT retina was similar in pigmented and albino mice, suggesting that the reduced number of RGCs observed at E15.5 does not persist later in development. Using short-term birthdating assays, researchers showed that fewer $Zic2^+$ RGCs are born at E13 and more $Zic2^-$ RGCs are born at E15 in the albino VT retina compared to the pigmented VT retina, suggesting a delay in RGC production. Due to this delay, RGCs born at E15 may have lost their ability to express Zic2 and instead express contralateral markers such as Islet2. Indeed, a greater number of $Islet2^+$ RGCs was found in the albino VT retina compared with the pigmented retina at E17.5. This suggests that more RGCs are specified to project contalaterally in the albino retina.

Yet, a study of non-albinotic patients with combined occurrence of foveal hypoplasia and misrouting suggests that foveal hypoplasia could result from misrouting or vice versa (Van Genderen et al. 2006). Fundus photography revealed normally pigmented fundi while foveal hyperpigmentation and foveal pit were absent. VEP recordings confirmed the presence of misrouting. Foveal hypoplasia was also found, using fundus photographs, in Aniridia. In this condition, a Pax6 mutation leads to an abnormal iris. However, projections from the retina follow a similar pattern to that present in healthy individuals, as shown by VEP recordings. This suggests that the mechanisms governing the development of the central retina are separate from those regulating chiasmatic pathways (Neveu et al. 2005). These studies demonstrate that foveal hypoplasia and misrouting are not exclusive features of albinism, and propose a retrograde mechanism in which misrouting affects foveal development.

In mice, RGCs are generated during embryonic days E10–19, with a peak production of uncrossed and crossed axons on E13 and E15, respectively. The first axons arrive at the chiasm around E11–12 (Jeffery 2001). In humans, RGCs are produced from fetal week (Fwk) 5 to Fwk 18 (Erskine & Herrera 2014). Though the fovea is the first region to cease cell division, around Fwk14 in humans, it takes up to four years for the foveal pit to reach complete maturation. However, it develops rapidly in infancy and

appears adult-like at 11–15 months after birth (12 weeks in monkeys) (Hendrickson 1992). Retrograde degeneration of RGCs following hemispherectomy in monkeys is inversely correlated with the age of the lesion, with maximal loss of cells seen when the lesion is induced in the first 4–6 months of life. Degeneration is less pronounced from 8 months to adulthood. It is also mostly confined to the central part of the retina. This suggests higher susceptibility of the fovea to environmental cues in the first months of life. Maximal retrograde influence thus correlates with the period of foveal development, which proceeds well after the chiasmal decussation is established (Herbin et al. 1999). Further research on patients with foveal hypoplasia caused by different conditions is required to understand the link between the chiasm and foveal development in albinism.

3.2 Rationale

In glaucoma, increased intraocular pressure (IOP) and ischemia result in the loss of RGCs. This leads to optic nerve (ON) damage, and to subsequent transneuronal degeneration in the retina's main target, the LGN (Malik et al. 2012). The LGN contains two populations of neurons: thalamocortical (TC) relay neurons that receive synaptic contacts from RGCs and terminate in V1, and interneurons that provide feed-forward inhibition to regulate visually evoked responses of TC neurons. While Nissl staining labels both types of neurons, immunocytochemistry with an antibody against parvalbumin (PV) exclusively labels PV-containing relay neurons. A study on monkeys with glaucoma sought to determine whether RGC death in glaucoma causes atrophy in the magno- and parvocellular layers of the LGN. Light microscopy revealed a significant decrease in the number of immune-reactive LGN relay neurons and LGN volume (Yücel et al. 2001), suggesting a correlation between LGN size and the number of tracts traveling through the OR to V1.

The first study to examine the LGN in human albinism revealed, through post mortem examination, a smaller LGN with fused M and P layers (Guillery et al. 1975). Such fusion is likely due to the increased innervation of neighbouring layers by a larger than normal proportion of crossing fibres. High-resolution structural MRI confirmed

significant reductions in LGN volume (Mcketton et al. 2014), reporting respective right and left mean LGN volumes of 165.2 ± 9.6 mm^3 and 157.9 ± 9.8 mm^3 for controls and 105.6 ± 8.7mm^3 and 98.2 ± 6mm^3 for albinism.

Taken together, these findings suggest that decreases in number of central RGCs and LGN volume may result in a reduced number of neurons in the LGN, and in turn in decreased LGN to V1 connectivity.

3.3 Objective and Hypothesis

This study uses diffusion data and tractography to explore the effect of axonal misrouting on retino-geniculo-cortical connectivity. Based on previously reported reductions in LGN volumes in human albinism (Mcketton et al. 2014), we predict that fiber projections from LGN to V1 are also reduced (Figure 29).

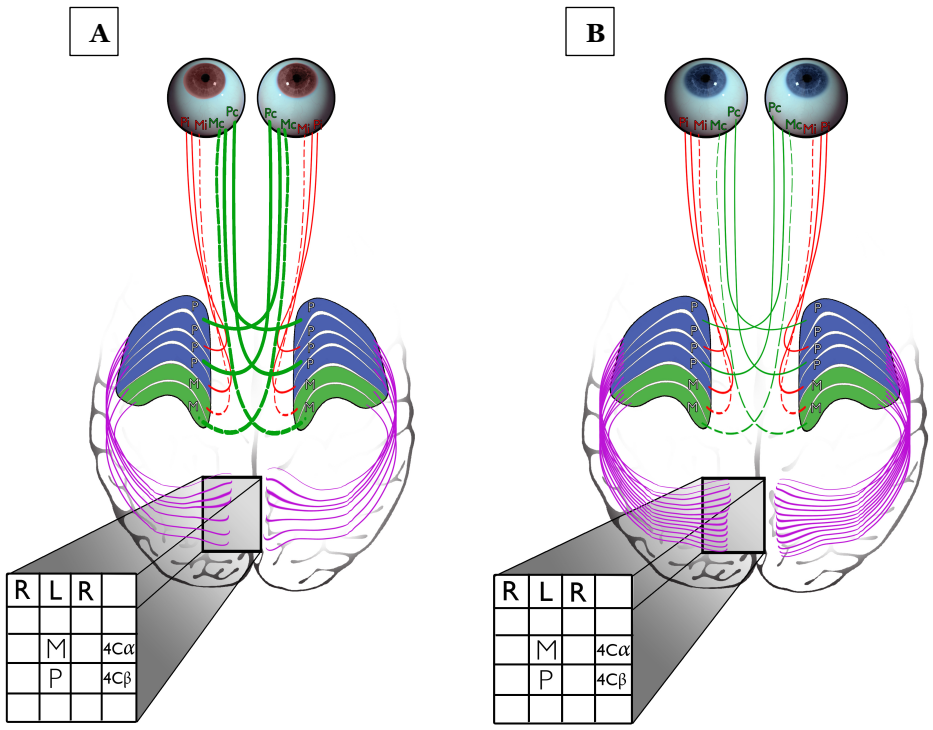

Figure 29: Primary visual pathway in healthy and albino brains. (modified from Mcketton and Schneider 2012). Each LGN receives inputs from both eyes. Ipsilateral retinal projections (red) terminate on Layers 2, 3 and 5, while contralateral projections (green) end on Layers 1, 4 and 6. The LGN sends projections to V1 via the optic radiation (purple), with axons terminating most heavily on V1 Layer 4. Inputs from the two eyes remain segregated in the ocular dominance columns of Layer 4. Beyond this point, inputs from both eyes are combined (binocular neurons in the cortex). (A) In albinism, the majority of temporal optic fibres erroneously decussate to the contralateral hemisphere. (B) In controls, roughly half of the projections extend ipsilaterally from the temporal retina, while the other half arise from the nasal retina and cross at the chiasm to the contralateral hemisphere. This schematic suggests additional abnormalities further downstream the retino-geniculo-cortical pathway, with reduced LGN to V1 connectivity in albinism as confirmed by this study.

3.4 Methods

3.4.1 Subjects

This study was conducted under ethical approval from the Human Participants Review Committee (HPRC) at York University, Toronto. Eleven participants with OCA, aged 36 ± 4years (6 females) were compared to ten age-matched controls, aged 32 ± 4 years (6 females). Participant history is recorded in Table 2.

Table 2: Participant information and health history. Visual acuity was assessed using an Early Treatment Diabetic Retinopathy Study (ETDRS) eye chart and expressed in LogMar (logarithm of the minimum angle of resolution) notation, that is, the logarithm to the base 10 of decimal visual acuity (0.0–1.0 for 20/20-20/200). All controls had normal or corrected-to-normal visual acuity (20/20). No history of neurological disorders was reported.

Albinism					Controls		
Participant	**Age (yr)**	**Sex**	**Classification**	**Visual Acuity**	**Participant**	**Age (yr)**	**Sex**
A1	48	M	OCA	0.6	**S1**	24	F
A2	20	M	OCA-1	0.8	**S2**	22	M
A3	21	M	OCA-1A	1.0	**S3**	25	M
A4	48	M	OCA-1	1.0	**S4**	24	F
A5	43	F	OCA-1	0.8	**S5**	20	F
A6	56	M	OCA	0.9	**S6**	39	M
A7	22	F	OCA	0.6	**S7**	26	F
A8	47	F	OCA	0.9	**S8**	42	F
A9	45	F	OCA	1.0	**S9**	41	F
A10	17	F	OCA-1	0.9	**S10**	60	M
A11	29	F	OCA-2	0.5			

3.4.2 Structural MRI Parameters

All imaging was acquired on a Siemens Trio 3T MRI scanner using a 32-channel head coil. The following scans were collected during a single session per subject:

A high resolution T1-weighted anatomical was acquired using a 3D-MPRAGE sequence covering the entire brain. The following parameters were used: acquisition time 4 min 26 s, field of view 256 mm, 256 matrix, 192 slices with slice thickness of 1 mm, with a resulting isotropic voxel size of 1.0 mm^3, TR = 1900 ms, TE (echo time) = 2.52

ms with an inversion time of 900 ms and flip angle of 9°, 1 average, parallel imaging (iPat GRAPPA, acceleration factor of 2).

Next, the DTI sequence was acquired. Coverage always included cortex, with slices in a transverse orientation following the anterior commissure/posterior commissure (AC-PC) line. The following parameters were used: acquisition time 8 min 5 s, field of view 192 mm, 128 matrix, voxels 1.5 × 1.5 mm in-plane, 56 contiguous (no gap) slices with 2 mm thickness, TR = 6900 ms, TE = 86 ms, 64 directions, b-value of 1000 s/mm^2, 1 average, parallel imaging (iPat GRAPPA) with an acceleration factor of 3.

Lastly, 30–40 proton density (PD)-weighted images were acquired in a coronal orientation, parallel to the brain stem, covering from the anterior extent of the pons to the posterior portion of the inferior colliculus. Turbo spin echo (FAST spin echo) pulse sequence was used. The following parameters were used: acquisition time 1 min 29s per scan, field of view 192 mm, 256 matrix, 30–40 slices with thickness of 1mm, resulting voxel size 0.75 × 0.75 × 1 mm^3, TR = 3000 ms, TE = 22ms, turbo factor of 5, refocusing flip angle of 120°, 1 average, parallel imaging (iPat GRAPPA) with an acceleration factor of 2. Note: S12 was scanned using the following parameters: field of view 180 mm, 512 matrix, 30 slices with 1 mm thick slices, resulting voxel size 0.4 × 0.4 × 1.0 mm^3. All other parameters remained the same. Acquisition time 2 min 47s.

All scans were pre-processed by converting raw DICOM to NIfTI format required for use by FSL and DSI studio.

3.4.3 LGN Delineation and V1 Segmentation

The LGN is a small subcortical structure located deep in the brain, hence high-resolution PD images are required to determine its anatomical boundaries. In these scans, the LGN appears as an area of high signal intensity relative to the surrounding WM tracts, facilitating its detection (Fujita et al. 2001). In FSL (Smith et al. 2004), three raters blind to group membership manually traced right and left LGN masks three times each on averaged PD images interpolated to twice the resolution and half the voxel size (original 256 × 256 matrix, 0.75 × 0.75 × 1 mm^3 voxel size). Each rater's ROIs were then merged

into a median mask, and individual median masks were then merged into all-raters-median masks.

FreeSurfer (FS) (v5.3.0) segmentation (Fischl 2012) was used for V1 segmentation. Recon-all for automated processing was run on participants' T1-weighted images. The appropriate outputs in the newly created mri folder (orig.mgz, brain.mgz, rawavg.mgz, T1.mgz) were then converted to NIfTI. Brain extraction tool (BET) was applied to correct the skull-stripped output brain (brain.nii.gz) in FS space if necessary. Recon-all output V1 parcellation from the newly created label folder was converted to a volumetric mask using **label2surf** and **surf2volume** commands, which required the brain file in FS space.

3.4.4 Probabilistic Tractography

Diffusion-weighted images were corrected for distortions using Eddy current correction and brain extracted with BET. FSL's tool dtifit was then run to fit a diffusion tensor model at each voxel, creating files for post-processing. Next, BedpostX (estimation of diffusion parameters) generated all files required for tractography.

FLIRT linear registration was used to transform participants' PD brains to anatomical T1 space and to FreeSurfer (FS) space. Transformations were applied to LGN masks using nearest-neighbour interpolation. FS brains were transformed to T1 space and transformations were applied to V1 masks using tri-linear interpolation. T1 and FS brains were linearly registered to diffusion space. FLIRT linear registration creates two outputs, the input brain registered to the reference image (.nii.gz) and a transformation matrix (.mat). The latter file is required for tractography when seed space is not diffusion.

Tracking was run for each hemisphere separately. ProbtrackX for probabilistic tracking was run in DTI space with seed (LGN) and target (V1) masks in T1 space, and the appropriate .mat file as the seed to diffusion transformation matrix. It was also run with the appropriate transformation matrix and seed and target masks in FS space with the addition of the contralateral white matter border mask (in FS space) as an exclusion mask, to avoid any crossing over. Default basic options were used (5000 samples, 0.2

curvature and loopcheck applied) and modified Euler for computing probabilistic streamlines from advanced options was selected for increased accuracy. All steps were performed in FSL (v5.0.4).

ProbtrackX was also run with a standard spherical ROI as the seed region. The following steps were performed to normalize LGN masks in T1 space: FNIRT non-linear registration was applied to bring participants' non-extracted anatomical brains to MNI space using the Montreal Neurological Institute whole brain template (MNI152). Transformation was then applied to LGN masks in anatomical space using nearest-neighbour interpolation. All LGN masks were then averaged in MNI space across both groups and the mean mask was thresholded. The radius of the mean mask in MNI space was then calculated using $V=4/3\pi r^3$ (assuming a sphere). The centre of mass (COM) coordinates of each individual LGN mask in anatomical space was recorded. Spherical ROIs of identical volumes across participants were created in anatomical space using the recorded COM coordinates and the calculated radius. Standard ROIs were only created in anatomical space.

It is important to emphasize that tractography is always run from diffusion space, but probtrackx for probabilistic tracking allows the input of seed and target masks in a different space, along with a transformation matrix to diffusion space. In this study, probabilistic tractography was run with masks in both anatomical (T1) and FS space (Figure 30).

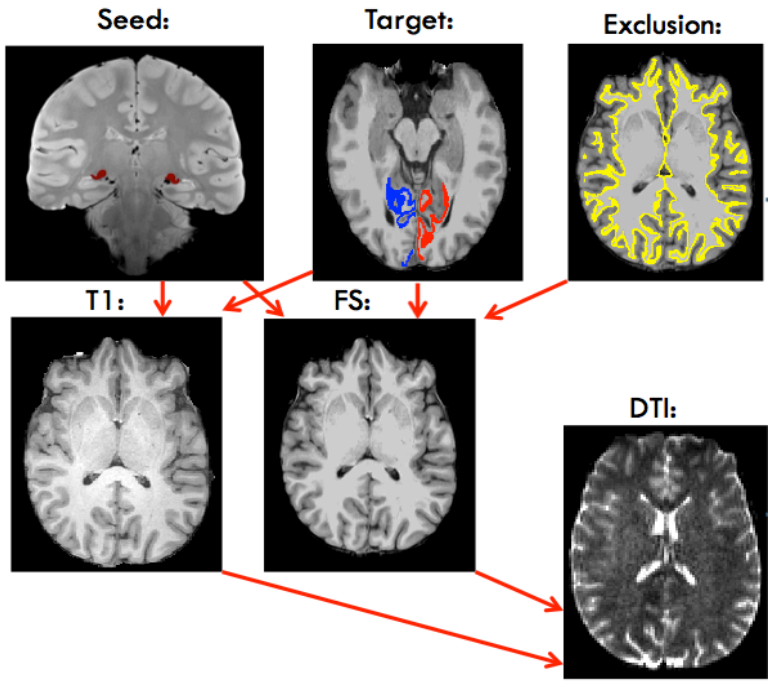

Figure 30:Probabilistic tractography pipeline. FLIRT linear registration was used to transform participants' PD brains to anatomical T1 space and to FreeSurfer (FS) space. Transformations were applied to LGN masks using nearest-neighbour interpolation. FS brains were transformed to T1 space and transformations were applied to V1 masks using tri-linear interpolation. T1 and FS brains were linearly registered to diffusion space. PROBTRACKX2 for probabilistic tracking was run in DTI space with masks in T1 and FS space (LGN as seed, V1 as target, contralateral white matter border as exclusion mask when run from FS space). Red arrows indicate registration.

3.4.5 Deterministic Tractography

Eddy corrected diffusion-weighted images were opened in DSI Studio (Yeh et al. 2013) and bvec and bval files, generated upon DICOM to NIfTI conversion, were loaded onto a b-table window to create a source (.src) file. Source files were opened and the default reconstructed brain masks were modified as necessary.

Next, a DTI reconstruction model (Jiang et al. 2006) was applied to the source files to produce fiber information files (.fib). These .fib files were then opened in the program's tracking window.

Participants' PD brains were transformed to diffusion space and transformations were then applied to LGN masks using nearest-neighbour interpolation. Tracking was run for each hemisphere separately. LGN masks in diffusion space were loaded onto the .fib

files in the tracking window and set as seeds. Region 17 (V1) from Brodmann atlas available from DSI Studio, was set as a terminative region. In each run, the contralateral WM (named left/right-cerebral-white-matter) mask from FreeSurfer segmentation atlas was loaded and set as an ROA. Tracking was repeated using standard spherical ROIs in diffusion space instead of individual LGN as the seed region.

For most runs, default tracking parameters were applied. For some individuals (A5, A7, S12), anisotropy threshold (default .14–.15) was lowered (.10–.12) and angular threshold (default 60) was increased (65–85) for nicer visualization. A schematic of the technique is shown in Figure 31.

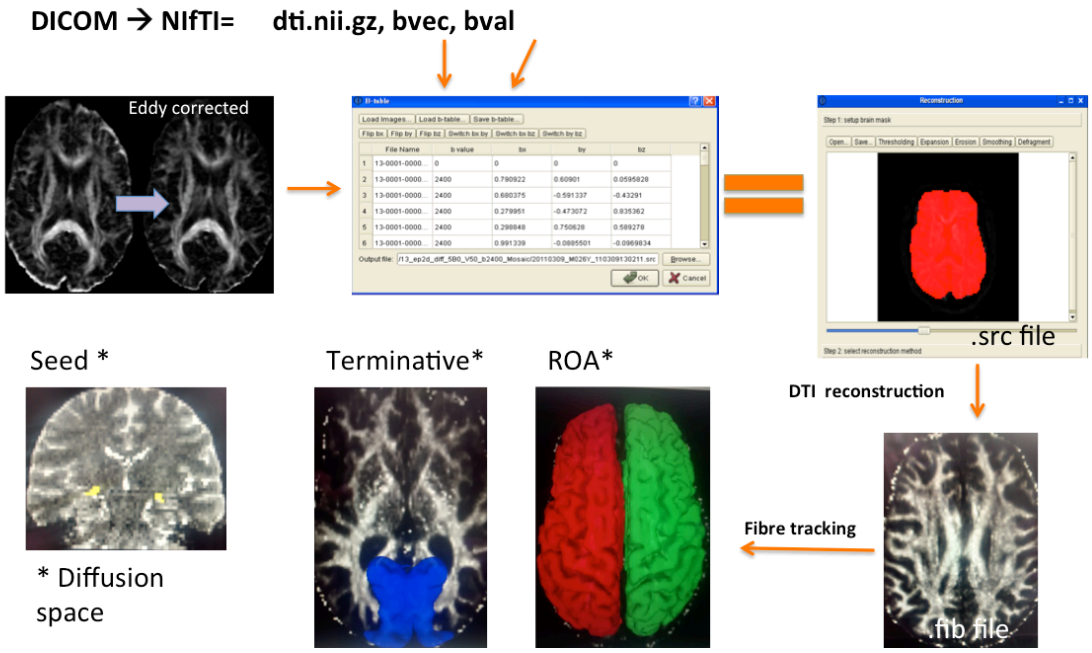

Figure 31: Deterministic tractography pipeline. Eddy corrected diffusion-weighted images were opened in DSI Studio and bvec and bval files were loaded onto a b-table window to create a source (.src) file. Source files were opened and the default reconstructed brain masks were modified as necessary. Next, DTI reconstruction model was applied to the source files to produce fiber information files (.fib). LGN masks in diffusion space were loaded onto the .fib files in the tracking window and set as seeds. Region 17 (V1) from Brodmann atlas was set as a terminative region. In each run, the contralateral WM mask from FreeSurfer segmentation atlas was loaded and set as an ROA.

3.4.6 Statistical Analysis-TBSS

Tract-based spatial statistics is a voxelwise statistical analysis of participants' FA maps (Smith et al. 2006) obtained with dtifit (Smith et al. 2004). It is extensively used for statistics on diffusion data. This voxelwise approach overcomes potential alignment and smoothing problems seen in VBM-style FA analysis and provides whole brain investigation, unattainable through tractography-based approaches (Smith et al. 2006).

It solves such issues through non-linear registration of each subject's FA data into a common space, followed by projection of each subject's aligned FA image onto a "mean skeleton" of all aligned FA images. No spatial smoothing is required for image processing (Smith et al. 2006).

To run TBSS, a newly TBSS directory was first created and participants' FA maps were placed there. The FA data was then pre-processed using the **tbss_1_preproc** command. Next, **tbss_2_reg -T** was run to apply non-linear registration, bringing each participant's FA data into common space (FMRIB58_FA, target image in TBSS). A mean FA skeleton with the centers of all common tracts among participants was then created using **tbss_3_postreg -S.** Each participant's aligned FA map was then projected onto the mean skeleton of all aligned FA maps using **tbss_4_prestats 0.2**. The last step in the analysis, running randomise, requires design.con and design.mat files. When creating these files, the order of the matrix must be consistent with the order in which TBSS pre-processed the FA data. Once these files were obtained, **randomise** was run. The T2 option, which is recommended for TBSS as it acts on a skeleton (a reduced subset of the 3D data), and 5000 pre-mutations, which gives more accurate p-values- were used.

3.4.7 Statistical Analysis-SPSS

Mean FA and streamline count were used to explore LGN to V1 connectivity. FA is one of the most commonly reported measures derived from diffusion data. It is most accurately described as a quantification of how strongly directional diffusion is in a region. It is important to note that group differences in FA measures do not necessarily imply differences in white matter integrity. Since this study involves a clinical condition

with a potential effect on white matter, such interpretation can be justified. However, while reduced integrity suggests structural damage or decline, FA in a region may be lowered due to fewer barriers such as larger axon diameters and less densely packed axons, as well as due to less effective boundaries resulting from increased membrane permeability (Jones et al. 2013).

Deterministic-based FA values were recorded from DSI Studio output statistics text files. These values represent the mean FA within the generated tracts, which in this case correspond to the region of the OR. Probabilistic-based FA values were derived from ProbtrackX2 output fdt_paths files. These are 3D tract density images that in this study covered the area corresponding to the OR. Participant's fdt_paths files were linearly registered to diffusion space, binarised and multiplied by the participant's FA map from dtifit. The **fslmeants** command was then applied to find the mean FA from each tract mask.

The term 'streamline count', is preferred over 'fiber count', since the number of reconstructed streamlines may not be a true representation of the number of actual fibers due to variations in pathway features such as length, curvature and branching, as well as experimental conditions such as signal-to-noise ratio (SNR) (Jones et al. 2013).

In this study, streamline count was based on waytotal values. Waytotal describes the total number of generated streamlines that have not been rejected by inclusion/ exclusion criteria (Galantucci et al. 2011). The number of generated streamlines (NGSL), which refers to the total number of streamlines sent, is equal to the number of voxels in the seed mask multiplied by the number of samples drawn from each voxel (5000 in this case). Percentage generated streamlines (PGSL), waytotal divided by NGSL times 100, is a measure of successful connectivity between the seed and the target. Both waytotal and PGSL were used for statistical analysis.

Statistical analysis was performed using SPSS 20 for Mac. Since hemisphere is a within-subject variable, a generalized linear model (GENLIN) with which the effects in each side of the brain can be looked at separately, was applied. In separate tests, each of mean FA and streamline count (waytotal or percentage generated streamlines, PGSL)

were set as the dependent variable. The influence of the independent variables of group and gender on LGN to V1 connectivity was studied. LGN volume and age were used as covariates.

Main effects as well as two- and three-way interactions were studied. It is important to note that these individual tests are not conditioned to each other, so the significance of one main effect or interaction is independent of the other. The level of significance was $p < .05$, and Bonferroni correction was used to adjust for multiple comparisons (Cabin & Mitchell 2000). Since Bonferroni is a very conservative test, p values smaller than .1 were treated as approaching significance, and the trends were recorded. Note: Total brain volume was found to be an insignificant covariate and was therefore omitted from stats.

3.5 Results

This section provides a summary of results obtained using two different algorithms of tractography, deterministic and probabilistic. LGN volumes in PD space, in which masks were originally drawn, are recorded in Table 3, and LGN tracing is illustrated in Figure 32. Statistical analysis was run using LGN volume as a covariate, with a median mask of the most experienced rater. LGN volumes versus raw waytotal values from probabilistic runs were plotted in Figures A1-A2. These plots demonstrate a positive relationship between LGN volume and the size of generated streamlines, with larger values recorded in controls. Figure B1 demonstrates a similar relationship in data from the deterministic run. Moreover, probabilistic tractography was run using all-raters-median LGN masks, in which the medians of three raters were combined (Figure A3). No significant differences were observed between the one rater- and median of the median-masks, confirming the expected inter-rater consistent measurements (ICC > 0.70 for both intra- and inter-rater reliability) (Cohen 2001). Statistics with LGN size controlled through normalization was also performed. Resulting trends obtained with both statistical analyses were mostly comparable. Only results from runs that used a standard sphere as the LGN ROI are reported here. Standard LGN volume was 461 mm^3 in both

hemispheres in anatomical space (probabilistic run), and 292.5 mm^3 and 364.5 mm^3 in the right and left hemispheres, respectively, in diffusion space (deterministic run). For both runs, these standard volumes are very close to the mean volumes calculated in MNI space (anatomical to MNI: 472 mm^3 and 440 mm^3 for left and right, respectively; diffusion to MNI: 376 and 312 mm^3 for left and right, respectively) but larger than most individual LGN volumes in native space (largest in anatomical: 281 mm^3; largest in diffusion: 324 mm^3).

Table 3: A summary of LGN volumes. The volumes recorded in this table (mm^3) are of right and left LGN of patients and controls in PD space in which masks were originally drawn. These volumes were calculated from one rater's median masks. Lists of volumes in other spaces used in the study are not reported here. Instead, volume ranges are provided. In diffusion space, LGN volume ranges from 31.5–193.5 mm^3 for albinism and 103.5–324 mm^3 for controls. In MNI space, 96–520 mm^3 for albinism and 328–864 mm^3 for controls. In anatomical space, 54–202 mm^3 for albinism and 112–281 mm^3 for controls. In FreeSurfer space, 40–212 mm^3 for albinism and 112–292 mm^3 for controls.

Albinism			Controls		
Participant	**LLGN (mm^3)**	**RLGN (mm^3)**	**Participant**	**LLGN (mm^3)**	**RLGN (mm^3)**
A1	47.8	70.73	**S1**	200.95	234.12
A2	195.05	175.5	**S2**	158.34	165.23
A3	191.25	181.13	**S3**	172.13	183.8
A4	118.81	99	**S4**	152.58	119.11
A5	127.83	132.47	**S5**	276.19	229.36
A6	127.83	75.09	**S6**	186.61	201.52
A7	114.68	104.7	**S7**	241.72	249.62
A8	63.49	49.15	**S8**	196.1	112.43
A9	80.79	104.55	**S9**	211.5	236.39
A10	120.37	122.34	**S10**	193	150.82
A11	68.98	92.46			

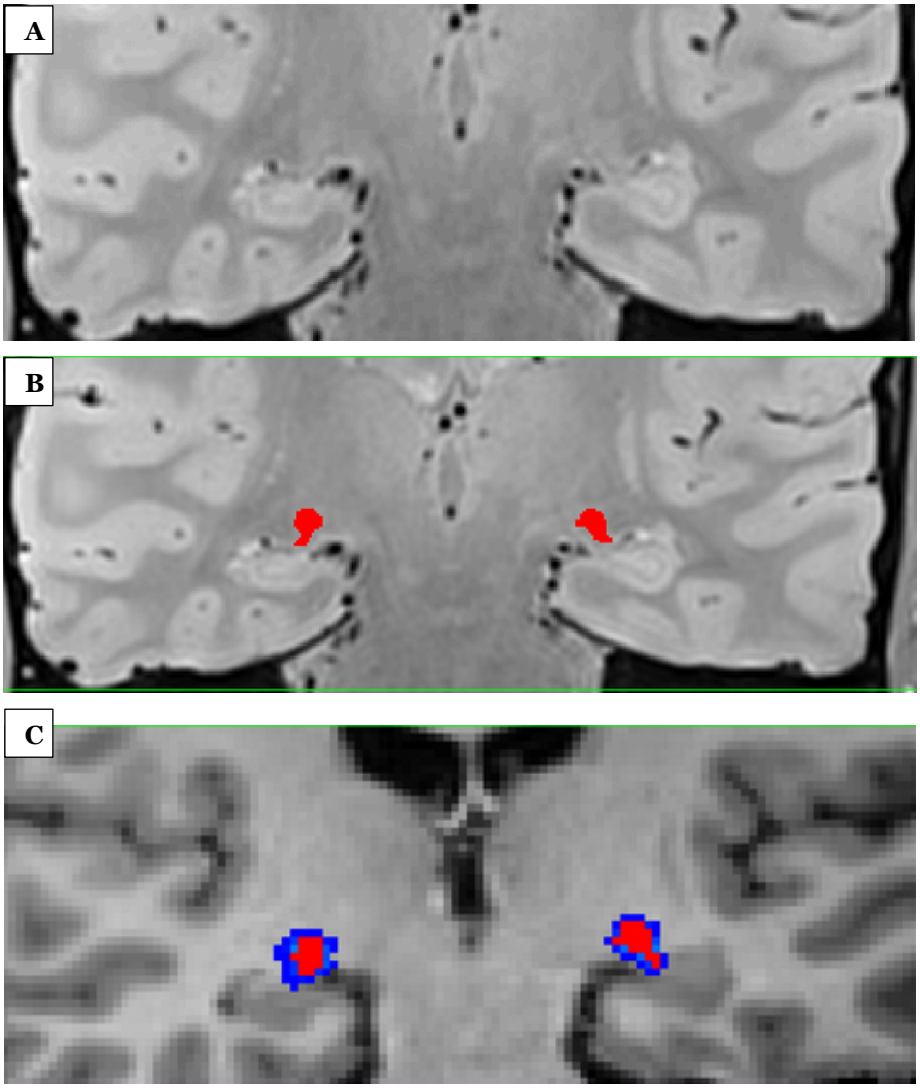

Figure 32: LGN mask delineation on a PD scan. A) Zoomed-in view of right and left LGN on an averaged coronal PD-weighted image slab that was interpolated to twice the resolution and half the voxel size in an albino patient, A11. B) Manually traced right and left LGN areas of interest (ROIs) in red C) Manually traced LGN ROIs with nearest neighbour interpolation in red, and tri-linear interpolation in blue. The former was applied in this study for more accurate delineation of the structure.

3.5.1 Probabilistic Tractography

Using mean FA values from fdt_paths as the dependent variable, the main effect of group was insignificant (mean ± SEM .353 ± .0035 controls; .349 ± .0046 albinism). However, the main effects of hemisphere (.358 ± .004 right; .345 ± .003 left, p = .005) and gender (.34 ± .004 females; .36 ± .004 males, p = .014) were significant.

Data were normally distributed (Shapiro $p > .05$). Pairwise comparisons revealed reduced FA in the left hemisphere compared to the right hemisphere in both groups ($p = .012$). In males, FA was significantly reduced in albinism compared to controls ($p = .039$). Also, FA was significantly decreased in females compared to males in controls ($p < .001$).

Using waytotal values and PGSL as dependent variables, the main effects of group, hemisphere and gender were not significant. Mean waytotal values were 28739 ± 7297 for albinism and 31220 ± 7202 for controls. Mean PGSL from LGN to V1 were 1.3 ± .3 for albinism and 1.4 ± .3 for controls. In both cases, data were non-normally distributed and gamma log transformation was applied. Pairwise comparisons revealed decreased connectivity in the right hemisphere of males compared to females ($p <.001$). Outputs of probabilistic tractography are illustrated in Figure 33.

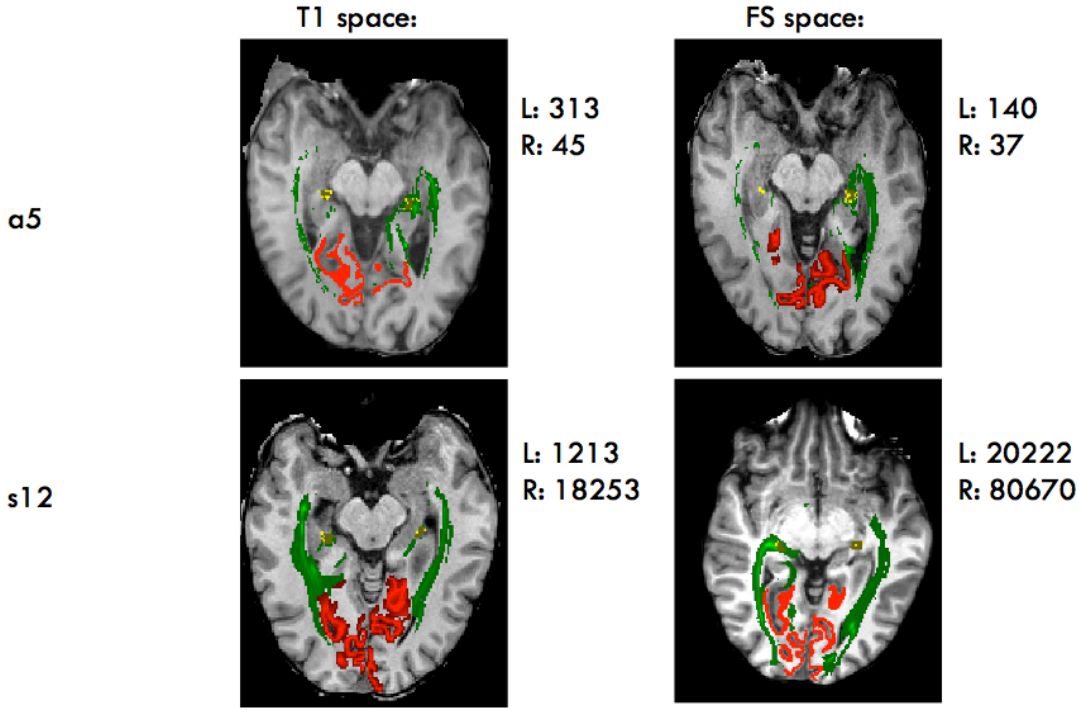

Figure 33: Output of PROBTRACKX for probabilistic tracking. Reduced LGN to V1 connectivity in albinism compared to controls (LGN in yellow, optic radiation in green, V1 in red). Note: this is an example of a run with non-normalized LGN masks.

3.5.2 Deterministic Tractography

Data for all tests were normally distributed as confirmed by the Shapiro-Wilk test ($p > .05$). Using mean FA as the dependent variable, main effects of group and gender were insignificant, while the main effect of hemisphere approached significance (means ± SEM .41 ± .008 right; .39 ± .006, $p = .064$). Means (± SEM) of mean FA values corresponding to the OR region connecting the LGN to V1 were 0.39 ± 0.007 for albinism and 0.40 ± 0.008 for controls. Pairwise comparisons revealed reduced FA in the right hemisphere of albinism compared to controls ($p = .042$). In controls, the left hemisphere FA value was lower than that for the right hemisphere ($p = .007$), and a trend for decreased FA in females compared to males was found ($p = .085$).

Mean waytotal values were 2728 ± 127 for albinism and 2753 ± 169 for controls. Pairwise comparisons revealed reduced connectivity in male albinos compared to male controls ($p = .031$). In both groups, connectivity in the left hemisphere was lower compared to the right hemisphere ($p = .037$). Additionally, connectivity was lower in males compared to females in the albinism group ($p = .034$), while the opposite was seen in the control group ($p = .049$). Lastly, in females, a trend for decreased connectivity was seen in controls compared to albinism ($p = .061$). Using PGSL as the dependent variable, the main effects of group and gender were insignificant, while the effect of hemisphere was significant (means ± SEM .89 ± .045 right; .63 ± .026, $p = .001$) Mean PGSL from LGN to V1 were .76 ± .046 for albinism and .76 ± .048 for controls. PGSL were calculated using standard LGN ROI. Pairwise comparisons revealed similar results to those obtained with waytotal values. Outputs of deterministic tractography are illustrated in Figure 34.

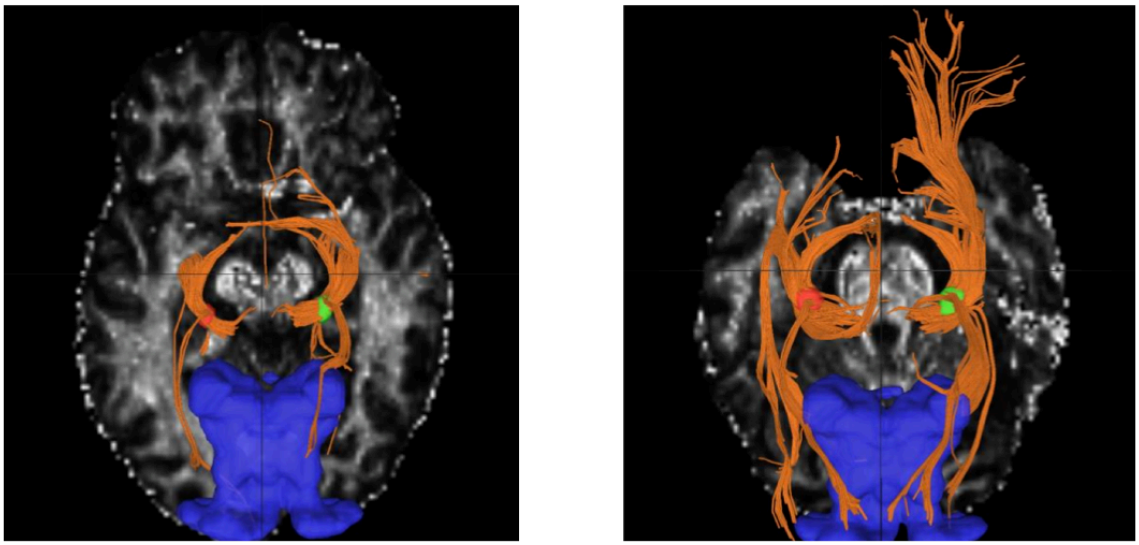

Figure 34: Output of DSI Studio fiber tracking. Left: Reduced LGN to V1 connectivity in albinism patient A1 (lowest number of reconstructed tracts in right hemisphere, 1365) compared to, Right: controls (S6, highest number of reconstructed tracts in right hemisphere, 4355) (left LGN in red, right LGN in green, LGN connections to optic tract and OR in orange, V1 in blue).

3.5.3 TBSS

TBSS on FA maps revealed areas of significant difference ($p < .05$) between the two groups, with areas in red representing regions of reduced white matter tract integrity in albinism (Figure 35).

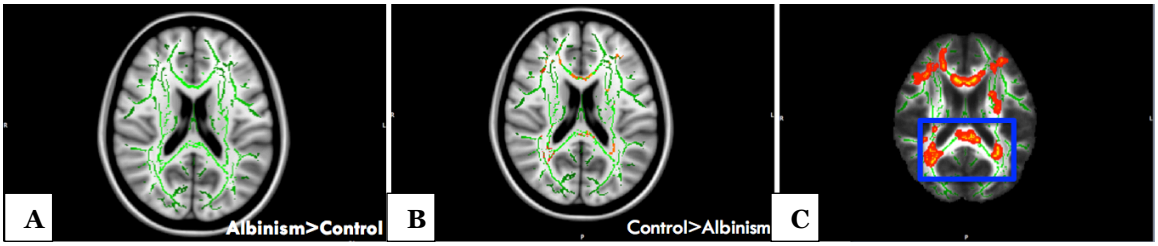

Figure 35: Voxelwise statistical analysis with TBSS. Whole brain voxelwise statistical analysis of FA data was carried out using tract-based spatial statistics (TBSS). Non-linear registration of all participants' FA images to a common space was performed, followed by the creation of a mean FA skeleton and the projection of each participant's FA image onto the skeleton. A) Albinism > control contrast showing skeleton in green with no areas of significance due to reduced FA in albinism compared to controls. B) Significant difference between the control group and the albinism group detected, with areas in red representing regions (cerebral white matter corresponding to optic radiation fibres and calcarine cortex, on which they terminate) of reduced white matter tract integrity in albinism, for the control>albinism contrast (TFCE (threshold-free cluster enhancement) corrected, $p < .05$), C) Thickened skeletonised version of results displayed in B, for visual representation.

4. Discussion and Conclusion

4.1 General Discussion

Altered WM and more specifically, decreased connectivity in albinism compared to controls were expected. Thus, the reduced FA in the right hemisphere of albinism compared to controls as well as the decreased connectivity in male albinos reported here are in line with our prediction. Gender and hemisphere effects are not completely clear, although research on the healthy brain suggests decreased WM complexity in the left hemisphere of males compared to females (Farahibozorg et al. 2013; Tian et al. 2011) and could explain some of the gender- and hemisphere-related differences observed in this study. Reduced connectivity in male albinism compared to female albinism may be in part due to the younger average age of females in both groups (7–8 years < males), as reduced WM volume was reported in mid-adulthood in the healthy brain (Ge et al. 2002; Zhang et al. 2007). Gender differences may also be due to the small sample size and the uneven number of males versus females in each group (5 males OCA, 4 controls). The increased connectivity observed in female albinism compared to controls of the same gender was not expected, and might suggest some sort of a compensatory mechanism in albinism. However, this finding could instead be attributed to the great variability within a small population sample.

Tractography is the only non-invasive technique for mapping WM *in vivo*. In the deterministic approach, termination occurs when anisotropy drops below a certain level, or when there is an abrupt angulation. However, most voxels contain fibers in more than one direction, and the deterministic approach is limited to either identifying the dominant tract in a voxel or an "average" of all directions within a voxel. It thus fails to provide a true representation of neuronal pathways. Probabilistic tractography allows the resolution of two fiber models in a single voxel, providing a more reliable representation of a tract, and tracking in areas of low anisotropy (Newcombe et al. 2013). The probabilistic algorithm was therefore particularly advantageous in this study, which investigated the

trajectory of the OR, a highly branching WM structure (particularly the portion of Meyer's loop), terminating in the gray matter of V1. Although probabilistic tractography is believed to follow the true course of nerve fibres more closely, deterministic tractography was run to compare the usefulness and reproducibility of both techniques. Since trends were detected using the probabilistic approach, similarities seen in the deterministic run only further strengthened the validity of the results.

Apart from its increasing use in research on mapping anatomical connectivities in the brain, tractography has shown promising advances in neurosurgical panning. Visualization of OR during resection of tumours by neuronavigationally transferring DWI data into the operative field was reported to help in successfully removing lesions and keeping the visual fields intact (Coenen et al. 2005). Nevertheless, DTI has limitations such as relatively poor spatial resolution and impaired data quality when structures with low fiber density such as the OR are studied (Hofer et al. 2010). Though probabilistic tractography was the preferred technique, the current study aimed to compare the two algorithms. Both tracking algorithms revealed some common findings, increasing the reliability of the results.

LGN volume ranges from 110–276 mm^3 in healthy brains (McKetton et al. 2014) and correlates with volumes of the visual cortex and the optic tract, but not with overall brain volume (Andrews et al. 1997). Since tractography depends on the number of voxels in the seed mask, LGN volume should be normalized across participants to prevent bias in quantitative comparisons between tracts (Bridge et al. 2008). PGSL calculations and spherical ROIs of a standard size are two approaches to control for LGN volume in the statistical analysis, and both were used here. Creating spherical ROIs requires registration of subjects' anatomical brains to MNI space. Non-linear registration of original anatomical images is recommended for this step, as registrations were more accurate when FNIRT was applied to non-extracted T1s compared to FLIRT on extracted brains. Standard LGN volumes obtained here were close in size to the mean volumes calculated in MNI space, but larger than most individual LGN volumes in native space. This ensures the inclusion of all voxels that are part of this structure in all participants. Moreover,

though using a large mask size would usually increase the risk for false positives, such concern does not apply when seeding in a structure such as the LGN, which differs in connectivity patterns from surrounding nuclei. Hence, voxels belonging to other structures will generate streamlines that do not follow the expected paths and such paths will therefore be discarded (Behrens et al. 2003). The normalized results reported here show significantly weaker thalamo-cortical connectivity in albinism compared to controls that is beyond the effect of smaller LGN size demonstrated in the non-normalized runs.

Another approach for LGN normalization is the addition and removal of voxels around individual LGN masks to obtain a standard size across subjects using a MATLAB script. This approach does not require any additional registrations and therefore limits the degree of deformation of the brain images and increases accuracy. It also retains the LGN outline rather than creating a sphere around the LGN region. However, to minimize human error, multi-atlas segmentation may be used instead of manually tracing the LGN masks. Using a set of atlases accounts for individual structural variability and therefore yields a more accurate representation of a subcortical region than a single atlas (Asman & Landman 2013).

4.2 Human Optic Radiation Tractography

The OR consists of three fibre bundles: the anterior ventral fiber bundle, also known as Meyer's loop, the central bundle and the dorsal bundle (Figure 36). Its complex anatomic path varies considerably among individuals. Many pathological conditions that affect the OR result in visual field abnormalities. Even more frequently, visual field deficits are induced by damage to the OR during tumour resection. Therefore, successfully localizing this region in the brain is crucial during neurosurgery (Hofer et al. 2010). It is especially critical since the OR is not visible under the operative microscope, and surgeons therefore rely solely on their anatomical knowledge and operative experience.

To lower the surgical risk, anatomical landmarks that are visible under the operative microscope have been defined to more accurately estimate the exact location of the OR. Moreover, an approach has been developed that involves mapping of myelin-stained histological sections of human brains onto an MRI volume of a reference brain. Warping of histological volumes to a reference brain by linear and nonlinear transformations produces brain atlases that demonstrate intersubject position and spatial variability of the OR, improving anatomical localization of the OR and infiltrating lesions. However, positional displacement or deformation of the OR by a lesion limits the usefulness of these approaches (Coenen et al. 2005).

Unlike these approaches, DTI-based tractography allows in vivo determination of OR anatomy in individual brains (Hofer et al. 2010). It allows both preoperative planning and intraoperative guidance by neuronavigationally displaying preoperative DWI data into the operative field. Coenen (2005) and colleagues report the first OR visualization with DWI during tumour resection. Visual fields were successfully maintained in all four patients, demonstrating the potential of DWI-guided resections to reduce operative error.

Despite its promising advances in neurosurgical planning, DTI-based tractography introduces limitations such as poor spatial resolution. Moreover, reconstruction of the elongated fibre pathways comprising the human visual system is particularly challenging. In parts of the OR like Meyer's loop where it curves out off its horizontal plane, the change in fibre direction results in a loss of signal. Edema around tumours, which appears as an area of high intensity on DWI scans, may also constitute a challenge. This is because edema formation results in reduced anisotropy, which may impair the detection of fibres around a tumour. Also, opening the dura and tumour debulking result in the loss of CSF, which leads to brain shift. This may in turn interfere with neuronavigational accuracy, as intraoperative display of OR consists of preoperative images (Coenen et al. 2005).

Though the OR consists of large axons surrounded by thick myelin sheaths, it has low fibre density with wide translucent spaces between axons. These histological

characteristics are translated into low signal intensity on T1-weighted images and high signal intensity on T2-weighted images (Kitajima et al. 1996). Therefore, DTI data acquisition requires a technique that minimizes signal loss or geometric distortions and allows adequate SNR ratio. Single-shot stimulated echo acquisition mode (STEAM) MR imaging is insensitive to differences in tissue susceptibility, magnetic field inhomogeneities and chemical shifts. It therefore avoids regional signal losses, high intensity artifacts and geometric distortions. However, it exhibits lower SNR compared to echo-planar imaging (EPI), but this can be improved using parallel imaging (Hofer et al. 2010).

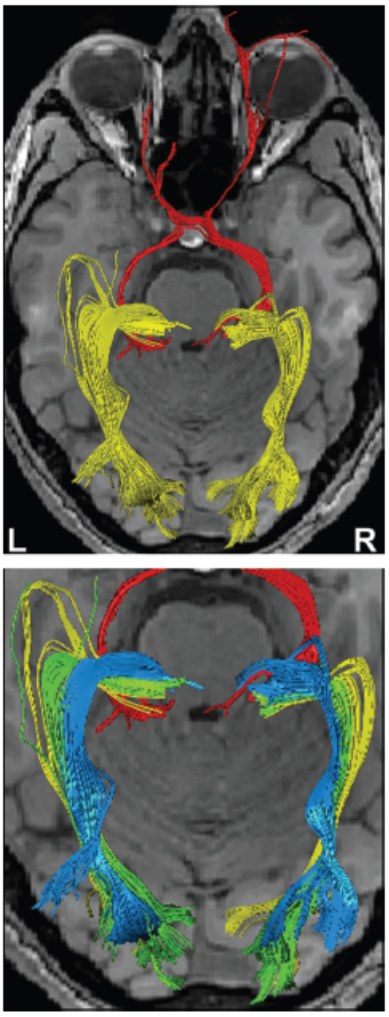

Figure 36: OR tractography. Meyer's loop in yellow, central bundle in green and dorsal bundle in blue (Hofer et al. 2010).

4.3 Other Disorders

4.3.1 Dyslexia

Developmental dyslexia (DD) is a neurobiological reading disability in individuals who experience difficulties with reading, writing and spelling, but otherwise show normal intelligence. It affects about 7% of the population, and about 75% of people identified with learning disabilities (Steinbrink et al. 2008). It can also affect cognitive processes such as memory, speed of processing and coordination. It has been demonstrated that dyslexics take longer to distinguish two presentations of successive

visual stimuli, and have trouble distinguishing the order of two rapidly flashed visual stimuli, while their performance on tasks involving prolonged stimuli is normal. This suggested an abnormality in the part of the visual system that is fast and transient, with high contrast sensitivity and low spatial selectivity, properties attributed to the magnocellular pathway.

Livingstone and collaborators (1991) recorded visually evoked potentials in both dyslexic and non-dyslexic subjects, and found reduced responses to rapid, low-contrast stimuli but normal responses to prolonged, high-contrast stimuli in the dyslexic population (Livingstone et al. 1991). This supports the theory of a magnocellular dysfunction. While the parvocellular layers of the LGN appeared similar in both groups, post-mortem measurements revealed smaller magnocellular cell bodies in the LGN of dyslexic brains. At the functional level, smaller cell bodies are likely to possess thinner axons, which are associated with slower conduction velocities. This supports the notion that visual processing in dyslexic individuals is slower compared to non-dyslexic individuals.

Giraldo-Chica and colleagues (2015) found reduced LGN volumes in the left hemisphere of dyslexics. Based on that and on the reported link between poor reading and disruption of neuronal pathways in the temporo-parietal cortex (Deutsch, et al., 2005; Carter, et al., 2009), they hypothesized that the LGN exhibits abnormal connectivity in dyslexia. Based on their DWI data and probabilistic tractography, they reported reduced PGSL between LGN and V1 in dyslexia.

Though it is not a direct measure of the number of axonal projections, the number or percentage of reconstructed streamlines provides information about the connectivity distribution between two brain regions. Like in our study, this work demonstrates the usefulness of tractography in mapping the OR. It shows that, similar to albinism, dyslexia exhibits abnormal LGN morphology that alters downstream connectivity.

4.3.2 Achiasma

Achiasma, also known as non-decussating retinal fugal fibre syndrome (NDRFFS), is a very rare condition in which the optic chiasm is completely absent, and nasal RGCs project ipsilaterally. As a consequence of both hemiretinae projecting to the same side of the brain, each hemisphere receives input not only from the contralateral, but also from the ipsilateral visual hemifield. The absent crossing was demonstrated by VEPs, which showed activation of V1 primarily by the ipsilateral eye (Apkarian et al. 1994). This unilateral cortex activation was later confirmed by fMRI. Each hemisphere mapped the whole visual field, with both halves of the visual field overlapping completely (Victor et al. 2000).

Despite the extensive miswiring, visual performance that depends on exact geometric information such as vernier acuity appeared normal. Yet, velocity judgement and contrast sensitivity were altered. These abnormalities, however, are likely due to congenital nystagmus observed in affected individuals rather than the misrouting. Relatively normal vision may be attributed to the plasticity of visual pathways, which transmit visual information between hemispheres. Particularly, pathways such as the corpus callosum and the anterior commissure, are involved in interhemispheric transfer and appear normal as demonstrated by MRI (Victor et al. 2000).

In achiasmatic Belgian sheepdogs, the erroneously ipsilateral projecting nasal fibres contact the LGN as if they successfully crossed at the chiasm and terminated in the appropriate layers (Williams et al. 1994). As a result, V1 columns, normally segregated by ocular input, would alternatively be innervated by the two hemifields. DTI-based tractography revealed normal OR anatomy in achiasma. With the exception of nystagmus and absence of stereopsis, visual function is relatively unaffected, as a result of conservative geniculocortical and cortico-cortical mapping of abnormal visual input (Hoffmann et al. 2012).

Achiasma, similarly to albinism, is a phenotype caused by axonal misrouting. Unlike albinism, achiasma shows no alterations in visual pathways beyond the LGN, possibly explaining the differences in visual performance between the two groups.

4.4 Conclusion

This novel *in vivo* study investigates interdependent development among different parts of the primary visual pathway in human albinism. It thus provides further insight into the etiology of this condition and improved diagnosis through identification of disorder-specific signatures. Both probabilistic and deterministic tractography algorithms used here showed comparable patterns of altered LGN to V1 connectivity in human albinism. Reduced WM integrity and connectivity in the OR area in albinism compared to controls were in line with our predictions. Though no generalization to the large population can be made due to the small sample size and the large inter-subject variation in structures of interest, this study demonstrates the usefulness of tractography in detecting trends within the sample population, suggesting the importance of further research in the field. Furthermore, albinism is associated with increased risk of skin cancer and with syndromes affecting additional cell types beyond melanocytes. Examples include HPS, characterized by bruising and bleeding, and CHS, in which the immune system is weakened (Kromberg et al. 1989; Martinez-Garcia and Montoliu 2013). Therefore, combining imaging and molecular techniques to investigate mechanisms of development in this population may assist in treating associated medical outcomes.

5. Future Directions: V1 to LGN Tractography and fMRI-based V1 Organization

Descending feedback projections parallel ascending sensory pathways in the brain, such as in the mammalian visual system. Feedforward connections from LGN terminate most densely in layer 4C of V1 and less densely in layer 6.corticogeniculate feedback arises from layer 6 neurons. Terminals from feedback cells comprise 30% of synaptic input to LGN relay neurons, compared to only 10% retinal input (Sillito et al. 2006). Layer 6 neurons also send excitatory input to layer 4, where LGN afferents contact V1. Their synaptic input is about five times greater than from LGN afferents terminating in layer 4. Layer 6 is therefore thought to regulate the transfer of retinal input to the central visual pathway (Sillito et al. 2006).

Due to these feedback connections, the transfer of ascending input from the LGN is continuously influenced by previous patterns of activity. Briggs and Usrey identified a subclass of corticogeniculate neurons in layer 6 of V1 that receive direct, suprathreshold LGN input. These corticogeniculate neurons provide much faster feedback to the LGN than neurons lacking LGN input, indicating a fast transfer of visual signals from the periphery to the cortex and back to the LGN. Feedback from the cortical motion area MT/V5 to layer 6 of V1 influences early sensory processing in both V1 and LGN. Such dynamic 'top-down' processing is necessary for normal motion processing (Sillito et al. 2006). Feedforward and feedback pathways should therefore be viewed as a reciprocal circuit interconnecting the thalamus with higher processing areas in the brain.

Since there is a robust feedback from the cortex to the LGN, it would be of interest to study the integrity of V1 to LGN connections in albinism. Unlike neural tracers, which are unidirectional and follow individual axons, tractography is bidirectional. It follows bundles of axons and may cross synapses. Discrepancies between tractography and tracer data are often attributed to false positives in the tractography data, but could also represent true feedback projections (Calabrese et al. 2015). Bridge and colleagues used probabilistic tractography to investigate the connections between human

LGN and contralateral MT+/V5 in controls and blindsight subject GY, whose left V1 was destroyed. They also performed tractography in the opposite direction, from MT+/V5 to contralateral LGN. In controls, transcallosal pathways were not of significant strength and the number of samples reaching the target in either direction did not differ significantly. In GY, however, the lesion may affect how tracts pass through the corpus callosum. Indeed, reversing the direction of tractography yielded significantly different results. Since tractography depends on the size of the seed, this difference could also be attributed to the big difference in the size of the masks; 140 mm^3 (9 voxels) for LGN compared to 2500 mm^3 (140 voxels) for MT+/V5. Moreover, the researchers also investigated cortico-cortical connections between V1 as well as MT+/V5 via the splenium in the two hemispheres. Tracts were of nearly equivalent size when run from both hemispheres (2008), likely due to the identical size of the seed and target masks.

However, when investigating ipsilateral thalamo-cortical and cortico-thalamic connections, tractography results may be different due to the great difference in size of the seed. Hence, when seeding from V1, waytotal values are expected to be larger compared with those obtained by seeding from LGN due to an increased number of voxels in the seed mask. Also, the runs are expected to take longer due to a bigger seed size. Since tractography does not provide information about polarity and tracts are likely to contain feedforward and feedback connections, it is impossible to infer about the exact ratio of these connections. The results presented here show altered LGN to V1 connectivity in human albinism. V1 and its feedback projection are much larger in size than the LGN and its feedforward projection. Therefore, if the size of tracts generated in the opposite direction (V1 to LGN) differs from the size of tracts travelling in the forward direction (LGN to V1), altered feedback connectivity would be a possible explanation. However, such assumptions could currently only be verified using molecular techniques. Finally, it would also be of interest to study connections to higher processing areas in the albino visual system such as the prestriate cortex (V2) and extrastriate cortex (V3-5). Tractography will be run as described in 3.4.4-3.4.5, with the desired structures as the seed and target masks.

To further support the tractography results, and to establish a structure-function relationship in the brains of individuals with albinism, an fMRI experiment will also be of interest. Specifically, patterns of V1 activation in individuals with OCA1 (no melanin) and OCA2 (minimal melanin) should be investigated, to validate previous studies stating that pigmentation predicts the line of decussation. Hoffman and colleagues used fMRI to study the topographical mapping of input to V1 in human albinism. Stimulating the nasal retina resulted in similar activation of the contralateral hemisphere in both albinism and controls. Upon stimulation of the temporal retina, however, an abnormal activation of the contralateral hemisphere was observed in albinism, compared to the normal ipsilateral activation observed in healthy brains (2003). For the fMRI experiment, a visual stimulus will consist of a section of a contrast-reversing checkerboard. Monocular stimulation of each hemi-retina will be performed to compare activation patterns in individuals with OCA1 (no melanin) and OCA2 (minimal melanin). A control nystagmus group should be included if eye movement is greater than 1.5-3 degrees.

References

Akeo, K., Ebenstein, D.B. & Dorey, C.K., 1989. Dopa and oxygen inhibit proliferation of retinal pigment epithelial cells, fibroblasts and endothelial cells in vitro. *Experimental eye research*, 49(3), pp.335–346.

Andrews, T.J., Halpern, S.D. & Purves, D., 1997. Correlated size variations in human visual cortex, lateral geniculate nucleus, and optic tract. *The Journal of neuroscience*, 17(8), pp.2859–2868.

Anikster, Y. et al., 2001. Mutation of a new gene causes a unique form of Hermansky-Pudlak syndrome in a genetic isolate of central Puerto Rico. *Nature genetics*, 28(4), pp.376–80.

Asman, A.J. & Landman, B.A., 2013. Non-local statistical label fusion for multi-atlas segmentation. *Medical Image Analysis*, 29(6), pp.997–1003.

Balkema, G.W. & Dräger, U.C., 1990. Origins of uncrossed retinofugal projections in normal and hypopigmented mice. *Visual neuroscience*, 4(6), pp.595–604.

Bassi, L. et al., 2008. Probabilistic diffusion tractography of the optic radiations and visual function in preterm infants at term equivalent age. *Brain*, 131(2), pp.573–582.

Bedell, H.E. & Loshin, D.S., 1991. Interrelations Between Measures of Visual-Acuity and Parameters of Eye-Movement in Congenital Nystagmus. *Investigative Ophthalmology & Visual Science*, 32(2), pp.416–421.

Behrens, T.E.J. et al., 2003. Non-invasive mapping of connections between human thalamus and cortex using diffusion imaging. *Nature neuroscience*, 6(7), pp.750–757.

Borovansky, J. & Riley, P.A., 2011. *Melanins and Melanosomes: Biosynthesis, Structure, Physiological and Pathological Functions*, John Wiley & Sons.

Brenner, M. & Hearing, V.J., 2008. The protective role of melanin against UV damage in human skin. *Photochemistry and Photobiology*, 84(3), pp.539–549.

Bridge, H. et al., 2008. Changes in connectivity after visual cortical brain damage underlie altered visual function. *Brain*, 131(6), pp.1433–1444.

Brilliant, M.H., 2001. The mouse p (pink-eyed dilution) and human P genes, oculocutaneous albinism type 2 (OCA2), and melanosomal pH. *Pigment cell research*, 14(2), pp.86–93.

Burkhalter, a & Bernardo, K.L., 1989. Organization of corticocortical connections in human visual cortex. *Proceedings of the National Academy of Sciences of the United States of America*, 86(3), pp.1071–1075.

Cabin, R.J. & Mitchell, R.J., 2000. To Bonferonni or not to Bonferonni: When and how are the questions. *Bulletin of the Ecoloical Society of America*, 81(3), pp.246–248.

Chacko, L.W., 1948. the Laminar Pattern of the Lateral Geniculate Body in the Primates. *Journal of neurology, neurosurgery, and psychiatry*, 11(3), pp.211–224.
Charles, S.J. et al., 1992. Genetic counselling in X-linked ocular albinism: clinical features of the carrier state. *Eye (London, England)*, 6 (Pt 1), pp.75–79.
Chenaux, G. & Henkemeyer, M., 2011. projection. , 34(10), pp.1620–1633.
Coenen, V. a. et al., 2005. Diffusion-weighted imaging-guided resection of intracerebral lesions involving the optic radiation. *Neurosurgical Review*, 28(3), pp.188–195.
Conlee, J.W., Parks, T.N. & Creel, D.J., 1986. Reduced neuronal size and dendritic length in the medial superior olivary nucleus of albino rabbits. *Brain research*, 363(1), pp.28–37.
Cope, F.W., 1969. Nuclear magnetic resonance evidence using D2O for structured water in muscle and brain. *Biophysical journal*, 9(3), pp.303–319.
Cortese, K. et al., 2005. The ocular albinism type 1 (OA1) gene controls melanosome maturation and size. *Investigative Ophthalmology and Visual Science*, 46(12), pp.4358–4364.
Costin, G.-E. & Hearing, V.J., 2007. Human skin pigmentation: melanocytes modulate skin color in response to stress. *The FASEB journal : official publication of the Federation of American Societies for Experimental Biology*, 21(4), pp.976–994.
Creel, D., Conlee, J.W. & Parks, T.N., 1983. Auditory brainstem anomalies in albino cats. I. Evoked potential studies. *Brain research*, 260(1), pp.1–9.
Creel, D., Hendrickson, A.E. & Leventhal, A.G., 1982. Retinal Projections in Tyrosinase-Negative Albino Cats. *The Journal of Neuroscience*, 2(7), pp.907-911.
Cruz-Inigo, A.E., Ladizinski, B. & Sethi, A., 2011. Albinism in Africa: stigma, slaughter and awareness campaigns. *Dermatologic clinics*, 29(1), pp.79–87.
Damadian, R., 1971. Tumor detection by nuclear magnetic resonance. *Science (New York, N.Y.)*, 171(976), pp.1151–1153.
Dave-Odigie, C.P., 2010. Albino Killings in Tanzania: Implications for Security. *Peace Studies Journal*, 3(1), pp.68–75.
Descoteaux, M. et al., 2009. Deterministic and Probabilistic Tractography Based on Complex Fiber Orientation Distributions. *IEEE Transactions on Medical Imaging*, 28(2), pp.269–286.
DeSimone, K., Viviano, J.D. & Schneider, K. a., 2015. Population Receptive Field Estimation Reveals New Retinotopic Maps in Human Subcortex. *Journal of Neuroscience*, 35(27), pp.9836–9847.
Devlin, J.T. et al., 2006. Reliable identification of the auditory thalamus using multi-modal structural analyses. *NeuroImage*, 30(4), pp.1112–1120.
Donatien, P. & Jeffery, G., 2002. Correlation between rod photoreceptor numbers and levels of ocular pigmentation. *Investigative Ophthalmology and Visual Science*, 43(4), pp.1198–1203.

Dubis, A.M. et al., 2012. Evaluation of normal human foveal development using optical coherence tomography and histologic examination. *Archives of ophthalmology*, 130(10), pp.1291–300.
Duffy, D.L. et al., 2004. Interactive effects of MC1R and OCA2 on melanoma risk phenotypes. *Human Molecular Genetics*, 13(4), pp.447–461.
Ebeling, U. & Reulen, H.J., 1988. Neurosurgical topography of the optic radiation in the temporal lobe. *Acta neurochirurgica*, 92(1-4), pp.29–36.
Eden, G.F. et al., 1996. Abnormal processing of visual motion in dyslexia revealed by functional brain imaging. *Nature*, 382(6586), pp.66–69.
Erskine, L. & Herrera, E., 2014. Connecting the Retina to the Brain. *ASN Neuro*, 6(6), pp.1–26.
Esteve, J.V. & Jeffery, G., 1998. Reduced retinal deficits in an albino mammal with a cone rich retina: A study of the ganglion cell layer at the area centralis of pigmented and albino grey squirrels. *Vision Research*, 38(6), pp.937–940.
Farahibozorg, S., Hashemi-Golpayegani, S.M. & Ashburner, J., 2013. Age- and Sex-Related Variations in the Brain White Matter Fractal Dimension Throughout Adulthood: An MRI Study. *Clinical Neuroradiology*, pp.1–14.
Fischl, B., 2012. FreeSurfer. *NeuroImage*, 62(2), pp.774–781.
Fujisawa, H. et al., 1976. A decay of gap junctions in association with cell differentiation of neural retina in chick embryonic development. *Journal of cell science*, 22(3), pp.585–596.
Fujita, N. et al., 2001. Lateral Geniculate Nucleus: Anatomic and Functional Identi cation by Use of MR Imaging. American Journal of Neuroradiology. 22, pp.1719–1726.

Fukuda, Y. et al., 1989. Nasotemporal overlap of crossed and uncrossed retinal ganglion cell projections in the Japanese monkey (Macaca fuscata). *The Journal of neuroscience*, 9(7), pp.2353–2373.
Fulton, A.B., 1978. Human Albinism. *Archives of Ophthalmology*, 96(2), p.305.
Galantucci, S. et al., 2011. White matter damage in primary progressive aphasias: A diffusion tensor tractography study. *Brain*, 134(10), pp.3011–3029.
Ge, Y. et al., 2002. Age-related total gray matter and white matter changes in normal adult brain. Part I: volumetric MR imaging analysis. *AJNR. American journal of neuroradiology*, 23(8), pp.1327–1333.
Van Genderen, M.M. et al., 2006. Chiasmal misrouting and foveal hypoplasia without albinism. *The British journal of ophthalmology*, 90(9), pp.1098–1102.
Gershoni-Baruch, R. et al., 1991. Dopa reaction test in hair bulbs of fetuses and its application to the prenatal diagnosis of albinism. *Journal of the American Academy of Dermatology*, 24(2 Pt 1), pp.220–2.
Giraldo-Chica, M., Hegarty, J.P. & Schneider, K. a., 2015. Morphological differences in the lateral geniculate nucleus associated with dyslexia. *NeuroImage: Clinical*, 7, pp.830–836.

Gittler, J.K. & Marion, R., 2014. More than skin deep : Genetics , clinical manifestations , and diagnosis of albinism. *European Journal of Business and Management*, pp.1–12.
Godement, P., Wang, L.C. & Mason, C. a, 1994. Retinal axon divergence in the optic chiasm: dynamics of growth cone behavior at the midline. *The Journal of neuroscience,* 14, pp.7024–7039.
Gottlob, I., 2007. Albinism: a model of adaptation of the brain in congenital visual disorders. *The British journal of ophthalmology*, 91(4), pp.411–412.
Guillery, R.W. et al., 1984. Abnormal central visual pathways in the brain of an albino green monkey (Cercopithecus aethiops). *The Journal of comparative neurology*, 226(2), pp.165–183.
Guillery, R.W., Okoro, a. N. & Witkop, C.J., 1975. Abnormal visual pathways in the brain of a human albino. *Brain Research*, 96(2), pp.373–377.
Von Dem Hagen, E. a H. et al., 2007. Pigmentation predicts the shift in the line of decussation in humans with albinism. *European Journal of Neuroscience*, 25(2), pp.503–511.
Von dem Hagen, E.A.H. et al., 2005. Retinal abnormalities in human albinism translate into a reduction of grey matter in the occipital cortex. *The European journal of neuroscience*, 22(10), pp.2475–80.
Halder, R.M. & Bridgeman-Shah, S., 1995. Skin cancer in African Americans. *Cancer*, 75(2 Suppl), pp.667–73.
Hampson, E.C., Vaney, D.I. & Weiler, R., 1992. Dopaminergic modulation of gap junction permeability between amacrine cells in mammalian retina. *The Journal of neuroscience : the official journal of the Society for Neuroscience*, 12(12), pp.4911–4922.
Hawkes, J.E. et al., 2013. Report of a novel OCA2 gene mutation and an investigation of OCA2 variants on melanoma risk in a familial melanoma pedigree. *Journal of Dermatological Science*, 69(1), pp.30–37.
Hendrickson, a, 1992. A morphological comparison of foveal development in man and monkey. *Eye*, 6 (Pt 2), pp.136–144.
Hendrickson, A.E. & Yuodelis, C., 1984. The morphological development of the human fovea. *Ophthalmology*, 91(6), pp.603–12.
Herbin, M. et al., 1999. Transneuronal degeneration of retinal ganglion cells in early hemispherectomized monkeys. *Neuroreport*, 10(7), pp.1447–1452.
Herrera, E. et al., 2003. Zic2 patterns binocular vision by specifying the uncrossed retinal projection. *Cell*, 114(5), pp.545–557.
Hickey, T.L. & Guillery, R.W., 1979. Variability of laminar patterns in the human lateral geniculate nucleus. *The Journal of comparative neurology*, 183(2), pp.221–46.
Hitchcock, P.F. & Hickey, T.L., 1980. Prenatal development of the human lateral geniculate nucleus. *The Journal of comparative neurology*, 194(2), pp.395–411.

Hofer, S. & Frahm, J., 2008. In Vivo Mapping of Fiber Pathways in the Rhesus Monkey Brain. *The Open Medical Imaging Journal*, 2(1), pp.32–41.
Hofer, S., Karaus, A. & Frahm, J., 2010. Reconstruction and dissection of the entire human visual pathway using diffusion tensor MRI. *Frontiers in neuroanatomy*, 4, p.1-7.
Hoffmann, M.B. et al., 2005. Misrouting of the optic nerves in albinism: Estimation of the extent with visual evoked potentials. *Investigative Ophthalmology and Visual Science*, 46(10), pp.3892–3898.
Hoffmann, M.B. et al., 2003. Organization of the visual cortex in human albinism. *The Journal of neuroscience*, 23(26), pp.8921–8930.
Hoffmann, M.B. et al., 2012. Plasticity and Stability of the Visual System in Human Achiasma. *Neuron*, 75(3), pp.393–401.
Horton, J.C. & Hocking, D.R., 1996. Anatomical demonstration of ocular dominance columns in striate cortex of the squirrel monkey. *The Journal of neuroscience*, 16(17), pp.5510–5522.
Huberman, A.D., Feller, M.B. & Chapman, B., 2008. Mechanisms Underlying Development of Visual Maps and Receptive Fields. *Annual Review of Neuroscience* , 31, pp.479–509.
Ilia, M. & Jeffery, G., 1999. Retinal Mitosis is Regulated by Dopa, a Melanin Precursor That May Influence the Time at Which Cells Exit the Cell Cycle: Analysis of Patterns of Cell Production in Pigmented and Albino Retinae. *Journal of Comparitive Nuerology*, 405(3), pp.394-405.
Inagaki, K. et al., 2004. Oculocutaneous albinism type 4 is one of the most common types of albinism in Japan. *American journal of human genetics*, 74(3), pp.466–471.
Introne, W., Boissy, R.E. & Gahl, W. a, 1999. Clinical, molecular, and cell biological aspects of Chediak-Higashi syndrome. *Molecular genetics and metabolism*, 68(2), pp.283–303.
Iwata, F. et al., 2000. Correlation of visual acuity and ocular pigmentation with the 16-bp duplication in the HPS-1 gene of Hermansky-Pudlak syndrome, a form of albinism. *Ophthalmology*, 107(4), pp.783–9.
Jannot, A.-S. et al., 2005. Allele variations in the OCA2 gene (pink-eyed-dilution locus) are associated with genetic susceptibility to melanoma. *European journal of human genetics : EJHG*, 13(8), pp.913–920.
Jeffery, G., 2001. Architecture of the optic chiasm and the mechanisms that sculpt its development. *Physiological reviews*, 81(4), pp.1393–1414.
Jeffery, G., 1997. The albino retina: An abnormality that provides insight into normal retinal development. *Trends in Neurosciences*, 20(4), pp.165–169.
Jeffery, G., Cowey, A. & Kuypers, H.G., 1981. Bifurcating retinal ganglion cell axons in the rat, demonstrated by retrograde double labelling. *Experimental brain research*, 44(1), pp.34–40.

Jeffery, G., Darling, K. & Whitmore, a, 1994. Melanin and the regulation of mammalian photoreceptor topography. *The European journal of neuroscience*, 6(4), pp.657–667.
Jeffery, G. & Erskine, L., 2005. Variations in the architecture and development of the vertebrate optic chiasm. *Progress in Retinal and Eye Research*, 24(6), pp.721–753.
Jiang, H. et al., 2006. DtiStudio: Resource program for diffusion tensor computation and fiber bundle tracking. *Computer Methods and Programs in Biomedicine*, 81(2), pp.106–116.
Jones, D.K., Knösche, T.R. & Turner, R., 2013. White matter integrity, fiber count, and other fallacies: The do's and don'ts of diffusion MRI. *NeuroImage*, 73, pp.239–254.
Kaiser, P.K., 2009. Prospective evaluation of visual acuity assessment: a comparison of snellen versus ETDRS charts in clinical practice (An AOS Thesis). *Transactions of the American Ophthalmological Society*, 107, pp.311–324.
King, R. a et al., 2003. MC1R mutations modify the classic phenotype of oculocutaneous albinism type 2 (OCA2). *American journal of human genetics*, 73(3), pp.638–645.
King, R. a. et al., 2003. Tyrosinase gene mutations in oculocutaneous albinism 1 (OCA1): Definition of the phenotype. *Human Genetics*, 113(6), pp.502–513.
Kitajima, M. et al., 1996. MR signal intensity of the optic radiation. *American Journal of Neuroradiology*, 17(7), pp.1379–1383.
Kromberg, J.G. et al., 1990. Red or rufous albinism in southern Africa. *Ophthalmic paediatrics and genetics*, 11(3), pp.229–35.
Kromberg, J.G. & Jenkins, T., 1982. Prevalence of albinism in the South African negro. *South African medical journal = Suid-Afrikaanse tydskrif vir geneeskunde*, 61(11), pp.383–386.
Kupfer, C., 1965. The laminar pattern and distribution of cell size in the lateral geniculate nucleus of man. *Journal of neuropathology and experimental neurology*, 24(4), pp.645–52.
Kupfer, C., Chumbley, L. & Downer, J.C., 1967. Quantitative histology of optic nerve, optic tract and lateral geniculate nucleus of man. *Journal of anatomy*, 101(Pt 3), pp.393–401.
Laemle, L.K., Strominger, N.L. & Carpenter, D.O., 2006. Cross-modal innervation of primary visual cortex by auditory fibers in congenitally anophthalmic mice. *Neuroscience Letters*, 396(2), pp.108–112.
Laird, D.W., 2005. Connexin phosphorylation as a regulatory event linked to gap junction channel assembly. *Biochimica et Biophysica Acta - Biomembranes*, 1711(2 SPEC. ISS.), pp.154–163.
Li, M. et al., 2012. Quantification of the human lateral geniculate nucleus in vivo using MR imaging based on morphometry: volume loss with age. *AJNR. American journal of neuroradiology*, 33(5), pp.915–21.

Livingstone, M.S. et al., 1991. Physiological and anatomical evidence for a magnocellular defect in developmental dyslexia. *Proceedings of the National Academy of Sciences of the United States of America*, 88(18), pp.7943–7947.
Lund, P.M. et al., 2007. Oculocutaneous albinism in a rural community of South Africa: a population genetic study. *Annals of human biology*, 34(4), pp.493–497.
Malik, R., Swanson, W.H. & Garway-Heath, D.F., 2012. The "structure-function" relationship in glaucoma- past thinking and current concepts. *Clinical & Experimental Ophthalmology*, 40(4), pp.369-380.
Del Marmol, V. & Beermann, F., 1996. Tyrosinase and related proteins in mammalian pigmentation. *FEBS Letters*, 381(3), pp.165–168.
Mártinez-García, M. & Montoliu, L., 2013. Albinism in Europe. *Journal of Dermatology*, 40(5), pp.319–324.
Mason, C. a, Marcus, R.C. & Wang, L.C., 1996. Retinal axon divergence in the optic chiasm: growth cone behaviors and signalling cells. *Progress in brain research*, 108, pp.95–107.
Mcketton, L., Kelly, K.R. & Schneider, K. a., 2014. Abnormal lateral geniculate nucleus and optic chiasm in human albinism. *Journal of Comparative Neurology*, 522(11), pp.2680–2687.
Meissirel, C. et al., 1997. Early divergence of magnocellular and parvocellular functional subsystems in the embryonic primate visual system. *Proceedings of the National Academy of Sciences of the United States of America*, 94(11), pp.5900–5905.
Meyer, C.H., Lapolice, D.J. & Freedman, S.F., 2002. Foveal Hypoplasia in Oculocutaneous Coherence Tomography. *American Journal of Ophthalmology*, 133(3), pp.409–410.
Moore, D.R. & Kowalchuk, N.E., 1988. An anomaly in the auditory brain stem projections of hypopigmented ferrets. *Hearing research*, 35(2-3), pp.275–8.
Mufson, E.J., Brady, D.R. & Kordower, J.H., 1990. Tracing neuronal connections in postmortem human hippocampal complex with the carbocyanine dye DiI. *Neurobiology of Aging*, 11(6), pp.649–653.
Murillo-Cuesta, S. et al., 2010. Melanin precursors prevent premature age-related and noise-induced hearing loss in albino mice. *Pigment Cell and Melanoma Research*, 23(1), pp.72–83.
Nakagawa, S. et al., 2000. Ephrin-B regulates the Ipsilateral routing of retinal axons at the optic chiasm. *Neuron*, 25(3), pp.599–610.
Neveu, M.M. et al., 2005. Optic chiasm formation in humans is independent of foveal development. *European Journal of Neuroscience*, 22(7), pp.1825–1829.
Newcombe, V.F.J., Das, T. & Cross, J.J., 2013. Diffusion imaging in neurological disease. *Journal of Neurology*, 260(1), pp.335–342.

Newton, J.M. et al., 2001. Mutations in the human orthologue of the mouse underwhite gene (uw) underlie a new form of oculocutaneous albinism, OCA4. *American journal of human genetics*, 69(5), pp.981–988.
Nga Tran, T., 2009. controversies. , 21(5), pp.509–516.
Oetting, W.S., 2002. New insights into ocular albinism type 1 (OA1): Mutations and polymorphisms of the OA1 gene. *Human Mutation*, 19(2), pp.85–92.
Oetting, W.S. & King, R. a, 1994. Molecular basis of oculocutaneous albinism. *The Journal of investigative dermatology*, 103(5 Suppl), p.131S–136S.
Okulicz, J.F. et al., 2003. Oculocutaneous albinism. *Journal of the European Academy of Dermatology and Venereology : JEADV*, 17(3), pp.251–256.
Palumbo, a et al., 1991. Comparative action of dopachrome tautomerase and metal ions on the rearrangement of dopachrome. *Biochimica et biophysica acta*, 1115(1), pp.1–5.
Papageorgiou, E., McLean, R.J. & Gottlob, I., 2014. Nystagmus in Childhood. *Pediatrics and Neonatology*, 55(5), pp.341–351.
Pearson, R. a. et al., 2004. Ca2+ signalling and gap junction coupling within and between pigment epithelium and neural retina in the developing chick. *European Journal of Neuroscience*, 19(9), pp.2435–2445.
Piatigorsky, J. & Kozmik, Z., 2004. Cubozoan jellyfish: An evo/devo model for eyes and other sensory systems. *International Journal of Developmental Biology*, 48(8-9), pp.719–729.
Picaud, S., Wunderer, H. & Franceschini, N., 1990. Dye-induced photopermeabilization and photodegeneration: a lesion technique useful for neuronal tracing. *Journal of neuroscience methods*, 33(2-3), pp.101–12.
Purves, D. et al., 2001. The Retinotopic Representation of the Visual Field.
Rasband, K., Hardy, M. & Chien, C.B., 2003. Generating X: Formation of the optic chiasm. *Neuron*, 39(6), pp.885–888.
Rebsam, A., Bhansali, P. & Mason, C.A., 2012. Eye-specific projections retinogeniculate axons are altered in albino mice. *The Journal of neuroscience*, 32(14), pp.4821–4826.
Reese, B.E., 1988. "Hidden lamination" in the dorsal lateral geniculate nucleus: the functional organization of this thalamic region in the rat. *Brain research*, 472(2), pp.119–37.
Rice, D.S., Williams, R.W. & Goldowitz, D., 1995. Genetic control of retinal projections in inbred strains of albino mice. *The Journal of comparative neurology*, 354(3), pp.459–69.
Schmitz, B. et al., 2003. Configuration of the optic chiasm in humans with albinism as revealed by magnetic resonance imaging. *Investigative ophthalmology & visual science*, 44(1), pp.16–21.
Schneider, K. a, Richter, M.C. & Kastner, S., 2004. Retinotopic organization and functional subdivisions of the human lateral geniculate nucleus: a high-resolution functional magnetic resonance imaging study. *The Journal of neuroscience*, 24(41), pp.8975–8985.

Schnur, R.E. et al., 1998. OA1 mutations and deletions in X-linked ocular albinism. *American journal of human genetics*, 62(4), pp.800–809.
Schwartz SH. 2010.Visual perception: a clinical orientation. In: Morita J and Boyle PJ, editors. Introductory concepts.4th ed. US: p.3-19.
Serrant, M.T. et al., 2010. NIH Public Access. *Changes*, 29(6), pp.448–453.
Shen, B., Rosenberg, B. & Orlow, S.J., 2001. Intracellular distribution and late endosomal effects of the ocular albinism type 1 gene product: consequences of disease-causing mutations and implications for melanosome biogenesis. *Traffic (Copenhagen, Denmark)*, 2(3), pp.202–211.
Sherbondy, A.J. et al., 2008. Identifying the human optic radiation using diffusion imaging and fiber tractography. *Journal of Vision*, 8(10), pp.1–11.
Sherbondy, A.J., Dougherty, R.F. & Wandell, B. a, 2008. ConTrack: Finding the most likely pathways between brain regions using diffusion tractography. *Journal of Vision*, 8(9), pp.1–30.
Smith, S.M. et al., 2004. Advances in functional and structural MR image analysis and implementation as FSL. *NeuroImage*, 23(SUPPL. 1), pp.208–219.
Smith, S.M. et al., 2006. Tract-based spatial statistics: Voxelwise analysis of multi-subject diffusion data. *NeuroImage*, 31(4), pp.1487–1505.
Spear, P.D. et al., 1996. Relationship between numbers of retinal ganglion cells and lateral geniculate neurons in the rhesus monkey. *Visual neuroscience*, 13(1), pp.199–203.
Spielmann, a, 2000. Clinical rationale for manifest congenital nystagmus surgery. *Journal of AAPOS :American Association for Pediatric Ophthalmology and Strabismus*, 4(2), pp.67–74.
Spritz, R. a. et al., 1997. Novel mutations of the tyrosinase (TYR) gene in type I oculocutaneous albinism (OCA1). *Human Mutation*, 10(2), pp.171–174.
Stein, J.F., 1994. Developmental dyslexia, neural timing and hemispheric lateralisation. *International journal of psychophysiology : official journal of the International Organization of Psychophysiology*, 18(3), pp.241–9.
Steinbrink, C. et al., 2008. The contribution of white and gray matter differences to developmental dyslexia: Insights from DTI and VBM at 3.0 T. *Neuropsychologia*, 46(13), pp.3170–3178.
Summers, C.G., 2009. Albinism : Classification , Clinical Characteristics, and recent findings. *Optometry and Vision Science*, 86(6), pp.659–662.
Summers, C.G., 1996. Vision in albinism. *Transactions of the American Ophthalmological Society*, 94, pp.1095–1155.
Suzuki, T. & Hayashi, M., 2011. Oculocutaneous Albinism Type 4. *GeneReviews*.
Thaler, L., Arnott, S.R. & Goodale, M. a., 2011. Neural correlates of natural human echolocation in early and late blind echolocation experts. *PLoS ONE*, 6(5).

Tian, L. et al., 2011. Hemisphere- and gender-related differences in small-world brain networks: A resting-state functional MRI study. *NeuroImage*, 54(1), pp.191–202.
Toyofuku, K. et al., 2001. The molecular basis of oculocutaneous albinism type 1 (OCA1): sorting failure and degradation of mutant tyrosinases results in a lack of pigmentation. *The Biochemical journal*, 355(Pt 2), pp.259–269.
Vandermosten, M. et al., 2012. A qualitative and quantitative review of diffusion tensor imaging studies in reading and dyslexia. *Neuroscience and Biobehavioral Reviews*, 36(6), pp.1532–1552.
Victor, J.D. et al., 2000. Visual function and brain organization in non-decussating retinal-fugal fibre syndrome. *Cerebral cortex (New York, N.Y. : 1991)*, 10(1), pp.2–22.
Wang, L.C. et al., 1995. Crossed and uncrossed retinal axons respond differently to cells of the optic chiasm midline in vitro. *Neuron*, 15(6), pp.1349–1364.
Wedeen, V.J. et al., 2008. Diffusion spectrum magnetic resonance imaging (DSI) tractography of crossing fibers. *NeuroImage*, 41(4), pp.1267–1277.
Weiner, I.B. 2003. Visual processing in the Primate Brain. Handbook of Psychology, Biological Psychology. New Jersey: Wiley&Sons Inc. pp. 143-146.
Westbroek, W. et al., 2007. Cellular defects in Chediak-Higashi syndrome correlate with the molecular genotype and clinical phenotype. *The Journal of investigative dermatology*, 127(11), pp.2674–2677.
Wick, M.M., 1980. Levodopa and Dopamine Analogs as DMA Polymerase Inhibitors and Antitumor Agents in Human Melanoma1. *Cancer Research*, 40(5), pp.1414–1418.
Wiesel, T.N. & Hubel, D.H., 1966. Spatial and chromatic interactions in the lateral geniculate body of the rhesus monkey. *Journal of neurophysiology*, 29(6), pp.1115–1156.
Williams, D.S. et al., 2010. Harmonin in the Murine Retina and the Retinal Phenotypes of Ush1c-Mutant Mice and human USH1C. *Investigative Ophthalmology and Visual Scien*e, 50(8), pp.3881-3889.
Williams, R.W., Hogan, D. & Garraghty, P.E., 1994. Target recognition and visual maps in the thalamus of achiasmatic dogs. *Nature*, 367(6464), pp.637–639.
Wilson, H.R. et al., 1988. Albino spatial vision as an instance of arrested visual development. *Vision research*, 28(9), pp.979–90.
WOLFF, D., 1931. MELANIN IN THE INNER EAR. *Archives of Otolaryngology - Head and Neck Surgery*, 14(2), pp.195–211.
Yeh, F.C. et al., 2013. Deterministic diffusion fiber tracking improved by quantitative anisotropy. *PLoS ONE*, 8(11), pp.1–16.
Young, R.W., 1985. Cell differentiation in the retina of the mouse. *The Anatomical Record*, 205, pp.199–205.

Yücel, Y.H. et al., 2001. Atrophy of relay neurons in magno- and parvocellular layers in the lateral geniculate nucleus in experimental glaucoma. *Investigative Ophthalmology and Visual Science*, 42(13), pp.3216–3222.
Zhang, K. et al., 2011. Oculocutaneous Albinism Type 3 (OCA3): Analysis of Two Novel Mutations in TYRP1 Gene in Two Chinese Patients. *Cell Biochemistry and Biophysics*, 61(3), pp.523–529.
Zhang, L. et al., 2007. Quantifying degeneration of white matter in normal aging using fractal dimension. *Neurobiology of Aging*, 28(10), pp.1543–1555.

Appendices

Appendix A: **Non-normalized Probabilistic Runs**

Table A1: SPSS GENLIN "long form" data view for T1 run. Group: 2=albinism, 1=controls; hemisphere: 2=left, 1=right; gender: 2=male, 1=female.

Subjectid	Group	Hemisphere	Gender	Age	LGN_vol	LGN2V1
1.00	2.00	2.00	2.00	48.00	57.00	359.00
1.00	2.00	1.00	2.00	48.00	78.00	944.00
3.00	2.00	2.00	2.00	20.00	199.00	4653.00
3.00	2.00	1.00	2.00	20.00	179.00	2389.00
4.00	2.00	2.00	2.00	21.00	202.57	13927.00
4.00	2.00	1.00	2.00	21.00	186.45	14154.00
5.00	2.00	2.00	2.00	48.00	131.90	313.00
5.00	2.00	1.00	2.00	48.00	109.77	45.00
6.00	2.00	2.00	1.00	43.00	101.00	27986.00
6.00	2.00	1.00	1.00	43.00	106.00	21009.00
7.00	2.00	2.00	2.00	56.00	75.00	2966.00
7.00	2.00	1.00	2.00	56.00	75.00	319.00
8.00	2.00	2.00	1.00	22.00	101.00	1044.00
8.00	2.00	1.00	1.00	22.00	95.00	1564.00
9.00	2.00	2.00	1.00	47.00	54.00	696.00
9.00	2.00	1.00	1.00	47.00	56.00	2562.00
10.00	2.00	2.00	1.00	45.00	81.00	5181.00
10.00	2.00	1.00	1.00	45.00	104.00	5252.00
11.00	2.00	2.00	1.00	17.00	115.00	15541.00
11.00	2.00	1.00	1.00	17.00	117.00	38313.00
12.00	2.00	2.00	1.00	29.00	70.00	606.00
12.00	2.00	1.00	1.00	29.00	93.00	82.00
105.00	1.00	2.00	1.00	24.00	217.00	5298.00
105.00	1.00	1.00	1.00	24.00	240.00	29236.00
106.00	1.00	2.00	2.00	22.00	126.00	3308.00
106.00	1.00	1.00	2.00	22.00	131.00	1589.00
107.00	1.00	2.00	2.00	25.00	204.00	11760.00
107.00	1.00	1.00	2.00	25.00	212.00	5573.00
108.00	1.00	2.00	1.00	24.00	140.00	818.00
108.00	1.00	1.00	1.00	24.00	112.00	3354.00
109.00	1.00	2.00	1.00	20.00	281.00	31618.00
109.00	1.00	1.00	1.00	20.00	247.00	5232.00
111.00	1.00	2.00	2.00	39.00	203.00	54798.00
111.00	1.00	1.00	2.00	39.00	230.00	30794.00
112.00	1.00	2.00	1.00	26.00	199.00	1213.00
112.00	1.00	1.00	1.00	26.00	209.00	18253.00
113.00	1.00	2.00	1.00	42.00	213.00	38345.00
113.00	1.00	1.00	1.00	42.00	125.00	6621.00
114.00	1.00	2.00	1.00	41.00	224.00	11885.00
114.00	1.00	1.00	1.00	41.00	256.00	35201.00
115.00	1.00	2.00	2.00	60.00	190.00	2583.00
115.00	1.00	1.00	2.00	60.00	152.00	3317.00

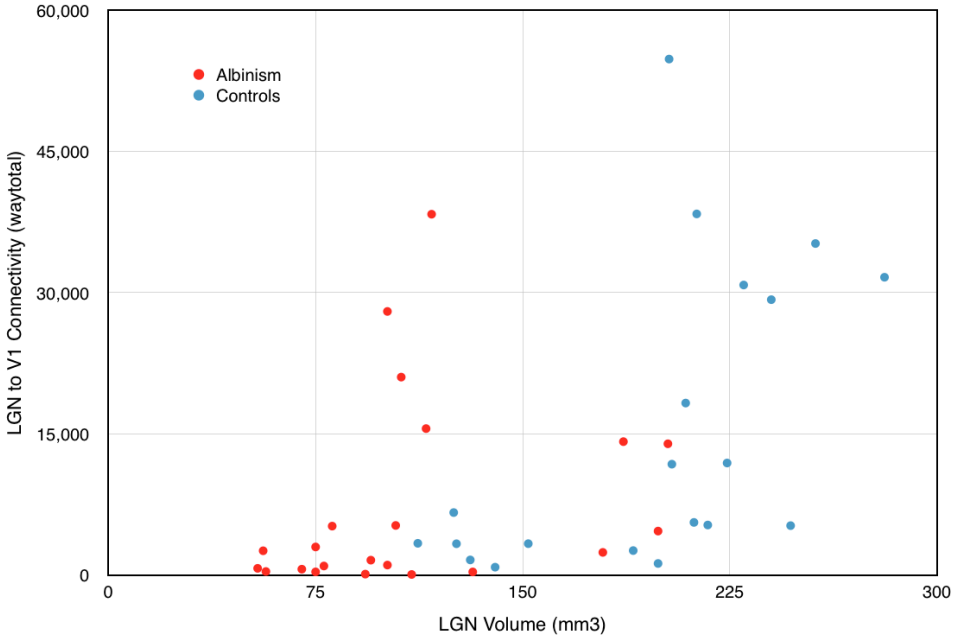

Figure A1: LGN volume (mm³) vs. LGN to V1 connectivity (waytotal), T1 space. ProbtrackX for probabilistic tracking was run in DTI space with seed (LGN) and target (V1) masks in T1 space.

Table A2: SPSS GLM (general linear model) "wide form" data view for FS run (note: analysis was run using GENLIN).

SubjID	Group	Gender	Age	LLGN_vol	RLGN_vol	LLGN2V1	RLGN2V1
101.00	2.00	2.00	48.00	49.00	67.00	248.00	397.00
103.00	2.00	2.00	20.00	212.00	190.00	2558.00	780.00
104.00	2.00	2.00	21.00	194.00	184.00	18765.00	17820.00
105.00	2.00	2.00	48.00	129.00	113.00	140.00	37.00
106.00	2.00	1.00	43.00	135.00	153.00	38703.00	20870.00
107.00	2.00	2.00	56.00	84.00	85.00	2141.00	831.00
108.00	2.00	1.00	22.00	117.00	114.00	1173.00	1641.00
109.00	2.00	1.00	47.00	79.00	40.00	2892.00	2712.00
110.00	2.00	1.00	45.00	76.00	112.00	7786.00	15342.00
111.00	2.00	1.00	17.00	156.00	156.00	23862.00	41985.00
112.00	2.00	1.00	29.00	75.00	98.00	607.00	131.00
205.00	1.00	1.00	24.00	205.00	250.00	11310.00	22739.00
206.00	1.00	2.00	22.00	112.00	115.00	27288.00	1529.00
207.00	1.00	2.00	25.00	186.00	199.00	54942.00	14314.00
208.00	1.00	1.00	24.00	166.00	121.00	16261.00	4355.00
209.00	1.00	1.00	20.00	292.00	243.00	15582.00	22047.00
211.00	1.00	2.00	39.00	191.00	193.00	697.00	2135.00
212.00	1.00	1.00	26.00	206.00	235.00	20222.00	80670.00
213.00	1.00	1.00	42.00	209.00	136.00	16251.00	8496.00
214.00	1.00	1.00	41.00	224.00	256.00	30930.00	43480.00
215.00	1.00	2.00	60.00	211.00	158.00	24569.00	23533.00

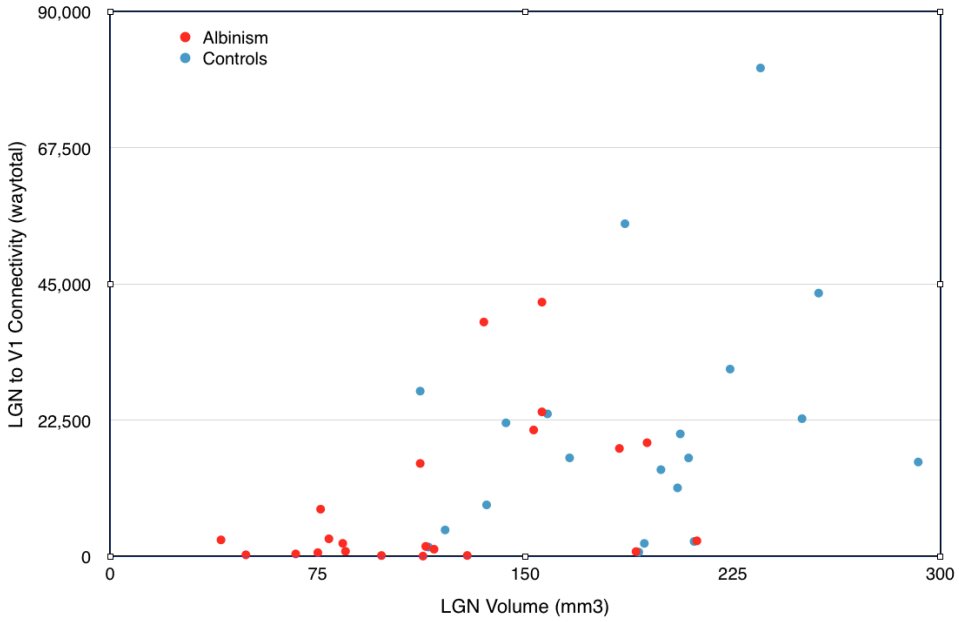

Figure A2: LGN volume (mm³) vs. LGN to V1 connectivity (waytotal), FS space. ProbtrackX for probabilistic tracking was run in DTI space with seed (LGN) and target (V1) masks in FS space.

Table A3: SPSS GENLIN"long form" data view for FS run with all-raters-median LGN masks

SubjectID	Group	Hemisphere	Gender	Age	Waytotal
1.00	2.00	2.00	2.00	48.00	3150.00
1.00	2.00	1.00	2.00	48.00	789.00
3.00	2.00	2.00	2.00	20.00	1599.00
3.00	2.00	1.00	2.00	20.00	861.00
4.00	2.00	2.00	2.00	21.00	13796.00
4.00	2.00	1.00	2.00	21.00	19272.00
5.00	2.00	2.00	2.00	48.00	158.00
5.00	2.00	1.00	2.00	48.00	46.00
6.00	2.00	2.00	1.00	43.00	38703.00
6.00	2.00	1.00	1.00	43.00	20870.00
7.00	2.00	2.00	2.00	56.00	1223.00
7.00	2.00	1.00	2.00	56.00	997.00
8.00	2.00	2.00	1.00	22.00	2143.00
8.00	2.00	1.00	1.00	22.00	1822.00
9.00	2.00	2.00	1.00	47.00	3463.00
9.00	2.00	1.00	1.00	47.00	3141.00
10.00	2.00	2.00	1.00	45.00	23486.00
10.00	2.00	1.00	1.00	45.00	14819.00
11.00	2.00	2.00	1.00	17.00	26629.00
11.00	2.00	1.00	1.00	17.00	40083.00
12.00	2.00	2.00	1.00	29.00	698.00
12.00	2.00	1.00	1.00	29.00	111.00
105.00	1.00	2.00	1.00	24.00	8163.00
105.00	1.00	1.00	1.00	24.00	13668.00
106.00	1.00	2.00	2.00	22.00	25225.00
106.00	1.00	1.00	2.00	22.00	1589.00
107.00	1.00	2.00	2.00	25.00	46916.00
107.00	1.00	1.00	2.00	25.00	14413.00
108.00	1.00	2.00	1.00	24.00	13316.00
108.00	1.00	1.00	1.00	24.00	3204.00
109.00	1.00	2.00	1.00	20.00	6840.00
109.00	1.00	1.00	1.00	20.00	21037.00
111.00	1.00	2.00	2.00	39.00	20774.00
111.00	1.00	1.00	2.00	39.00	20397.00
112.00	1.00	2.00	1.00	26.00	13974.00
112.00	1.00	1.00	1.00	26.00	67600.00
113.00	1.00	2.00	1.00	42.00	16251.00
113.00	1.00	1.00	1.00	42.00	8496.00
114.00	1.00	2.00	1.00	41.00	31067.00
114.00	1.00	1.00	1.00	41.00	35658.00
115.00	1.00	2.00	2.00	60.00	18833.00
115.00	1.00	1.00	2.00	60.00	20783.00

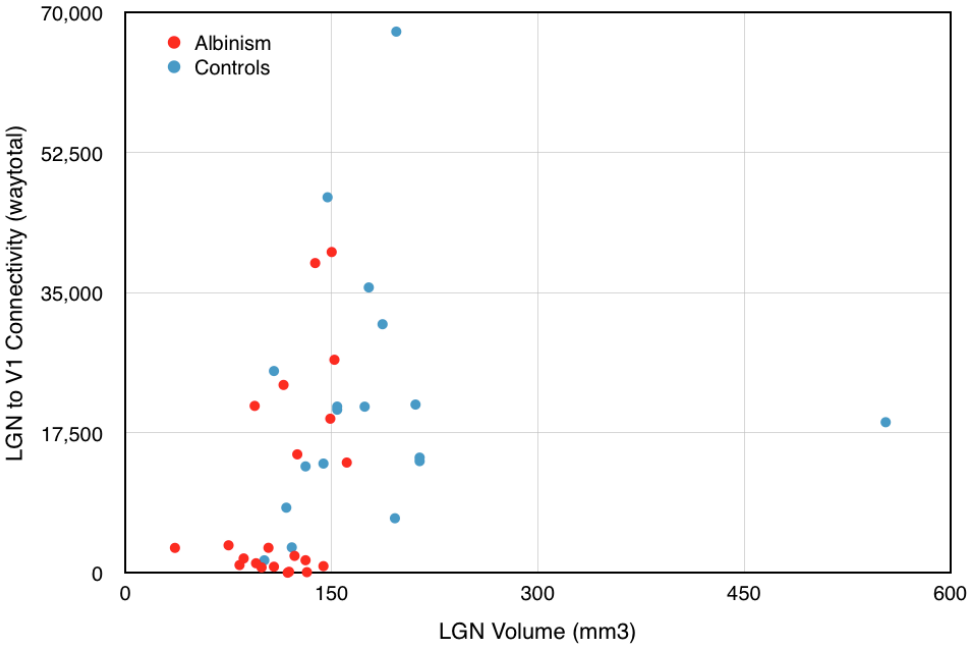

Figure A3: LGN volume (mm³) vs. LGN to V1 connectivity (waytotal), FS space. ProbtrackX for probabilistic tracking was run in DTI space with seed (all-raters-median LGN) and target (V1) masks in FS space.

Appendix B: **Non-normalizaed Deterministic Run**

Table B1: SPSS GENLIN "long form" data view for deterministic run in diffusion space. Group: 1=albinism, 2=controls; hemisphere: 2=left, 1=right; gender: 2=male, 1=female.

SubjectID	Group	Hemisphere	Gender	Age	LGN_vol	numb_tracts
1.00	1.00	2.00	2.00	48.00	63.00	2359.00
1.00	1.00	1.00	2.00	48.00	72.00	1365.00
3.00	1.00	2.00	2.00	20.00	193.50	4005.00
3.00	1.00	1.00	2.00	20.00	162.00	3022.00
4.00	1.00	2.00	2.00	21.00	180.00	3213.00
4.00	1.00	1.00	2.00	21.00	171.00	3764.00
5.00	1.00	2.00	2.00	48.00	121.50	3855.00
5.00	1.00	1.00	2.00	48.00	121.50	2707.00
6.00	1.00	2.00	1.00	43.00	153.00	2974.00
6.00	1.00	1.00	1.00	43.00	112.50	1948.00
7.00	1.00	2.00	2.00	56.00	85.50	2209.00
7.00	1.00	1.00	2.00	56.00	103.50	3763.00
8.00	1.00	2.00	1.00	22.00	117.00	2729.00
8.00	1.00	1.00	1.00	22.00	112.50	4482.00
9.00	1.00	2.00	1.00	47.00	45.00	3780.00
9.00	1.00	1.00	1.00	47.00	31.50	4832.00
10.00	1.00	2.00	1.00	45.00	76.50	4094.00
10.00	1.00	1.00	1.00	45.00	112.50	3913.00
11.00	1.00	2.00	1.00	17.00	130.50	4279.00
11.00	1.00	1.00	1.00	17.00	126.00	4002.00
12.00	1.00	2.00	1.00	29.00	81.00	3735.00
12.00	1.00	1.00	1.00	29.00	112.50	3840.00
105.00	2.00	2.00	1.00	24.00	198.00	2514.00
105.00	2.00	1.00	1.00	24.00	297.00	2492.00
106.00	2.00	2.00	2.00	22.00	180.00	3839.00
106.00	2.00	1.00	2.00	22.00	135.00	3273.00
107.00	2.00	2.00	2.00	25.00	166.50	4335.00
107.00	2.00	1.00	2.00	25.00	180.00	3008.00
108.00	2.00	2.00	1.00	24.00	162.00	2289.00
108.00	2.00	1.00	1.00	24.00	166.50	3784.00
109.00	2.00	2.00	1.00	20.00	324.00	3463.00
109.00	2.00	1.00	1.00	20.00	238.50	3643.00
111.00	2.00	2.00	2.00	39.00	148.50	4199.00
111.00	2.00	1.00	2.00	39.00	175.50	4355.00
112.00	2.00	2.00	1.00	26.00	270.00	4309.00
112.00	2.00	1.00	1.00	26.00	238.50	4308.00
113.00	2.00	2.00	1.00	42.00	193.50	2109.00
113.00	2.00	1.00	1.00	42.00	103.50	3328.00
114.00	2.00	2.00	1.00	41.00	225.00	3732.00
114.00	2.00	1.00	1.00	41.00	234.00	3057.00
115.00	2.00	2.00	2.00	60.00	211.50	4047.00

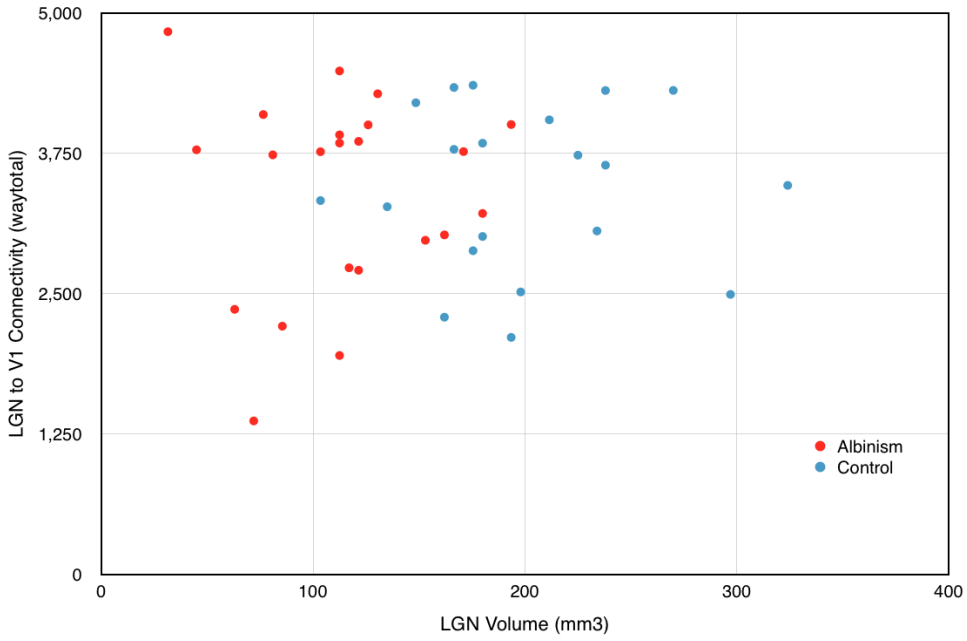

Figure B1: LGN volume (mm³) vs. LGN to V1 connectivity (waytotal), diffusion space.